

University of Nottingham
UK | CHINA | MALAYSIA

Mechanics and Biomimicking of Marine Mussel Byssus System

Thesis submitted to the University of Nottingham for the degree of **Doctor of Philosophy, July 2024.**

Yulan Lyu

20183910

Supervised by

Dr. Tao Liu
Prof. Wei Sun
Prof. Shuguang Li
Dr. Walid Tizani
Dr. Yong Pang

List of publications

Journals Publications The authors' contributions are shown in Appendix A.

1. **Lyu, Y.**, Pang, Y., Sun, W. and Liu, T.* (2024). Determining hyperelastic properties of the constituents of the mussel byssus system. *Soft Matter*, 20(11), 2442-2454. (**Cover paper**) https://doi.org/10.1039/D3SM01677C.

2. **Lyu, Y.**, Tan, M., Pang, Y., Sun, W., Li, S. and Liu, T.* (2024). Unveiling the deformability of mussel plaque core: the role of pore distribution and hierarchical structure. *Soft Matter*, 20, 4197-4207. https://doi.org/10.1039/D4SM00832D.

3. **Lyu, Y.**, Pang, Y., Sun, W., Li, S. and Liu, T.* (2024). Quasi-static indentation analysis for carbon-fibre mesh reinforced LLDPE foams inspired by mussel plaques. (**To be submitted**)

International conferences (Not included in thesis)

1. **Lyu, Y.**, Pang, Y., Sun, W. and Liu, T.* (2022). Mussel plaque inspired porous structure for the design of high ductility hyper elastomer. 18th European Mechanics of Materials Conference (EMMC18), Oxford

2. **Lyu, Y.**, Pang, Y., Sun, W. and Liu, T.* (2022). Mussel plaque inspired hyperelastic high fracture toughness random porous structure. 11th European Solid Mechanics Conference (ESMC 2022), Galway (**Received Women in STEM Conference Support Awards**)

3. Pang, Y., **Lyu, Y.**, Sun, W. and Liu, T.* (2022). Mechanical behaviours and failure mechanism in mussel plaque/substrate interface under directional tension. 18th European Mechanics of Materials Conference (EMMC18), Oxford

4. Pang, Y., **Lyu, Y.**, Sun, W. and Liu, T.* (2022). Development of polydimethylsiloxane (PDMS) substrates for traction forces measurement at marine mussel plaque/substrate interface. 11th European Solid Mechanics Conference (ESMC 2022), Galway

Abstract

The mussel byssus system, consisting of the proximal thread, distal thread, and adhesive plaque, enables marine mussels to attach securely to various surfaces and withstand sea waves. Extensive research has been conducted to analyse this natural system's chemical and structural composition. However, while the chemical properties of the mussel byssus system are well understood, its mechanical properties and potential biomimetic application require further investigation. This thesis aims to enhance our understanding of the mechanics and biomimicry of the mussel byssus system through three key aspects: (1) determining the mechanical behaviours and microstructural characteristics of the mussel byssus system's each component, (2) examining the impact of plaque microstructure on its tensile behaviour and inspired disordered porous structure design, and (3) showing a preliminary biomimetic example based on the microstructure of the mussel byssus system: the quasi-static indentation behaviour of carbon fibre mesh-reinforced linear low-density polyethylene (LLDPE) foams.

Firstly, scanning electron microscopy (SEM) analysis is employed to investigate the microstructure of each component of the mussel byssus system, including proximal thread, distal thread and adhesive plaque. Analytical and finite element (FE) inverse methods, combined with micro-tensile and optical tests, are developed to determine the individual mechanical

behaviours of these three components. It is found that the distal thread has higher tensile strength, and its tensile properties can be described using the Ogden constitutive model. In contrast, the proximal thread and plaque are more deformable. The Neo-Hookean model was applied to represent their tensile properties, with the residual sum of squares values of 0.0004 N^2 and 0.01 mm^2, respectively. These findings determine the mussel byssus system's mechanical behaviours and microstructure characteristics. Meanwhile, this study demonstrates the feasibility of using inverse methods to obtain the mechanical behaviours of complex biomaterials.

Secondly, SEM analysis is firstly applied to investigate the hierarchical porous structure of the mussel plaque core in detail, including porosity and pore distribution (size and location). Two types of two-dimensional (2D) porous representative volume elements (RVEs) are generated for qualitative analysis: one type uses scaled large-scale pore distribution parameters obtained from SEM analysis, and another type analyses the multi-scale porous structure. The calibrated phase field method is used to assess the effect of pore distribution and hierarchical structure on the mechanical behaviours and failure mechanisms of the porous RVEs. The findings show that pore distribution and multi-scale porous structure significantly influence the mechanical properties of RVEs, including strain energy density, tensile strength, and the final failure strain. This finding can further indicate that mussel plaque's pore distribution and multi-scale porous structure might be the key factors that contribute to its high deformability.

Thirdly, the high-strength mussel thread fibres embedded in the highly deformable porous plaque core inspire us to explore potential biomimetic applications. Due to the limitations of the experimental conditions, a preliminary attempt was made to manufacture carbon fibre mesh-reinforced LLDPE foams, where carbon fibre mesh is analogised as the thread fibre,

and the LLDPE foam is analogised as the plaque foamy core. The quasi-static indentation (QSI) tests were conducted to examine the QSI behaviour of carbon fibre mesh-reinforced LLDPE foams. The results show that the fibre mesh can enhance the indentation resistance of LLDPE foams by reducing sample bending. However, the position of the fibre mesh layers has minimal impact, while increasing the number of fibre mesh layers can effectively improve the LLDPE foams' indentation resistance under framed support. Two failure modes—fibre breakage and fibre pull-out were also observed within the fibre mesh layers. Additionally, indenter nose shapes and support conditions significantly influence the QSI behaviour of the samples. These findings show the potential to mimic the interaction between the mussel thread fibres and porous plaque core. Future studies can focus on accurately replicating the exact structure using three-dimensional (3D) printing technology and testing the material properties of the unique composite structure.

This research offers valuable insights into the mussel byssus system's mechanics and potential biomimetic application. Determining the system's components' mechanical behaviours and microstructure composition can deepen our understanding and inform future mimic designs. The analysis of the effect of the hierarchical porous structure of mussel plaque on its mechanical behaviour can inspire further research into disordered porous structure design. Finally, the experimental analysis of the QSI behaviour of carbon-fibre mesh-reinforced LLDPE foams inspired by the mussel byssus system highlights the preliminary biomimetic attempt of this natural system and builds the solid foundation for future biomimetic application. These findings have enhanced our understanding of the mechanics of the mussel byssus system and inspired future biomimetic designs.

Acknowledgements

My Ph.D. study over the past four years has been a truly transformative experience and has undoubtedly shaped me into a better person. This journey would not have been possible without the support of many individuals and institutions, to whom I am deeply grateful.

Firstly, I am very grateful for the continuous support from Dr. Tao Liu, both financially and academically. His unwavering professional guidance throughout my Ph.D. studies has been instrumental in helping me achieve my academic goals. I would also like to express my sincere gratitude to Prof. Wei Sun and Prof. Shuguang Li for their constant encouragement and professional support during challenging times. Additionally, I extend my heartfelt thanks to my other supervisors, Dr. Xianghui Hou and Dr. Walid Tizani, for providing the necessary support and resources at the university. A special note of appreciation goes to Dr. Yong Pang for his constant support and guidance, serving as both a good friend and mentor.

Secondly, I would like to thank the Leverhulme Trust Research Grant Scheme (No. RPG-2020-235) for their financial support. My special thanks also go to all the technicians at the Centre for Additive Manufacturing, the Civil Engineering Centre, the Transport Engineering Centre, and the Nanoscale and Microscale Research Centre at the University of Nottingham for their support throughout my Ph.D.

Finally, I would like to express my heartfelt thanks to my parents, my partner Zakariya and my friends. Without their constant love and support, it would have been very difficult for me to get this far. I dedicate this thesis to them and look forward to moving on to the next chapter of my life together.

Contents

List of publications **i**

Abstract **ii**

Acknowledgements **vi**

List of Tables **xi**

List of Figures **xii**

Abbreviations **xxiv**

Nomenclature **1**

Chapter 1 Introduction **10**

1.1 Background 10

1.2 Motivations 14

1.3 Aim and objectives 15

1.4 Thesis overview 16

Chapter 2 Literature review **19**

2.1 The constituents and microstructures of the mussel byssus system 19

2.2 The mechanical properties of the mussel byssus system . . . 26

2.3 The biomimetic applications of the mussel byssus system . . 31

2.4 Key research gaps 33

2.5 Summary of the literature review 36

Chapter 3 Overarching methodology **38**

3.1 Methods 38

3.2 Limitations 41

3.3 Summary 43

Chapter 4 Determining mechanical behaviours of the constituents of the mussel byssus system 44

4.1 Introduction 45

4.2 Material and methods 48

4.3 Mussel byssus system material constitutive models and inverse procedure 55

4.4 Results 63

4.5 Discussion 71

4.6 Conclusion 75

Chapter 5 Unveiling the deformability of mussel plaque core: the role of pore distribution and hierarchical structure 77

5.1 Introduction 78

5.2 SEM characterisation of mussel plaque core 80

5.3 The generation of the porous RVEs 84

5.4 ABAQUS implementation and experimental calibration of the phase field modelling method 90

5.5 The failure mechanism analysis of generated RVEs 102

5.6 Discussion 110

5.7 Conclusion 113

Chapter 6 A biomimetic application inspired by the mussel byssus system: The quasi-static indentation analysis of carbon-fibre mesh reinforced LLDPE foams 115

6.1 Introduction 116

6.2 Experimental methods 120

6.3 The results of experimental studies 125

6.4 Discussion 139
6.5 Conclusion 142
Chapter 7 Conclusions and future work 144
7.1 Conclusions 144
7.2 Future work 148
Bibliography 151
Appendices 179
Appendix A 180
Appendix B 182
Appendix C 188
C.1 Details on mussel samples preparation 188
Appendix D 189
D.1 The pore distribution analysis of mussel plaque SEM photos 189
D.2 The simplified process of the pore distribution of the mussel plaque cores 191
D.3 The Q–Q (quantile–quantile) plots 193
D.4 The size effect of RVE 193
D.5 The small-scale pores size effect study for the multi-scale porous RVEs 194
D.6 The derivation of Eq. 5.14 196
D.7 The derivation of Eq. 5.18 197
D.8 The comparison of the solid and small-scale porous RVEs . . 198
Appendix E 200
E.1 Typical framed-supported force–indentation curves for carbon fibre mesh reinforced LLDPE foams 200

List of Tables

4.1 mechanical behaviours for the distal portion 67

4.2 Proximal portion material parameter $C_1^p(MPa)$ and the min of the sum of square residuals (N^2) 68

4.3 Plaque portion material parameter $C_1^{pl}(MPa)$ and the minimum value of the sum of square residuals (mm^2) from the FE inverse approach 69

4.4 Bottom surface detachment radius $r_b(mm)$ and the minimum value of the sum of square residuals (mm^2) from the FE inverse approach 71

5.1 Porosity (υ_l), normalised mean radius $(\bar{\mu}_p^*)$ and normalised standard deviation of radius $(\bar{s}_p^*)$ of the simplified large-scale pores within the SEM images for different plaques. 84

5.2 Material parameters for TangoBlack Plus FLX980. 102

6.1 Material properties of LLDPE 8035 WS Black 9001 powder. 122

6.2 Material properties of the blowing agent ADC/M-C1. . . . 122

6.3 Material properties of the Mapegrid C 170 high-strength carbon fibre mesh. 125

6.4 Mechanical properties of pure LLDPE foams. 125

A.1 Publication(s) contribution 181

D.1 Porosity (υ_l), normalised mean radius ($\bar{\mu}_p^*$) and normalised standard deviation of radius ($\bar{s}_p^*$) of the simplified large-scale pores within the SEM images of the same mussel. 189

D.2 Porosity (υ_l), normalised mean radius ($\bar{\mu}_p^*$) and normalised standard deviation of radius ($\bar{s}_p^*$) of the simplified large-scale pores within the SEM images. 191

List of Figures

1.1 Location of adhesive-related proteins identified in the byssus of M. edulis. [1] 11

1.2 Morphology and fabrication of the mussel byssus. (a) Photo of a mussel in the process of extruding threads onto a plexiglass surface with its foot. Note the many threads already deposited. (b) m-CT image of the ventral surface of an iodine-stained mussel foot with two sections cut out to show the inner gland and groove structure in the middle of the foot and near the distal depression. Byssal threads are synthesized one at a time by secreting protein building blocks into the groove on the ventral side of the mussel foot. (c) Schematic of a single byssal thread, with scanning electron microscopy images highlighting the complex micron-scale morphologies of the protective cuticle (scale bar, 3 mm), fibrous core (scale bar, 5 mm) and the adhesive plaque (scale bar, 50 mm). [2] 12

1.3 The roles of mussel-inspired chemistry in the fabrication of anti-biofouling materials and the associated preparation strategies. [3] 13

2.1 (A) A Mytilus californianus mussel adhered to a surface using its byssus. (B) SEM of byssal thread torn open revealing core and cuticle. (C) A diagram illustrating the hierarchical arrangement of preCol proteins in the core. (D) A diagram illustrating the coordination link between His and Zn in His-rich regions of preCols. (E) Stress–strain curves for the distal and proximal threads. (F) The cyclic stress-strain curve of the distal thread shows a significant hysteresis in the initial cycle, damage in the subsequent cycle, and a self-healing response in the third cycle. The schematics show a hypothesised double network model that includes sacrificial bonds (His-Zn cross-links) and an elastic network (cross-beta sheet surrounding domains). [4] 22

2.2 The ultrastructure of a byssal adhesive plaque. (a) A byssated mussel showing the orientation of the sampled adhesive plaque (red). (b) Microscopic, reflected light image of a single attached plaque of Mytilus californianus. The underlying foam-like structure causes the light-scattering effect (white). The purple dashed line indicates the position of the freeze fracture. (c) Scanning electron microscope view of a freeze-fractured plaque illustrating the cuticle (Cut), the collagen fibers (Col) from the core, and the foam (Fo). (d) An enlargement of the foam-like structure shown in the blue boxed region in panel c. (e) The interfacial region between the plaque and the substratum shown in the yellow boxed region in panel c. A number of pillars (arrows) remain intact despite partial plaque delamination due to drying. [5] 23

2.3 Schematic view of mussel foot proteins (mfps) in a byssal plaque of Mytilus showing the approximate location of each of the major proteins. (a) Mfp-3 variants and mfp-5 are thought to be the adhesives (arrows). Mfp-2 makes up the core of each plaque. The entire plaque is coated by a cuticle made of mfp-1 and Fe3+. Mfp-4 may mediate links between the prepolymerized collagen (preCOL) fibers descending from the thread core to other proteins in the plaque. The red boxed region is enlarged in panel b. (b) Schematic view of all known mfp interactions as determined by the Surface forces apparatus (SFA). Mfp-3 and mfp-5 are responsible for the primary adhesive interactions with the surface. Only mfp-5 interacts with mfp-3, and only mfp-2 interacts with mpf-5. Interactions between mfp- 2s are entirely Ca2+ (blue) and Fe3+ (red) mediated. A Ca2+-mediated interaction between mfp-2 and mfp-4 also exists. Work-of-adhesion values for mfp-3 correspond to reducing (1.4 mJ m−2) and oxidizing (0.4 mJ m−2) conditions in the SFA. Interactions denoted by a question mark remain to be determined. Tmp denotes thread matrix protein. [5] 25

2.4 Example of plaque detachment via adhesive failure, at pull angle 45° and pull rate 30 μm/s. (a)–(d) The top row of images shows the thread–plaque deformations from a side-view perspective, while the lower row shows the debonding interface as observed from below the glass slide (scale bars = 1 mm). The dashed red circles are drawn to be slightly larger than the crack radius and included to aid the reader in identifying the location of the propagating crack. (e) Force to extend a thread–plaque sample a distance Δ_x. The labeled circular markers correspond to the images shown in panels (a)–(d). (f) Schematic showing the mechanism of adhesive failure in mussel plaques, where debonding is initiated at the plaque–glass interface via a center-initiated crack. [6] 30

2.5 Recent application of mussel-inspired adhesives. [7] 32

3.1 The main aspects and methods to investigate the mechanics and biomimicking of marine mussel byssus system [8, 9]. . . 39

4.1 (a) Mussel byssus system showing the threads and plaques, (b) a schematic illustration of a single mussel byssus structure and its protein composition, and (c) a schematic diagram of sample cutting positions: cutting position ① for collecting the whole mussel byssus system samples, ① and ③ for collecting thread samples, ② and ③ for collecting distal portion samples. 46

4.2 (a) Schematic illustration of a customised micro-tensile experimental setup, (b) focused plaque test setup, and (c) focused thread test setup. 50

4.3 (a) Side view of the mussel plaque, (b) side view of FE model of the mussel plaque, (c) bottom view of the mussel plaque, and (d) bottom view of the FE model of the mussel plaque, all under undeformed configuration. 51
4.4 (a) Schematic diagram of the simplified spring system, (b) schematic representation of the principle of the inverse method using displacement as a metric, (c) schematic representation of the principle of the inverse method using force as a metric, and (d) schematic of the deformed shape optimisation approach. 52
4.5 Flow chart of both analytical inverse and FE-based inverse procedures. 55
4.6 Flow chart of determining the mechanical behaviours of the plaque and the proximal portion by using FE-based inverse approach and analytical inverse approach, respectively. . . . 63
4.7 (a) The idealisation of the thread-plaque mechanics model, (b) the overall thread-plaque structure, and (c)-(f) the microstructures of proximal portion, transition portion, distal portion and plaque core, respectively. 64
4.8 (a) The tested distal portion force-displacement curves, (b) the converted nominal stress-strain curves, (c) the tested whole thread (proximal and distal) portion force-displacement curves, and (d) the tested distal-plaque portion force-displacement curves. 65
4.9 The average nominal stress-strain curves of the distal portion obtained by experiment (EXP curve), fitting (target curve) and inverse (analytical and FE inverse curves). 66

4.10 Nominal force-displacement curves of the thread (proximal and distal) portion obtained by experiment (EXP curve), fitting (target curve) and inverse (analytical and FE inverse curves). 67

4.11 (a) The side view of plaque deformation at $d_{pl} = 0mm$, $d_{pl} = 0.16mm$, $d_{pl} = 0.25mm$. (b) The force-displacement curves at $d_{pl} = 0mm, 0.16mm, 0.25mm$ without considering partial detachment at the bottom surface in the FE inverse solution, (c) the deformed shape comparison of the plaque portion at $d_{pl} = 0mm, 0.16mm, 0.25mm$ without considering partial detachment from the bottom surface in the FE inverse solution, (d) the force-displacement curves at $d_{pl} = 0mm, 0.16mm, 0.25mm$ with partial detachment at the bottom surface in the FE inverse solution, and (e) the deformed shape comparison of the plaque portion at $d_{pl} = 0mm, 0.16mm, 0.25mm$ with partial detachment at the bottom surface in the FE inverse solution. 69

5.1 (a) Mussel byssus system attached on a rock, (b) schematic diagram of the mussel plaque's microstructure [9], (c) large deformation of mussel plaque under tension, (d) the distribution of normalized x and y coordinates for large pore centres within the mussel plaque core, (e) the SEM photo showing the multi-scale porous structure of mussel plaque core and (f) the distribution of normalized radius for both large-scale (mirco) and small-scale (nano) pores within the mussel plaque core. 80

5.2 Pore size and location distribution analysis for SEM images of different plaques. 83

5.3 Schematic drawing of multi-scale porous RVEs generation (The mesh element type switched from 2D triangular plane stress elements CPS3T to coupled temperature-displacement truss element T2D2T). 90
5.4 Schematic drawings of (a) the SENT test samples and (b) the porous samples for tensile testing. 100
5.5 Comparison between the numerical and experimental stress-strain curves for samples with different notch lengths during SENT tests. 101
5.6 Comparison between the (a-c) numerical and experimental stress-strain curves and (d-f) fracture paths for three porous samples in tension (elements with $NT11 \geq 1$ were deleted). . 101
5.7 The RVE simulation and 3D linear regression results between the normalised mean value standard $\bar{\mu}$, normalised deviation value $\bar{s}$ of the large-scale pore radius and (a) $\Delta\varepsilon$ with a coefficient of determination (R^2) value of 0.08, (b) final failure strain (ε_{ff}) with a R^2 value of 0.12, (c) strength (σ_{max}) with a R^2 value of 0.4, and (d) strain energy density (φ) with a R^2 value of 0.53. The blue planes represent the linear regression surfaces, and the red dots represent the RVE results. 104
5.8 The 2D linear regression analysis between the normalised mean value standard $\bar{\mu}$ of the large-scale pore radius and (a) $\Delta\varepsilon$, (b) final failure strain (ε_{ff}), (c) strength (σ_{max}), and (d) strain energy density (φ). 105
5.9 (A) The macroscopic stress-strain curves, and (B) crack paths of selected samples with different failure modes. 106

5.10 (A) The macroscopic stress-strain curves of single and multi-scale porous samples, and (B) crack paths of multi-scale porous samples. 109

6.1 (a) A plaque–thread system of a marine mussel (from a blue mussel) [9]. (b) Schematic of the cross-section of a mussel plaque showing the internal structure, with the inset showing the top view of a real mussel plaque and the dashed line showing the direction of the section [9]. (c) Solid foam structure of a byssal adhesive plaque [8]. 118

6.2 (a) Uniaxial compression test setup with an Instron 68TM-50 test machine, and (b) the manufacturing process of the LLDPE foam for the uniaxial compression test. 121

6.3 A SEM image showing the microstructure of the LLDPE foam. 121

6.4 (a) The schematic drawings of four different indenter noses, (b) schematic drawings of framed support condition, (c) schematic drawings of solid support condition, (d) the manufacturing process of carbon-fibre reinforced LLDPE foam, and (e) four variants of fibre-reinforced polymeric foams: top-reinforced foam (TOF), mid-reinforced foam (MIF), bottom-reinforced foam (BOF), and top and bottom-reinforced foam (DOF). 124

6.5 The uniaxial compression stress-strain curves for three pure LLDPE foams. 126

6.6 The QSI force-indentation displacement curves for five variants of the fibre mesh-reinforced LLDPE foams under four different indenter noses using framed supporting: (a) flat-circular indenter, (b) truncated indenter, (c) hemi-spherical indenter, and (d) conical indenter. 127
6.7 Typical material parameters for three variants of the fibre mesh reinforced LLDPE foams with four different indenter noses using framed supporting: (a) max force (kN), (b) indentation depth at max force (mm), and (c) absorbing energy (J). 131
6.8 The QSI force-indentation displacement curves for three variants of the fibre mesh-reinforced LLDPE foams with four different indenter noses using solid supporting: (a) Flat-circular indenter, (b) truncated indenter, (c) hemi-spherical indenter, and (d) conical indenter. 132
6.9 Comparison of QSI force-indentation displacement curves and surface indentation of frame-supported and solid-supported LLDPE foams: (a) flat-circular indenter, (b) truncated indenter, (c) hemi-spherical indenter, and (d) conical indenter. 136
6.10 Comparison of QSI force-indentation displacement curves and surface indentation of top fibre mesh reinforced LLDPE foams with framed and solid supporting: (a) flat-circular indenter, (b) truncated indenter, (c) hemi-spherical indenter, and (d) conical indenter. 137

6.11 The fibre mesh failure modes under framed support: (a)-(d) fibre breakage on the top surface of TOF samples under four indenters, (e)-(h) fibre pull-out on the bottom surface of MIF samples under four indenters, (i)-(l) fibre pull-out on the bottom surface of BOF samples under four indenters, (m)-(n) fibre breakage on the top surface of DOF samples under four indenters and (q)-(t) fibre pull-out on the bottom surface of DOF samples under four indenters. 138

C.1 (a) The water tank for mussels, (b) the seawater PH=8.5, (c) rubber bands were used to fix uniformly sized marine mussels to the substrate. 188

D.1 Large-scale pore size and location distribution analysis for SEM images of the same mussel. 190

D.2 Large-scale pore size and location distribution analysis for SEM images of different mussel plaques. 191

D.3 The schematic drawing of the idealisation of the porous structure of mussel plaque cores. 192

D.4 Q–Q plots (quantile-quantile plot) comparing the x and y coordinates of large pores within the 9 mussel plaque SEM photos to a uniform distribution. 193

D.5 Schematic diagram of three difference sizes RVEs (60x60 mm, 30x30 mm, 15x15 mm). 194

D.6 Strain-stress curves of the three difference sizes RVEs (60x60 mm, 30x30 mm, 15x15 mm). 195

D.7 The macroscopic stress-strain curves of multi-scale porous RVEs with different approximate small-scale pore sizes: 0.4 mm, 0.5 mm (Sample C') and 0.6 mm. 196

D.8 The stress-strain curves of the solid and small-scale porous RVEs with 5% porosity. 199

E.1 Typical framed-supported force–indentation curves for different carbon fibre mesh reinforced LLDPE foams under conical indenter: (a) Top reinforced LLDPE foams (TOF), (b) middle reinforced LLDPE foams (MIF), (c) bottom reinforced LLDPE foams (BOF), (d) pure reinforced LLDPE foams (NOF) and (e) double reinforced LLDPE foams (DOF). 201

E.2 Typical framed-supported force–indentation curves for different carbon fibre mesh reinforced LLDPE foams under truncated indenter: (a) Top reinforced LLDPE foams (TOF), (b) middle reinforced LLDPE foams (MIF), (c) bottom reinforced LLDPE foams (BOF), (d) pure reinforced LLDPE foams (NOF) and (e) double reinforced LLDPE foams (DOF). 201

E.3 Typical framed-supported force–indentation curves for different carbon fibre mesh reinforced LLDPE foams under flat-circular indenter: (a) Top reinforced LLDPE foams (TOF), (b) middle reinforced LLDPE foams (MIF), (c) bottom reinforced LLDPE foams (BOF), (d) pure reinforced LLDPE foams (NOF) and (e) double reinforced LLDPE foams (DOF). 202

E.4 Typical framed-supported force–indentation curves for different carbon fibre mesh reinforced LLDPE foams under hemi-spherical indenter: (a) Top reinforced LLDPE foams (TOF), (b) middle reinforced LLDPE foams (MIF), (c) bottom reinforced LLDPE foams (BOF), (d) pure reinforced LLDPE foams (NOF) and (e) double reinforced LLDPE foams (DOF). 202

Abbreviations

2D Two dimensional.

3D Three dimensional.

AFM Atomic force microscopy.

BOF Bottom-reinforced foam.

DOF Top and bottom-reinforced foam.

DOPA 3,4-dihydroxyphenylalanine.

FE Finite element.

HDMS Hexamethyldisilane.

LLDPE Linear low-density polyethylene.

MFP-1 Mussel foot protein-1.

MIF Mid-reinforced foam.

NOF Pure LLDPE foam.

NTGF Normal traction-governed failure.

PET Polyethylene terephthalate.

PMI Polymethacrylimide.

PreCols Pre-pepsinised collagens.

PTMP-1 Proximal thread matrix protein-1.

PU Polyurethane.

QSI Quasi-static indentation.

RVEs Representative volume elements.

SEM Scanning electron microscopy.

STGF Shear traction-governed failure.

TMP-1 Thread matrix protein-1.

TOF Top-reinforced foam.

Nomenclature

α	notch lengths
$\bar{\lambda}_1, \bar{\lambda}_2$ and $\bar{\lambda}_3$	distortional principal stretches
$\bar{\mu}$	normalised mean value of the large-scale pores within generated RVEs
$\bar{\mu}_p^*$	normalised mean value of the large-scale pores' radius
$\bar{s}$	normalised standard deviation value of the large-scale pores within generated RVEs
$\bar{s}_p^*$	normalised standard deviation value of the large-scale pores' radius
$\boldsymbol{\lambda}_{\mathrm{d}}^{\mathrm{e}}$	experimental tensile strain for the distal portion
$\boldsymbol{\omega}_i$	material parameters of known sub-materials
$\boldsymbol{\sigma}_{\mathrm{d}}^{\mathrm{e}}$	experimental tensile stress for the distal portion
$\boldsymbol{d}(\boldsymbol{m})$	displacement of the overall spring system from the analytical inverse approach

$\boldsymbol{d}\left(C_1^{\mathrm{p}}\right)_{\mathrm{p}}$	elongation of the proximal portion based on the given material constant ${C_1}^{\mathrm{p}}$ in the analytical inverse approach
$\boldsymbol{d}\left(C_1^{\mathrm{p}}\right)_{\mathrm{t}}$	elongation of the whole thread based on the given material constant ${C_1}^{\mathrm{p}}$ in the analytical inverse approach
$\boldsymbol{d}^e$	experimental displacement data of the overall spring system
$\boldsymbol{d}^u(\boldsymbol{m})$	elongation of the unknown submaterial
$\boldsymbol{d}^{\mathrm{e}}_{\mathrm{d+pl}}$	experimental displacement of the mussel plaque
$\boldsymbol{d}^{\mathrm{e}}_{\mathrm{d}}$	experimental tensile displacement for the distal portion
$\boldsymbol{d}^{\mathrm{e}}_{\mathrm{p}}$	experimental tensile displacement for the proximal portion
$\boldsymbol{d}^{\mathrm{e}}_{\mathrm{t}}$	experimental tensile displacement for the whole thread
$\boldsymbol{F}$	deformation gradient tensor
$\boldsymbol{F}(\boldsymbol{m})$	residual vector
$\boldsymbol{f}(\boldsymbol{m})$	force of the overall spring system from the analytical inverse approach
$\boldsymbol{F}\left(C_1^{\mathrm{pl}}\right)$	residual vector for the given material constant C_1^{pl}
$\boldsymbol{F}\left(C_1^{\mathrm{p}}\right)$	residual vector for the given material constant C_1^{p}

$\boldsymbol{f}^e$	experimental force data of the overall spring system
$\boldsymbol{F}^{\mathrm{s}}\left(C_1^{\mathrm{pl}}\right)$	residual vector of each deformed shape
$\boldsymbol{f}^u(\boldsymbol{m})$	force of the unknown submaterial
$\boldsymbol{f}^{\mathrm{e}}_{\mathrm{d+pl}}$	experimental force of the mussel distal-plaque system
$\boldsymbol{f}^{\mathrm{e}}_{\mathrm{d}}$	experimental tensile force for the distal portion
$\boldsymbol{f}^{\mathrm{e}}_{\mathrm{pl}}$	experimental force of the mussel plaque
$\boldsymbol{f}^{\mathrm{e}}_{\mathrm{p}}$	experimental tensile force for the proximal portion
$\boldsymbol{f}^{\mathrm{e}}_{\mathrm{t}}$	experimental tensile force for the whole thread
$\boldsymbol{lb}$	lower bounds
$\boldsymbol{m}$	guessing material parameters of the unknown submaterial
$\boldsymbol{m}^*$	optimised material parameters
$\boldsymbol{n}$	the outward normal to the surface $\partial\Omega$
$\boldsymbol{ub}$	upper bounds
$\boldsymbol{u}$	displacement field
χ	changing rate of the heat flux
$\Delta\varepsilon$	the strain difference between the initial failure strain and the final failure strain for each RVE

$\dot{\boldsymbol{u}}$	the rate of change of the displacement field
$\dot{c}$	the rate of phase field variable
$\dot{D}^f$	rate of the dissipated energy from crack formation
$\dot{D}^g$	rate of dissipation energy for crack growth
$\dot{D}^{diss}$	the rate of the energy dissipated from the crack
$\dot{E}$	energy per time unit provided externally
$\dot{U}$	the rate of the strain energy stored in the material
η	fracture parameter
$\frac{\partial T}{\partial t}$	rate of the temperature field
$\gamma_l\left(c, \nabla_c\right)$	crack density function
$\hat{o}$	predicted value from the linear regression
κ_1	viscosity parameter
λ	uniaxial tensile stretch
λ_c	critical stretch value obtained when the applied load abruptly drops to zero in the SENT test
(x_i, y_i)	pore centre coordinates within the RVE
μ_p	scaled mean value of the normal distribution corresponding to the lognormal distribution

μ_p^*	mean value of the lognormal distribution of the large-scale pores within the SEM image
μ_{ps}^*	scaled mean value of the lognormal distribution of the large-scale pores within the SEM image
∇_c	spatial gradient
Ω	arbitrary body
$\partial\Omega$	the surface of the volumetric body Ω
ρ	density
σ	uniaxial compressive stress (Chapter 6)
σ	uniaxial tensile stress (Chapter 4)
$\sigma_{\max}$	tensile strength
τ	dissipated crack formation energy density
θ	distance between the centres of any two pores (Chapter 5)
θ	functional tolerance (Chapter 4)
υ	porosity of pores within the selected SEM image
υ_l	porosity of large-scale pores within the selected SEM image
υ_s	porosity of small-scale pores within the selected SEM image
ε	uniaxial compressive strain

ε_{ff}	final failure strain
φ	strain energy density
$\varphi_{iso}(\boldsymbol{F})$	the isochoric strain energy density
ξ	number of data points
A	the compressed contact surface area
a_0, a_1, a_2	regression coefficients
b	volumetric body force vector
c	phase field variable
C_1	material constant of the Neo–Hookean model
C_1^{pl}	guessing material constant of the mussel plaque
C_1^{p}	guessing material constant of the mussel proximal portion
c_p	specific heat
D	the compressive displacement
D^f	energy dissipated by the crack formation
F	the compressive load
G	strain energy rate
$g(c)$	quadratic degradation function
G_c	critical energy release rate
H	local history variable field
J	total volume ratio

k	number of data points obtained from the force–displacement curves (chapter 4)
k	thermal conductivity (chapter 5)
$K(\lambda)$	a function of the stretch value λ
k_1	total number of the deformed shapes
k_2	total number of selected nodes in each shape
l	length scale parameter (Chapter 5)
l	side length of the sample (Chapter 6)
l_d	length of the distal portion before tension
l_p	length of the proximal portion before tension
l_s	length of the squared SEM image edges
m	number of the large pores within the SEM images
N	order of strain energy potential
n	number of the large pores within the RVE
p	total number of sub-materials
q	heat flux/source (Chapter 5)
q	number of material parameters for the unknown sub-material (Chapter 4)
$R\left({C_1}^{\mathrm{pl}}\right)$	total sum of squared residuals for both force–displacement curves and deformed shapes
R^2	coefficient of determination

r_d	radius of the distal portion before tension
r_p	radius of the proximal portion before tension
r_i	radius of large-scale pores within the RVE
r_{pi}	radius of large-scale pores within the SEM images
s_p	scaled standard deviation value of the normal distribution corresponding to the lognormal distribution
s_p^*	standard deviation value of the lognormal distribution of the large-scale pores within the SEM image
s_{ps}^*	scaled standard deviation value of the lognormal distribution of the large-scale pores within the SEM image
T	temperature field
t	surface traction force vector
U	the strain energy stored in the material
u_β and α_β, $\beta = 1, 2, 3$	material constants of Ogden model
v_x, v_y, v_z	the corresponding velocity components
W	strain energy potential
w	side length of the RVE
$W(\lambda)$	material strain energy density under uniaxial tension

W_1 and W_2	non-negative weights
x, y, z	spatial coordinates
$(\boldsymbol{y}, \boldsymbol{z}\left({C_1}^{\mathrm{pl}}\right))$	coordinates of corresponding nodes based on the guessing material parameter C_1^{pl}

Chapter 1

Introduction

1.1 Background

The mussel byssus system comprises the proximal thread portion, the distal thread portion, and the adhesive plaque portion. It exhibits remarkable material characteristics such as high tensile strength, deformability, and durability (Figure 1.1) [1, 10, 11]. These features allow mussels to maintain their position on rocky shores despite the forces of waves and tides [6, 12–15]. Due to its distinctive properties, this natural system has captivated biologists and engineers for decades.

Numerous studies have focused on understanding the microstructural and chemical compositions of the mussel byssus system's components using advanced analytical techniques, including atomic force microscopy (AFM), scanning electron microscopy (SEM), and spectroscopy [1, 11, 16, 17]. Mussel threads consist of collagen-like proteins that contain silk- and elastin-like segments (Figure 1.1). These segments exhibit properties similar to nylon in the distal thread portion and a rubbery elastomer in the proximal thread

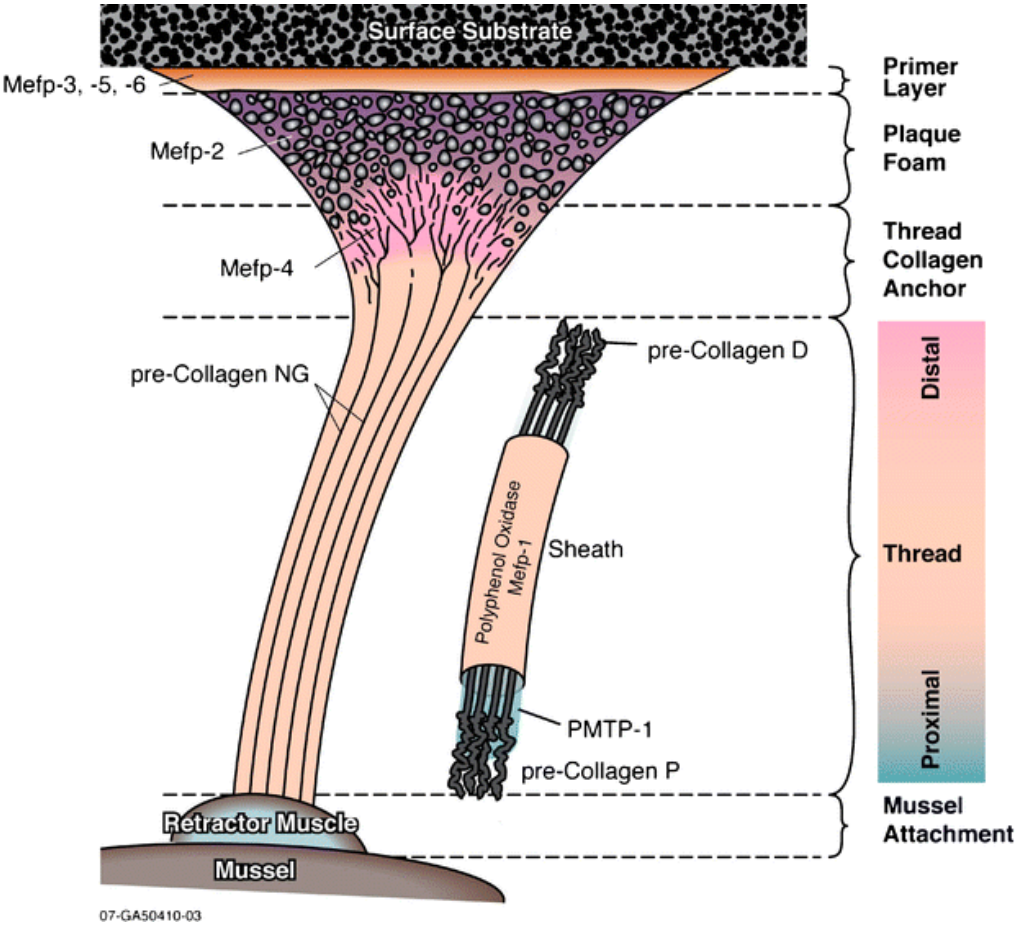


Figure 1.1: Location of adhesive-related proteins identified in the byssus of M. edulis. [1]

portion [18]. The fibrous thread core is coated with the cuticle protein mussel foot protein-1 (MFP-1), which contributes to the structural integrity of the threads (Figure 1.1) [1, 2]. Recent studies have also delved into the self-healing mechanisms of the proteins within mussel threads and their interactions with metal ions [19, 20]. Unlike the fibrous core of the mussel thread, the core of mussel plaque is a hierarchical porous structure (Figure 1.2) [16, 21]. Mfps 1-6 were found in the mussel plaque, with mfp-1, mfp-2, and mfp-4 contributing to cohesive strength and interaction, while mfp-3, mfp-5, and mfp-6 contribute to adhesive strength (Figure 1.1) [1, 22–24].

With a more comprehensive understanding of the structural and chemical composition of the mussel byssus system, researchers began investigating

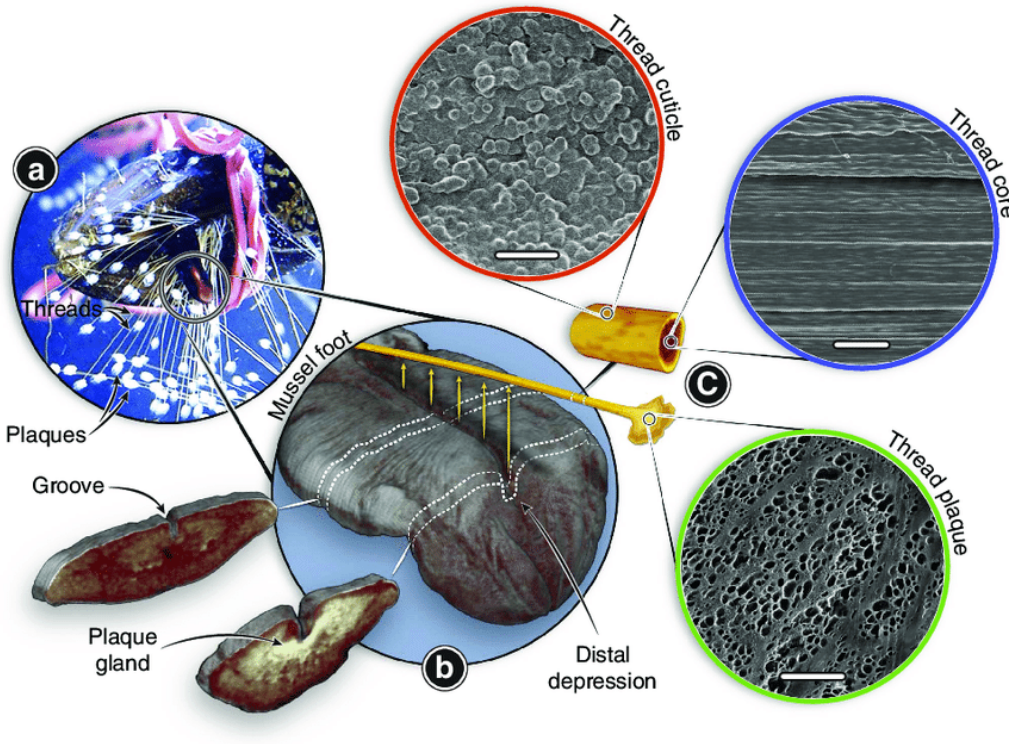


Figure 1.2: Morphology and fabrication of the mussel byssus. (a) Photo of a mussel in the process of extruding threads onto a plexiglass surface with its foot. Note the many threads already deposited. (b) m-CT image of the ventral surface of an iodine-stained mussel foot with two sections cut out to show the inner gland and groove structure in the middle of the foot and near the distal depression. Byssal threads are synthesized one at a time by secreting protein building blocks into the groove on the ventral side of the mussel foot. (c) Schematic of a single byssal thread, with scanning electron microscopy images highlighting the complex micron-scale morphologies of the protective cuticle (scale bar, 3 mm), fibrous core (scale bar, 5 mm) and the adhesive plaque (scale bar, 50 mm). [2]

its mechanical properties. Tensile tests were conducted on individual byssal threads and their components (distal and proximal portions) [25, 26]. The results demonstrated that the distal portion of the mussel thread has high tensile strength, approximately twice that of the proximal portion, and is over 50 times stiffer [26]. In contrast, the proximal portion exhibited high elasticity under tension, about twice that of the distal portion [26]. This combined behaviour endows the byssal thread with high tensile strength and deformability. Dynamic analysis was also conducted on the byssal thread and its components to investigate the self-healing mechanisms [27–

29].

The mechanical tests on individual mussel plaques are limited due to their size and fragility. However, the tensile adhesive tests have been conducted to analyse the adhesive behaviour of the whole byssus system [6, 26, 30]. A recent study by Desmond et al. (2015) has greatly advanced the study of mussel plaques by combining the tensile adhesive tests with the optical tests to demonstrate the deformation and failure modes of plaques at different tensile angles and strain rates [6]. Other studies have also explored the effects of seasonal variations and environmental factors on the mussel adhesion [31, 32].

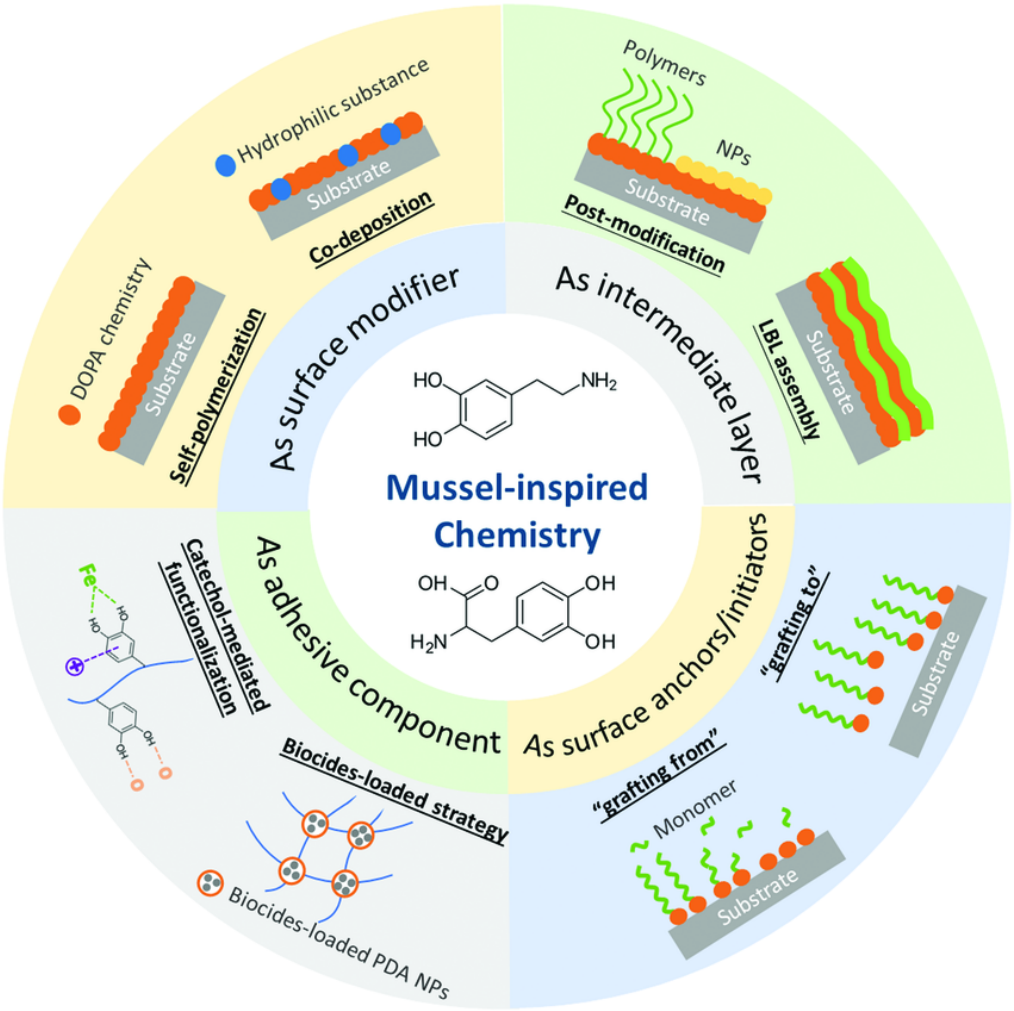


Figure 1.3: The roles of mussel-inspired chemistry in the fabrication of anti-biofouling materials and the associated preparation strategies. [3]

The unique protein and structural composition, combined with the mechanical properties observed in the mussel byssus system, has inspired a burgeoning research dedicated to biomimicking its characteristics. Biomimetics, or biomimicry, involves studying and imitating natural models to solve complex human problems [33]. Over the past decades, the mussel byssus system has inspired the development of advanced materials with applications (Figure 1.3) ranging from medical adhesives [34] and composite polymers [35] to self-healing hydrogels [36].

1.2 Motivations

In contrast to the considerable advances in understanding the chemical composition of the mussel byssus system and its chemical applications, research on its mechanical properties and inspired biomimetic designs remains comparatively limited. For instance, most studies on the mechanical properties of the mussel byssus system are experimentally based [6, 26, 30]. However, the fragility and size of the mussel byssus system undoubtedly increased the difficulty of the experiments. This motivated this research to develop more methods to investigate the mechanical properties of the mussel byssus system, such as the analytical method and finite element (FE) method.

Meanwhile, previous research has explored the relationship between the microstructure of mussel thread and its mechanical behaviour [25, 26]. However, the effect of the unique porous core of mussel plaque [16] on its mechanical properties remains unclear, which led us to investigate the potential link between them and inspire the future design of disordered porous structures.

Additionally, most biomimetic applications inspired by the mussel byssus system were based on its chemical composition [34–36]. Limited biomimetic research was conducted on this system based on its microstructure or mechanical properties. Therefore, a preliminary biomimetic study based on the microstructure of the mussel byssus system was conducted in this thesis.

By understanding the fundamental mechanics of the mussel byssus system and exploring more biomimetic solutions, nature's ingenuity could be applied to address contemporary engineering challenges in the future.

1.3 Aim and objectives

This study aims to gain insight into the mussel byssus system's mechanics and explore its biomimicry possibilities. Three studies were conducted and summarised in this thesis to achieve this goal. The corresponding objectives are summarised below:

- **Study 1** - (i) To investigate the difference between the cuticle of the proximal and distal threads, and the microstructure of the adhesive plaque; (ii) to determine the mechanical behaviours of the distal thread, proximal thread and adhesive plaque, respectively, using developed analytical and numerical inverse methods that integrate with micro-tensile and optical tests (Chapter 4).
- **Study 2** - (i) To analyse the pore distribution and multi-scale porous structure of the mussel plaque foam core using scanning electron microscope (SEM) analysis; (ii) to understand the effect of pore distribution and hierarchical porous structure on the mechanical behaviour and failure mechanism of porous RVEs using calibrated phase field

method (Chapter 5).

- **Study 3** - (i) To show a preliminary attempt for the biomimetic application: carbon fibre mesh-reinforced LLDPE foams, inspired by the structure of the mussel plaques' foamy core embedded with thread fibre; (ii) to investigate the effect of the location and number of fibre mesh layers on the QSI behaviour of LLDPE foams; (iii) to study the effect of indenter nose shapes and the type of support on the QSI behaviour of the carbon-fibre mesh reinforced LLDPE foams (Chapter 6).

1.4 Thesis overview

This thesis is organised into the following seven chapters:

Chapter 1 - This chapter briefly introduces this thesis's research background, motivation, aim and objectives.

Chapter 2 - The literature review outlines the mechanics and biomimicry of the mussel byssus system, including the microstructures and chemical compositions of each component of the mussel byssus system (proximal thread, distal thread and plaque), the mechanical properties of the mussel byssus system and the development of mussel-inspired biomimetic applications. The research gaps for each of the fields above are identified in the literature review.

Chapter 3 - This chapter presents the overarching methodology employed throughout this thesis. While each findings chapter has its own specific methodology tailored to its research questions, this chapter provides a comprehensive overview of the methodologies employed across the entire thesis.

It outlines the research design adopted to address the research questions or hypotheses and describes the overall research approach while objectively acknowledging the limitations.

Chapter 4 - This chapter examined the material characteristics of the components of the mussel byssus system. The mussel byssus system, which consists of the adhesive plaque, distal thread, and proximal thread, is essential for the survival of marine mussels under turbulent ocean conditions. This chapter represents the first utilisation of analytical and FE inverse methods for determining the mechanical behaviours of the mussel plaque and proximal thread. By employing mechanical and optical measurements, this reverse methodology provides a straightforward and effective approach to obtaining mechanical behaviours of various parts of the mussel byssus system. This, in turn, offers valuable insights into the potential applications of mimicking these qualities in material design.

Chapter 5 – To delve deeper into the microstructure of mussel plaques observed in Chapter 4, this chapter focuses on understanding the effect of the pore distribution and hierarchical porous structure of mussel plaque on its mechanical behaviours, especially its high deformability. The porous distribution of mussel plaques was investigated using SEM analysis. Two types of 2D porous RVEs with scaled large-scale pore distribution parameters and structure characteristics of plaque core obtained from the SEM analysis were generated for qualitative analysis. The calibrated phase-field method was then applied to interpret the effect of the pore distribution and multi-scale porous structure on the mechanical performance and failure mechanism of porous RVEs. The results show that both pore distribution and hierarchical porous structure could contribute to the high deformability of porous RVEs and affect mechanical properties like final failure strain, strength and strain energy density. This indicates that the

pore distribution and hierarchical porous structure could be the key factors contributing to the high deformability of mussel plaques. It also provides valuable insights for designing highly deformable biomimetic materials.

Chapter 6 - Except for the microstructure of mussel plaques, the structure of the thread fibres embedded into the plaque foam core also caught our attention. A preliminary biomimetic study was conducted to explore the potential biomimetic application and understand the reason behind this unique structure. The carbon-fibre mesh reinforced LLDPE foams were manufactured, with carbon fibre mesh presenting the 'thread fibre' and LLDPE foams presenting the 'plaque foamy core'. The experimental analysis investigated the impact of fibre mesh positioning and numbering within LLDPE foams on their QSI response. This chapter also analysed the effect of indenter nose shapes and support conditions on the QSI response of samples. The results show the potential to mimic the composite structure within the mussel byssus system and build a solid foundation to investigate its structure's application further.

Chapter 7 - The main conclusions of this thesis are presented in this chapter. Suggestions for potential future research following this thesis are also included.

It is noted that symbols defined in one chapter may represent different physical parameters in another chapter. Appendices and references for each chapter are compiled at the end of this thesis.

Chapter 2

Literature review

2.1 The constituents and microstructures of the mussel byssus system

Mussel byssus systems (Figure 2.1A) consist of threads and adhesive plaques that enable mussels to adhere to various surfaces under dynamic loading. This system has attracted considerable attention for its potential to inspire the development of advanced materials [4]. Therefore, understanding the constituents and microstructures of the byssus system is a crucial first step for unlocking its full potential in various applications.

2.1.1 The structural characteristics and chemical composition of the byssal thread

Macroscopically, the byssal thread consists of two main parts: the distal thread and the proximal thread [2, 37, 38]. In the SEM analysis, the proximal thread features a surface adorned with numerous transverse folds and

small furrows, and the distal part is characterised by a surface dotted with only small furrows [39]. A transition region has also been found between these two parts with combined structural features [39]. The length of the byssal thread varies according to the species and the specific environmental conditions, with adult mussels having threads between 2 and 6 cm in length [2, 40–42]. Typically, the length of the distal portion is around 80% of the total length of the thread, and the proximal portion comprises the remaining 20% [29]. Thread diameters also vary depending on the species or environment but are generally in the range of 0.1-0.2 mm [2, 43–45].

The byssal thread contains a fibrous core covered with a proteinaceous cuticle layer (Figure 2.1B). The protective cuticle layer has a granular appearance which is made up of mussel foot proteins and Fe-catecholate complexes (Figure 2.1B) [46–51]. The unique chemical composition provides remarkable hardness, high deformability, and self-healing ability [20]. For instance, the cuticle layer can be extended up to 100% of its original length before cracking, which is believed to be facilitated by its function as sacrificial load-bearing cross-links [47, 52]. Meanwhile, the cuticle has hardness and stiffness values similar to those of epoxy resins, being 4 to 5 times stiffer than the fibrous core, while maintaining high elongation at break [47, 53]. This makes it a prime example of a high-performance coating that combines hardness with exceptional elongation [54].

In addition to the cuticle layer, researchers have also studied the fibrous core of the byssal thread in depth [10, 55–57]. Three different partial collagen-like sequences of the byssal thread core were first obtained by Waite et al. (1998) and given the name pre-pepsinised collagens (PreCols) [55]. The PreCols have a modular structure similar to a block copolymer, consisting of a stiff collagen core domain, variable flanking domains on either side and two terminal histidine-rich domains (Figure 2.1C) [35, 58]. The stiff

collagen core domain of PreCols in byssal threads is a critical structural element that contributes to the mechanical properties and self-assembly of the threads. The core collagen domain in PreCols displays the characteristic Gly-X-Y motif, creating a triple helical structure about 150 nm long, which shapes the fibrous structure and contributes to the high stiffness of the threads [59]. Researchers also suggest that this may be responsible for the kinked central collagen domains of the PreCols [40, 60, 61]. This collagenous core domain is flanked by variable domains with three variants: preCol-D, preCol-NG, and preCol-P [40, 55]. PreCol-D, which has silk-like polyalanine runs, is mainly found in the distal portion of the byssal thread. In contrast, preCol-P, which has elastin-like polyalanine runs, is mainly found in the proximal portion [35, 55]. The preCol-NG with the Gly-rich flagelliform silk sequence is distributed along the entire thread [35, 55]. The inhomogeneous distribution of PreCols is considered to be a key factor that contributes to the difference in mechanical properties between the distal and proximal threads (Figure 2.1E) [25]. Moreover, the histidine-rich domains are situated at both the N- and C-terminal ends of all PreCols [59]. These domains contain a high concentration of histidine residues, which are believed to play a crucial role in thread assembly and self-healing [59]. This is due to their responsiveness to pH changes and their capacity to bind transition metal ions like Zn2+ and Cu2+ (Figure 2.1D) [59]. Histidine-rich domains contain metal binding and cross-linking sites that can create covalent cross-links using 3,4-dihydroxyphenylalanine (DOPA) residues and metal coordination complexes, which offer sacrificial bonds for strength and self-repair [2, 59, 62] (Figure 2.1F). Seven preCol triple helices then combine to create a 6 + 1 hexagonal bundle, serving as the primary unit in thread construction [19, 63]. Furthermore, two other distinct non-collagenous matrix proteins, thread matrix protein-1 (TMP-1) and proximal thread matrix protein-1 (PTMP-1), may contribute to the

mechanical gradient due to the uneven distribution along the byssal thread [2, 64].

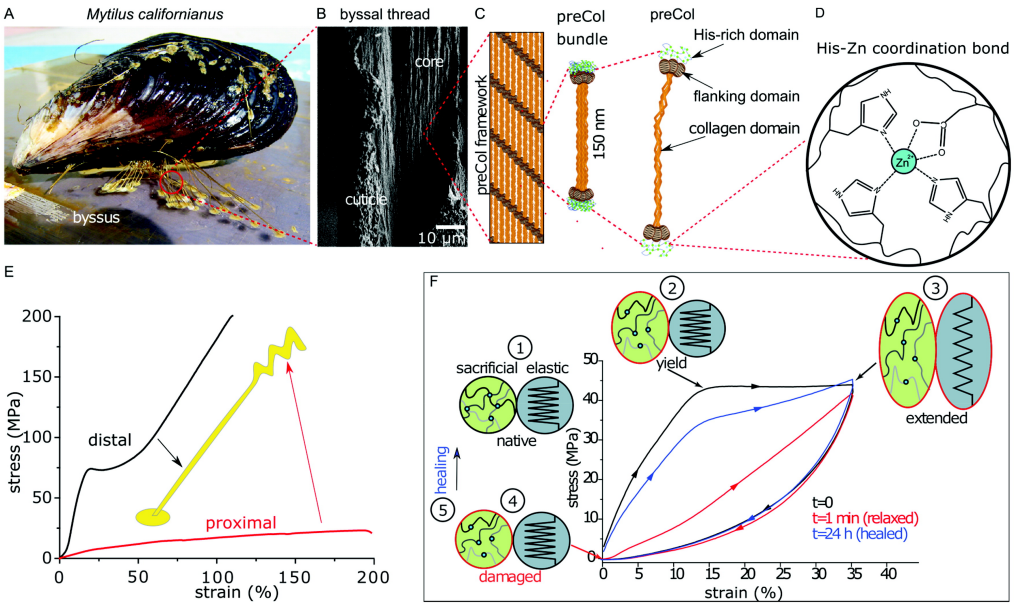


Figure 2.1: (A) A Mytilus californianus mussel adhered to a surface using its byssus. (B) SEM of byssal thread torn open revealing core and cuticle. (C) A diagram illustrating the hierarchical arrangement of preCol proteins in the core. (D) A diagram illustrating the coordination link between His and Zn in His-rich regions of preCols. (E) Stress–strain curves for the distal and proximal threads. (F) The cyclic stress-strain curve of the distal thread shows a significant hysteresis in the initial cycle, damage in the subsequent cycle, and a self-healing response in the third cycle. The schematics show a hypothesised double network model that includes sacrificial bonds (His-Zn cross-links) and an elastic network (cross-beta sheet surrounding domains). [4]

2.1.2 The structural characteristics and chemical composition of the mussel plaque

The mussel plaques have a multi-scale porous microstructure with large pores in the 1-3 μm range and small pores in the 75-130 nm range (Figure 2.2d) [16]. The porous structure of plaques is critical for accommodating microstructural damage, dissipating fracture energy and increasing adhesive strength, which makes it a vital aspect of plaques' functionality [65–68].

The porous core of the mussel plaque was also protected by the outer cuticle layer like mussel thread [5]. Interestingly, the generation of pores with the plaque core is related to the seawater PH values, whereas the development of the cuticle is not [21]. Additionally, the collagenous fibres from the thread's core extend to the plaque's porous core, as the roots of trees (Figure 2.2C) [4, 5].

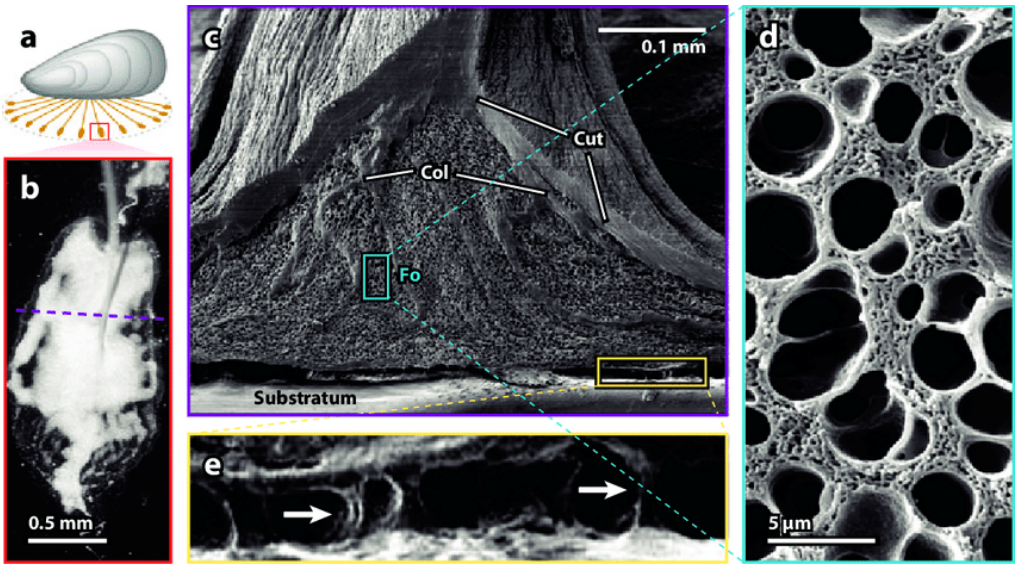


Figure 2.2: The ultrastructure of a byssal adhesive plaque. (a) A byssated mussel showing the orientation of the sampled adhesive plaque (red). (b) Microscopic, reflected light image of a single attached plaque of Mytilus californianus. The underlying foam-like structure causes the light-scattering effect (white). The purple dashed line indicates the position of the freeze fracture. (c) Scanning electron microscope view of a freeze-fractured plaque illustrating the cuticle (Cut), the collagen fibers (Col) from the core, and the foam (Fo). (d) An enlargement of the foam-like structure shown in the blue boxed region in panel c. (e) The interfacial region between the plaque and the substratum shown in the yellow boxed region in panel c. A number of pillars (arrows) remain intact despite partial plaque delamination due to drying. [5]

In addition to the complex plaque structure, the different proteins that make up the structure have been the research focus for the past decades. Mfp-1 is mainly located in the cuticle layer of the mussel byssus system [69–71]. It is a π-rich polymer with high water solubility and modest levels of Fe3+ [69–71]. The water-soluble and protective characteristics allow it

to improve the plaque's adherence to different surfaces by forming a stable and long-lasting coating (Figure 2.3a) [69–71]. Meanwhile, five distinct proteins, mfp-2, mfp-3, mfp-4, mfp-5 and mfp-6, were found by Waite's team to be particularly located in the plaque [60, 72–76]. Mfp-2 is the predominant protein in mussel plaque, constituting 25% of the plaque weight [5, 77]. It is mainly found in the structured foam of mussel plaques [4]. Raman microscopy has confirmed that the complexation of metal ions (especially Fe3+) with mfp-2 affects plaque cohesion [22]. Additionally, the interaction between mfp-2 and mfp-5 at the plaque-substrate interface also affects the plaque cohesiveness (Figure 2.3b) [22]. Moreover, mfp-3, mfp-5 and mfp-6 were found close to the interface between the plaque and the substrate [78]. The adhesive protein known as mfp-3 functions as a cohesive agent, facilitating the attachment of mussels onto various surfaces [69, 79]. Researchers have explained the indispensability of mfp-3 in plaque adhesion for different reasons: (i) The 3,4-dihydroxyphenylalanine (DOPA) in mfp-3 interacts with surfaces through its redox capacity, metal complexation, hydrophobic interactions and bidentate hydrogen bonding [79–81]; (ii) The adaptability and higher mobility of mfp-3 help it to diffuse into narrow gaps and create more binding sites [69, 82, 83]. Like mfp-3, mfp-5 contains a significant amount of DOPA that helps mfp-5 to build strong interaction with organic surfaces [84]. Mfp-6 is also a crucial component for the adhesive properties of mussel plaque [85–87]. The redox capacity of Mfp-6, e.g. the reduction of quinone to catechols, enhances the binding and cross-linking processes of proteins within the plaque, thereby improving the stability and adhesion of mussel plaque proteins [85–87]. Recently, researchers have suggested that mfp-5 constitutes the adhesive layer at the substrate interface, whilst a fluid protein condensate, including mfp-3 and mfp-6, fills the pores near the surface [80]. Furthermore, mfp-4 was thought to be the biochemical link between preCol fibres and mfp-2 (Figure 2.3b)

[60]. In addition to these five major proteins, recent studies have shown that another ten phenolic glandular proteins may be present in plaques [75].

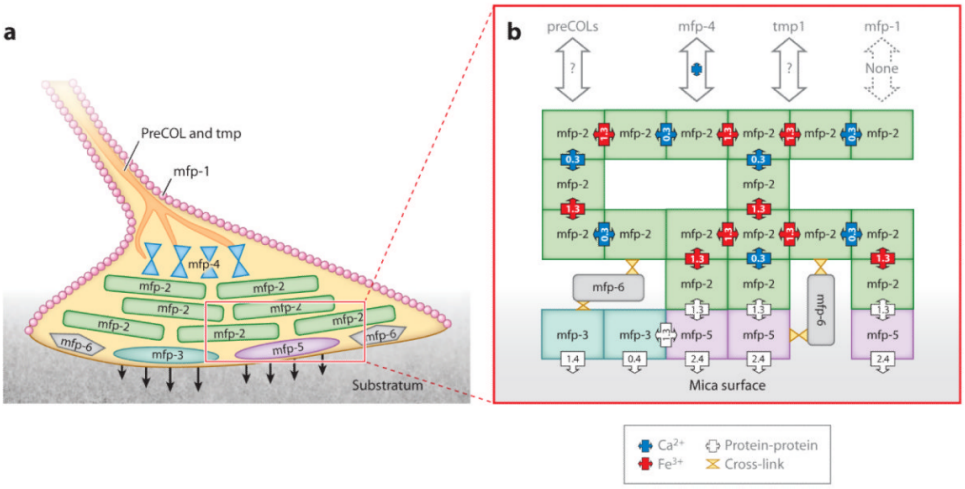


Figure 2.3: Schematic view of mussel foot proteins (mfps) in a byssal plaque of Mytilus showing the approximate location of each of the major proteins. (a) Mfp-3 variants and mfp-5 are thought to be the adhesives (arrows). Mfp-2 makes up the core of each plaque. The entire plaque is coated by a cuticle made of mfp-1 and Fe3+. Mfp-4 may mediate links between the prepolymerized collagen (preCOL) fibers descending from the thread core to other proteins in the plaque. The red boxed region is enlarged in panel b. (b) Schematic view of all known mfp interactions as determined by the Surface forces apparatus (SFA). Mfp-3 and mfp-5 are responsible for the primary adhesive interactions with the surface. Only mfp-5 interacts with mfp-3, and only mfp-2 interacts with mpf-5. Interactions between mfp-2s are entirely Ca2+ (blue) and Fe3+ (red) mediated. A Ca2+-mediated interaction between mfp-2 and mfp-4 also exists. Work-of-adhesion values for mfp-3 correspond to reducing (1.4 mJ m−2) and oxidizing (0.4 mJ m−2) conditions in the SFA. Interactions denoted by a question mark remain to be determined. Tmp denotes thread matrix protein. [5]

In summary, the investigation into the constituents and microstructures of the mussel byssus system offers a fundamental comprehension of the structural and chemical compositions that define this distinctive attachment system. The byssus exhibits a complex arrangement of proteins, metal ions, and structural frameworks, highlighting its complicated nature and providing a foundation for further exploration of its functional capacities.

2.2 The mechanical properties of the mussel byssus system

Transitioning from microstructural components to mechanical attributes, we focus on understanding how these parts converge to confer the mussel byssus system with its exceptional mechanical capabilities. The dynamic relationship between the structural integrity of the mussel byssus system and its ability to adapt to different environmental pressures highlights the remarkable evolutionary nature of this biological adhesive system, thereby connecting its microstructural composition and its macroscopic mechanical behaviour.

2.2.1 The mechanical properties of the byssal thread

Initial studies of the byssal thread have focused on measuring the whole thread mechanics in different sizes of mussels or wet/dry conditions, and researchers have begun to notice differences in mechanical properties between proximal and distal threads [13, 88, 89]. Later, Gosline and Carrington (1994) identified isolated tensile behaviours of the proximal and distal threads [26]. The distal portion of M. californianus exhibits more than 50 times greater stiffness, a strength approximately twice greater, and extensibility approximately half that of the proximal portion [26]. The strain-stress curve of the proximal portion shows a nonlinear trend, without an obvious yield point, and extends until it breaks at approximately 200% strain (Figure 2.1E) [25–27]. Four separate stress regimes are shown in the distal portion's stress-strain curve: elastic, plateau, hardening, and final failure [26, 27]. The distal thread exhibits an initial stiffness, accompanied by a distinct yield point at a strain of 12%. Subsequently, a post-yield

plateau is observed until a strain of 40%, after which the stress progressively increases until failure is reached at a strain of 100% [26, 27, 90]. The yield behaviour is also shown in the tensile test of the whole thread [27]. The distinct mechanical behaviour shown by the proximal and distal threads can help reduce stress concentrations resulting from modifications in the modulus and prevent localised failure during sudden transitions, such as those occurring at the interface [91]. Additionally, environmental factors such as epibiont fouling, site-specific conditions, or seasonal variations have a significant impact on the mechanical properties of mussel threads [72, 92–94]. In harsh environments, mussels have the ability to alter the diameter and mechanical properties of mussel threads to increase their strength. In more favourable environments, they can redistribute energy to vital structures such as gonads and soft tissue growth [92]. The threads produced in spring exhibited an increase in strength of more than 60% and an improvement in extensibility of 83% compared to the threads generated during other seasons [93]. Recent studies have also suggested that anthropogenic factors, such as noise pollution, lead to a reduction in the secretion of mussel threads and a subsequent deterioration in their mechanical properties, such as strength, elongation, and toughness [95].

Mussel threads are also key in helping mussels dissipate energy from dynamic loads under the sea [43]. Therefore, cyclic loading tests of the byssal threads can help to understand their mechanisms [26, 27, 43, 62, 91]. The mechanical behaviour of mussel threads under cycle loading depends mainly on their cyclic extension [26]. When the distal portion was subjected to low extension (8%), it showed stiffness and strong resilience (88%), and all future cycles were identical to the initial one [26]. When subjected to a series of escalating extensions ranging from 16% to 65%, the initial cycle showed a significant decrease in resilience, decreasing from 88% to 29%

[27]. The distal portion's initial modulus and hysteresis are reduced during the second cycle when the strain exceeds the yield point [91]. For the proximal portions, a strain stiffening phenomenon was observed instead of strain softening, with the initial modulus of 35 MPa gradually increasing to an asymptotic level at 50 MPa [91, 96]. The mechanical properties of whole threads also depend on their cyclic extension. The resilience of the byssal threads was 68% when strained to an extension below its yield point but was reduced to 35% when cycled to an extension below its yield point (Figure 2.1F) [27]. When loaded to failure, the initial stiffness of the extended samples below the yield point increased by 22%, whereas the extended samples' stiffness below the yield point decreased by 54% and lacked a yield region [27]. Interestingly, strain stiffening was also observed for the whole byssal threads when cycled to 11% extension [27]. A generalised Maxwell model has recently been built to describe stress relaxation in the byssal threads, which implies the adaptability of the byssal threads to cyclic loading [43].

In cyclic loading tests, an important mechanism of mussel threads was revealed: the self-healing ability. The initial modulus of the distal thread decreased from 600 MPa in the first cycle to 100 MPa in the second cycle and was recovered to 170 MPa after 1 hour of rest [90]. Gosline also observed that the area enclosed by the second loop was reduced to 38% of the first loop, but after a 30-minute break, the area surrounded by the loop was recovered to 68% of the first loop [27]. In particular, the recovery time is related to the length of the extension; the longer the extension, the longer the time taken to recover [27]. The self-healing response is believed to be the consequence of different mechanisms including reversible His-metal cross-links, sacrificial protein-metal bond exchanges, and the polyphenolic amino acid l-3,4-dihydroxyphenylalanine (DOPA) (Figure 2.1F) [96–100].

Increased temperature and PH value can help accelerate the healing process of the stiffness and strain energy of the byssal threads [62, 97, 101].

2.2.2 The adhesion of the mussel plaque

In addition to the unique compositional structure of mussel threads and their extraordinary ability to self-heal, the ability of mussel plaques to adhere firmly to the surface of the moist marine intertidal zone has also attracted the attention of researchers [67, 68, 102]. Early studies focused on the effect of various surfaces and hydrodynamic forces on the attachment strength of the mussel byssus system [26, 103]. Based on this, Burkett's team (2009) further developed a method to quickly measure the detachment force and the area of mussel plaques [30]. They investigated the effect of different surfaces on their adhesion force and found that most adhesion failures occurred in plaques [30]. Desmond et al. (2015) later conducted a pioneering study that integrated mechanics and video recordings to examine the deformation of plaques to the point of failure at varying angles and strain rates [6]. In the study, three different failure modes were identified, including adhesive failure, interior cohesive failure, and tear failure (Figure 2.4) [6]. The wet adhesive strength of an M. californianus plaque on glass exhibits a range of 1 to 5 MN/m with a pulling angle of 45° and a speed of 30 μm/s [6]. A recent study by Pang and Liu (2023) has further defined the failure modes of plaque detachment as shear traction-governed failure (STGF) mode and normal traction-governed failure (NTGF) [9]. They found that decreasing the pulling angle or increasing the substrate stiffness can lead to a transition in failure mode from NTGF to STGF [9].

In addition to investigating the mechanical response of the mussel byssus system under adhesive tensile tests, Valentine's team (2017) also analysed

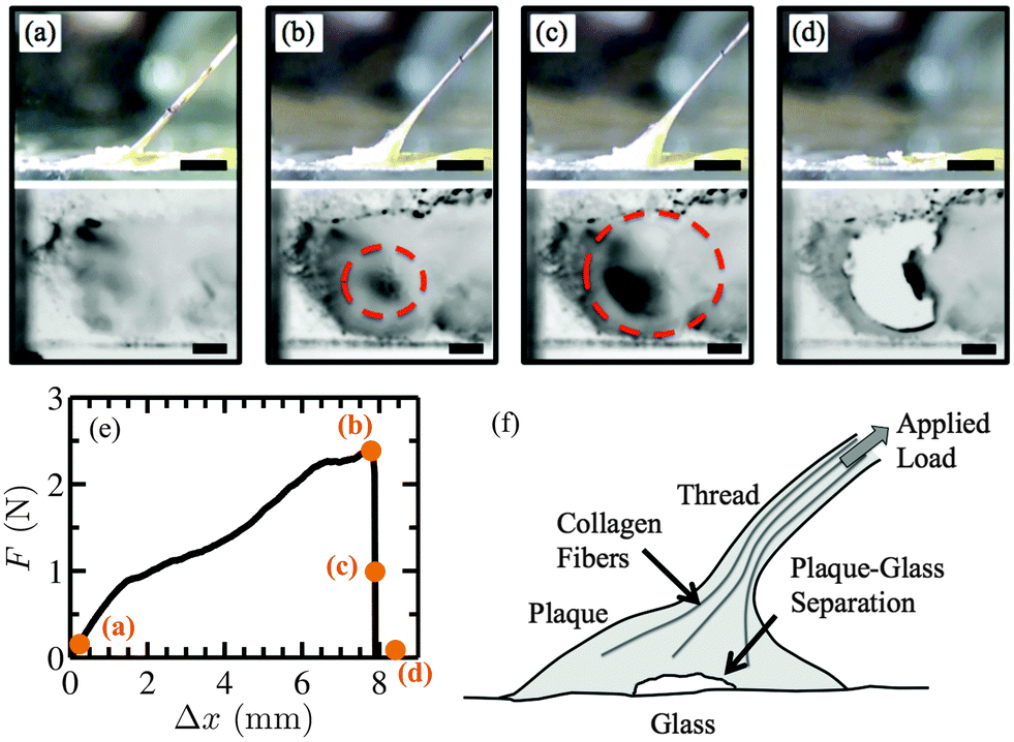


Figure 2.4: Example of plaque detachment via adhesive failure, at pull angle 45° and pull rate 30 μm/s. (a)–(d) The top row of images shows the thread–plaque deformations from a side-view perspective, while the lower row shows the debonding interface as observed from below the glass slide (scale bars = 1 mm). The dashed red circles are drawn to be slightly larger than the crack radius and included to aid the reader in identifying the location of the propagating crack. (e) Force to extend a thread–plaque sample a distance Δ_x. The labeled circular markers correspond to the images shown in panels (a)–(d). (f) Schematic showing the mechanism of adhesive failure in mussel plaques, where debonding is initiated at the plaque–glass interface via a center-initiated crack. [6]

its mechanical behaviour under multi-cycle loading [66]. They found that the low-strain stiffness of the plaques was reduced through multicycle loading, and irreversible plastic damage was introduced into the plaque microstructure [66]. The plaques enhance toughness by effectively dispersing the applied stress throughout the process of progressive plastic deformation [66]. However, when comparing plaques subjected to monotonically loaded failure, it is observed that the strain history does not have a detrimental effect on the critical strength or maximum strain, indicating that there are a variety of force transfer mechanisms between the thread and

the plaque-substrate interface [66].

Environmental conditions substantially influence the adhesive behaviour of mussel plaques. The adhesion strength and effectiveness of mussel plaques can be influenced by various factors, including PH, temperature, substrate type, season, salinity and the metabolic condition of the organism [104]. For example, marine mussels have been shown to have an acidic PH ($PH < 2$) beneath their foot during the plaque formation process [17]. For mussels, the acidic PH facilitates the delivery of adhesive proteins, stabilises DOPA for stronger bonding, enhances cationic functionality for better surface attraction, and, when combined with seawater, triggers protein insolubility and cross-linking for effective attachment [5, 79, 85, 86, 105–107]. However, mussels must be kept in a higher PH environment. Experiments have shown that keeping plaques in low PH conditions prevents them from gaining strength, leading to more frequent tearing of the material under tension [108].

Studying the mechanics of the mussel byssus system has revealed its incredible adhesion, strength, deformability, and adaptability. These unique biological features show mussels' extraordinary capabilities to thrive in dynamic and challenging marine environments and serve as a source of inspiration for cutting-edge biomimetic applications.

2.3 The biomimetic applications of the mussel byssus system

The mussel byssus system has inspired numerous biomimetic applications due to its unique adhesive and mechanical properties (Figure 2.5). Re-

searchers have utilized the strong wet adhesion and versatility of mussel foot proteins (Mfps) to develop new materials, such as hydrogels and adhesives [7, 104, 109], for various applications in medicine [110–114], environmental engineering [115, 116], and materials science [113, 114]. By mimicking the chemistry of Mfps, scientists have created innovative smart adhesives [117–119], self-healing materials [113, 120–128], and surface coatings [129–132] with enhanced properties like water resistance and adaptability.

These biomimetic applications bridge nature's sophisticated solutions with modern technological needs, opening up new possibilities in advanced materials design and functionality. However, despite the significant advancements in understanding the chemical structure of the mussel byssus system, its potential for biomimetic applications in terms of mechanical properties and microstructure remains relatively underexplored. Exploring the potential of this gap forms a key focus of this thesis.

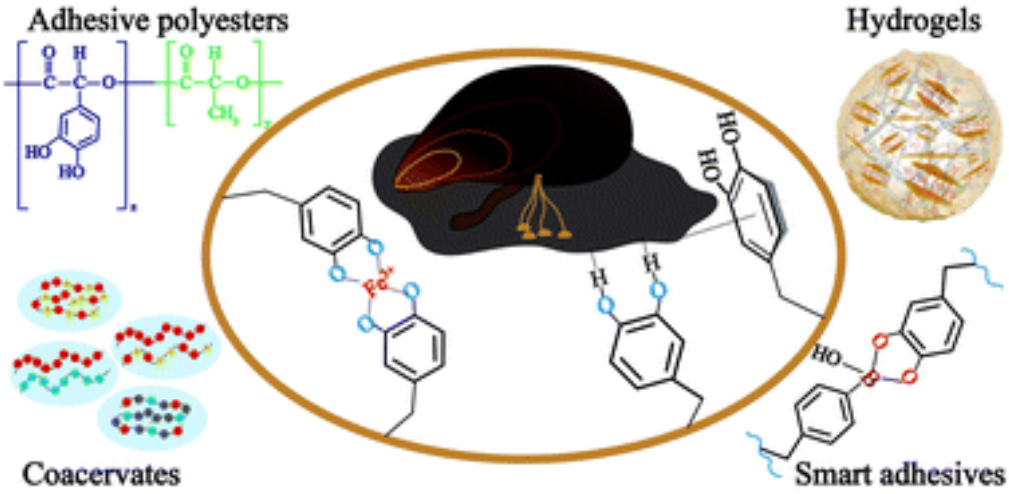


Figure 2.5: Recent application of mussel-inspired adhesives. [7]

2.4 Key research gaps

The byssus system of marine mussels represents an exceptional example of evolutionary optimisation, demonstrating distinctive characteristics such as strong adhesion, high deformability, and self-healing ability in underwater environments. The literature review describes in detail the research carried out in recent decades on the chemical composition, microstructure and mechanical properties of the marine mussel byssus system. Meanwhile, it has also underscored substantial progress in the field of biomimetic materials inspired by the marine mussel byssus system. However, in order to further investigate the mussel byssus system and effectively mimic its ability to solve practical problems, it is crucial to overcome the specific deficiencies that still exist in the research landscape. These gaps represent key opportunities to advance the field through targeted research initiatives.

2.4.1 The mechanical properties of the components of the mussel byssus system

Over the past decades, chemists have extensively studied the major chemical components of the marine mussel byssus system, including the mussel foot proteins (Mfps) contained in the mussel plaque and their content of DOPA (3,4-dihydroxyphenylalanine), the PreCols contained in the mussel threads (preCol-D, preCol-NG and preCol-P), and the Mfps and cuticle-specific proteins contained in the cuticle layer. However, the small size, fragile nature, and need to maintain moisture in the byssus system of marine mussels pose a challenge when conducting experiments aimed at measuring the mechanical properties of its constituents. Previous research has effectively determined the tensile curves of both proximal and distal

threads and the adhesive strength of the entire byssus system. However, the tensile mechanical properties of the mussel plaque portion have not been thoroughly investigated. Investigating the mechanical properties of the plaque portion using analytical or numerical methods is a promising avenue of research. Waite et al. (2019) developed a system of nonlinear springs to represent the mechanical contributions of different components, including the proximal and distal thread portions and the adhesive plaque [133]. The model estimates the elastic properties of these components and predicts the system's behaviour under tensile stress [133]. However, the model has limitations, particularly in its ability to capture the complex behaviour of the plaque fully, as it simplified the stress-strain curve of mussel plaque to three linear regions [133]. Therefore, more accurate analytical or numerical methods can facilitate accurate modelling of the mussel byssus system and a true understanding of each component's contribution to its overall mechanics.

2.4.2 The effect of the microstructure of mussel plaque on the mechanical performance

A notable research gap remains in determining how the porous microstructure of the mussel plaque affects the overall mechanical performance of the mussel byssus system. Our literature review shows that mussel plaque consists of a soft porous core under a hard cuticle layer, with the core exhibiting a randomly organised, multi-scale pore distribution. While it is evident that organisms have evolved structures to mitigate damage, the specific functions of such random and multiscale porous structures within the mussel plaque core and their contributions to the deformability or strength of the plaque or the overall byssus system remain unclear. Current re-

search focuses predominantly on the biochemical composition and adhesive properties of mussel plaques, largely neglecting the complex microstructural variations within the plaque that could significantly influence tensile strength or deformability under different environmental scenarios. limited study has tried to investigate how changes in the pore distribution of mussel plaques might affect their adhesion [134]. However, this study has applied an ordered pore arrangement rather than understanding the pore distribution found in mussel plaques. Filling this gap is crucial for developing bio-inspired materials that exploit these unique structural features to enhance mechanical properties in engineering applications.

2.4.3 The development of mussel-inspired biomimetic materials

While significant progress has been made in the development of mussel-inspired biomimetic materials, current research has focused primarily on the protein aspect, such as mimicking the adhesive proteins found in mussels, specifically the catecholamine chemistry of mussel foot proteins, for applications in wet adhesive environments. However, less emphasis has been placed on mimicking the specific material gradients of the mussel byssus system, the interactions between the mussel thread fibres and the porous plaque core, or the hierarchical porous structure of the plaque core. Gaining a comprehensive understanding of the mechanical mechanisms and the microstructure of the mussel byssus system is crucial in order to use this knowledge for the development of more biomimetic applications.

2.4.4 Summary of the key research gaps

This section has highlighted several critical gaps in the current understanding of the mechanism and biomimicry of the mussel byssus system. Addressing these gaps through focused research could lead to significant advances in materials science. Therefore, our research has attempted to fill these research gaps. Firstly, there is a need to further investigate the mechanical properties of the components of the byssus system, including the proximal thread, distal thread and mussel plaque, and understand their individual contribution. Secondly, it is important to understand the effect of the unique porous structure of the mussel plaque core on the overall mechanical properties of the mussel byssus system. Finally, the microstructure of the mussel byssus system has inspired us to conduct a preliminary biomimetic design study based on the interaction between thread fibre and plaque foamy core.

2.5 Summary of the literature review

This literature review has comprehensively examined the structure, chemistry, mechanics and biomimicry of the marine mussel byssus system.

Firstly, it commenced with a detailed analysis of the mussel byssus system's unique chemical compositions, constituents and microstructures. These are optimised for robust performance under the dynamic and challenging conditions of marine environments. This foundational understanding is critical as it sets the stage for appreciating the system's capabilities and potential for technological applications.

The review then transitioned to the mechanical properties of the mussel

byssus system, emphasising its strength, adhesion, deformability, and self-healing characteristics, which are crucial for survival in tidal zones. These features demonstrate mussels' evolutionary finesse and serve as a blueprint for developing advanced materials that mimic these natural solutions.

Furthermore, the review highlighted various biomimetic applications inspired by the byssus system. It delved into developing novel adhesive materials and self-healing composites that incorporate mussels' biochemical strategies, such as using DOPA and catecholamine chemistry. These sections illustrated how biological insights translate into real-world applications, thus paving the way for medical technologies, environmental challenges and engineering innovations.

Nevertheless, despite the considerable advances that have been made, this review has also identified and discussed several key research gaps. These include the need for a deeper investigation into the individual mechanical properties of byssus components, a better understanding of how these properties contribute to the overall system function, etc. Addressing these gaps could significantly enhance the design and synthesis of biomimetic materials.

In conclusion, this review presents the complex nature of the mussel byssus system and underscores its transformative potential in materials science. Bridging biological mechanisms with synthetic applications opens up new avenues for future research aimed at harnessing and amplifying the unique properties of the mussel byssus system in advanced material designs. This interdisciplinary approach is crucial for pushing the frontiers of both biological understanding and material innovation.

Chapter 3

Overarching methodology

3.1 Methods

The primary goal of this thesis is to investigate the mechanics of the mussel byssus system and apply its unique structural and mechanical properties to develop biomimetic designs. The research is structured around three interconnected aspects: (i) determining the mechanical behaviours and structural compositions of each component of the mussel byssus system, (ii) investigating the relationship between the unique microstructure of the mussel byssus system, especially the plaque, and its mechanical properties, and (iii) exploring potential biomimetic designs based on these mechanics and microstructures.

To cohesively address these aspects, three studies were designed with specific methodologies that build upon one another to form a comprehensive investigation of the system. Figure 3.1 illustrates the strategy of inquiry that links these studies, ensuring a clear progression from understanding the natural system to applying its principles in biomimetic design. The

following section outlines the overarching methodologies employed in these studies, with more detailed methodologies provided in Chapters 4-6. The Animal Welfare and Ethical Review Body (AWERB) form used in this study is provided in Appendix B.

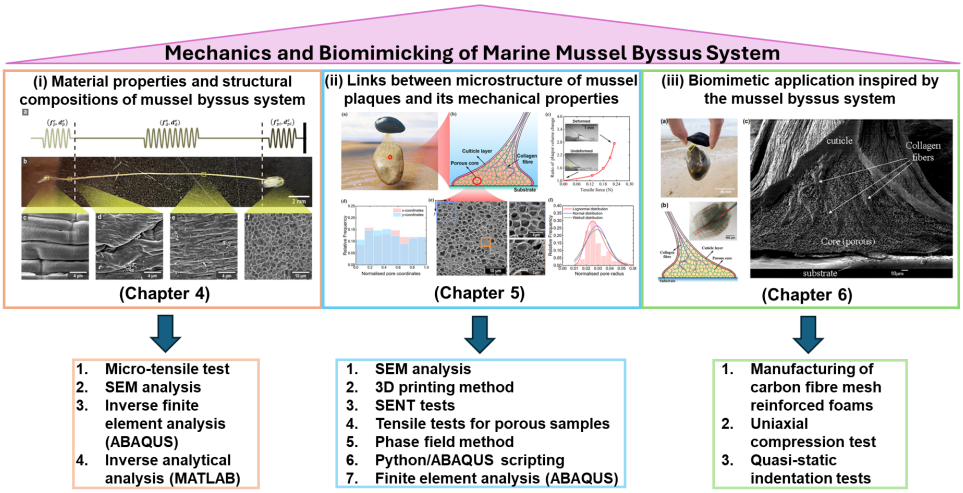


Figure 3.1: The main aspects and methods to investigate the mechanics and biomimicking of marine mussel byssus system [8, 9].

Study 1: The first study aims to determine the mechanical behaviours and structural compositions of the mussel byssus system's main components, including the proximal thread, distal thread, and adhesive plaques. Scanning Electron Microscopy (SEM) and micro-tensile testing were employed to map the microstructure and tensile properties of these components. This foundational study informed the subsequent investigations by providing the necessary material parameters for both analytical models and numerical simulations. These findings were used to develop inverse methodologies for determining material properties based on observed deformations under tensile loading, which was a critical step toward understanding the mechanics of the byssus system under various forces.

Study 2: The second study extended the knowledge from Study 1 by focusing on the mussel plaque's unique microstructure, specifically its hier-

archical porosity. The plaque's microstructure plays a critical role in its mechanical performance, particularly in how it dissipates energy and withstands stress. In this study, advanced SEM techniques were used to capture the plaque's pore distribution and hierarchical structure. Representative Volume Elements (RVEs) were generated to model the microstructure, and phase-field modelling was employed to simulate failure mechanisms within these RVEs. This study was essential in linking the microstructural details to the macroscopic mechanical behaviour of the plaque, providing insights that informed the third study's biomimetic applications.

Study 3: The final study applied the understanding gained from Studies 1 and 2 to develop and test a biomimetic material inspired by the mussel byssus system. The composite material, made from carbon-fibre mesh reinforced LLDPE foam, mimicked the thread-plaque interaction by embedding high-strength fibres within a deformable matrix. The quasi-static indentation (QSI) tests conducted in this study evaluated how different configurations of the fibre mesh and foam responded to low-velocity impact, providing insights into how the plaque's structure could inspire novel materials. This biomimetic approach aimed to harness the mechanical advantages seen in the mussel byssus system, demonstrating the potential for real-world applications in engineered materials.

By structuring these studies in a step-by-step manner, this thesis moves from characterisation of the natural system to the development and testing of biomimetic designs. Each study builds on the insights of the previous one, providing a cohesive narrative that links the mechanics of the mussel byssus system with its potential engineering applications.

3.2 Limitations

While the general methodologies developed in this thesis provided valuable insights into the mechanics and biomimetic potential of the mussel byssus system, it is essential to acknowledge their limitations. The following is a summary of these limitations, with more specific details presented in Chapters 4-6:

- Chapter 4 - (1) The three components of the mussel byssus system were simplified as individual materials, which might not fully capture the complex behaviour of the mussel byssus system. Further investigation into the material difference between the cuticle layer and inner cores could enhance the accuracy of the inverse methodology. (2) The optimisation metrics (deformed plaque shapes) were 2D images, which might be less accurate than comprehensive 3D images. (3) The detachment process of the mussel plaque was idealised to follow a circular shape and only occur at a fixed tensile displacement. The idealisation might affect the model's accuracy and can not capture the full dynamic detachment process of mussel plaque. (4) The failure of the mussel byssus system was not considered in this research. (5) The hyperelastic material constitutive models were applied to represent the tensile materials properties of the components of the mussel byssus system. However, the mussel byssus system is not hyperelastic; we only applied the hyperelastic materials model to represent their behaviour before failure. The model cannot be used to analyse the failure behaviour of the mussel byssus system.

- Chapter 5 - (1) The SEM analysis for the mussel plaques was two-dimensional, which might not capture the full 3D structure characteristics of the mussel plaque core. (2) The destructive process of the

SEM analysis might affect the accuracy of the obtained pore distribution of the plaque core. (3) The 2D porous RVEs applied in this study were only for qualitative analysis. (4) The irregular pores within the mussel plaques were simplified to be circular in the 2D porous RVEs to obtain the distribution parameters (size and location) and porosity. This may not fully capture the geometric characteristics within the plaque core and affect the value of the distribution parameters and porosity. (5) Meanwhile, the multi-scale 2D porous RVEs was an approximation of the hierarchical porous structure of mussel plaques rather than an accurate replication. (6) Due to difficulties obtaining the material properties of the mussel plaque core, a 3D printing material was used as the parent material. Different conclusions might be reached if the actual plaque material properties were used. (7) Due to the manufacturing limitation, the distribution parameters obtained from the SEM analysis were scaled from micrometres to millimetres, but the scalability effects were unclear. (8) Relatively small dataset was used for the statistical analysis in this study (400 cases), which was constrained by the computational demands of running each case. Due to the complexity of the model, each simulation run required significant computational resources and extended runtime, limiting the total number of cases that could feasibly be executed within the available time and computational capacity. Future work could address this limitation by leveraging improved computational infrastructure or optimizing the model to reduce the time per run, allowing for a more extensive dataset to draw stronger statistical conclusions.

- Chapter 6 – (1) Due to the experimental condition limitations, we only manufactured the LLDPE foams with carbon fibre mesh embedded in them rather than accurately replicating the structure of

high-strength mussel thread fibres embedded in a highly deformable mussel plaque foam core. (2) The manufacturing process and sample preparation might result in variations between samples. (3) This study's sample thickness, fibre mesh sizes and indenter sizes were unchanged. Investigating different sizes may facilitate a more comprehensive understanding of the size-related effects on QSI behaviours. (4) Only four configurations of fibre mesh reinforcement (top, middle, bottom, and double-reinforced) were analysed in this chapter. More varied configurations and multi-layer reinforcements might facilitate a more profound comprehension of the optimal reinforcement strategies.

3.3 Summary

This chapter outlines the methodologies employed to investigate the mechanics of the mussel byssus system and explore biomimetic applications inspired by its unique structure. The three studies are designed to build upon one another, moving from the characterization of the natural system to the development of bio-inspired composite materials. Each study provides critical insights that form the foundation for the next, creating a cohesive research narrative. The limitations discussed highlight areas for further exploration, particularly in refining the models and expanding the range of biomimetic designs tested.

Chapter 4

Determining mechanical behaviours of the constituents of the mussel byssus system

Publication Information

Title	Determining hyperelastic properties of the constituents of the mussel byssus system
Author	Yulan Lyu, Yong Pang, Wei Sun, Tao Liu*
Journal	Soft Matter
Status	Published (https://doi.org/10.1039/D3SM01677C)
Year	2024

4.1 Introduction

The mussel plaque within the mussel byssus system (Figure 4.1b) can achieve a strong adhesive strength in wet conditions [5, 135, 136]. Therefore, scientists have conducted numerous studies on the chemical composition of mussel plaques [22, 69, 137], inspiring the development of advanced adhesive materials in medical and engineering fields [5]. For example, six main mussel foot proteins (MFPs) were identified in mussel plaques, which play an essential role in maintaining adhesion at the plaque-substrate interface and establishing connections between threads and plaques [22, 69, 137]. These MFPs contain high levels of the amino acid 3,4-dihydroxyphenylalanine (DOPA), which forms solid and reversible bonds with various surfaces and is an essential component of adhesive chemistry [137]. Meanwhile, studies have also been carried out to investigate the mechanical behaviour of mussel plaques [6, 26, 27, 30, 88, 138]. Desmond et al. (2015) analysed the adhesive performance of mussel plaques subjected to directional tension and summarised three different failure modes: adhesive, interior cohesive, and exterior failure [6]. Based on this fundamental research, Pang et al. (2023) further demonstrated that the failure modes of mussel plaques could be changed by the pull angle or the stiffness of the substrate [9].

Furthermore, as researchers delved deeper into the mussel byssus system, the mechanical behaviours of the constituents of the mussel threads were also revealed. The mussel thread comprises a distal and a proximal portion. Each portion has different compositions and distinct mechanical behaviours that enable mussels to resist dynamic loads and effectively dissipate energy [26, 139]. Specifically, preCol-D and preCol-P, two pre-pepsinized collagens, exhibit a prominent presence in the distal and proximal portions, respectively, potentially leading to different mechanical characteris-

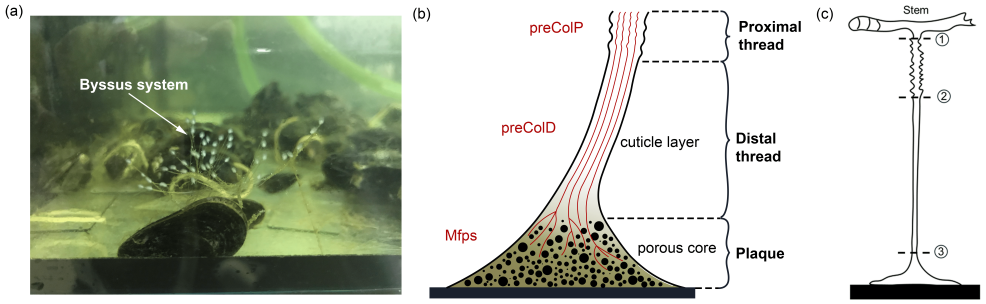


Figure 4.1: (a) Mussel byssus system showing the threads and plaques, (b) a schematic illustration of a single mussel byssus structure and its protein composition, and (c) a schematic diagram of sample cutting positions: cutting position ① for collecting the whole mussel byssus system samples, ① and ③ for collecting thread samples, ② and ③ for collecting distal portion samples.

tics [2, 25, 55]. Gosline and Carrington (2004) revealed that the distal portion of M. californianus mussels can extend approximately half the length of the proximal portion while demonstrating nearly twice the strength and fifty times the stiffness [27]. Furthermore, when subjected to tension, the proximal portion does not exhibit a prominent point of failure, whereas the distal portion experiences four distinct stress regimes: elastic, plateau, hardening, and ultimate failure [26, 27]. Additionally, researchers have also performed cyclic loading tests to analyse the self-healing mechanism of mussel threads [43, 88, 97]. Reversible sacrificial bonds between proteins and metals are widely recognised to play a crucial role in the self-healing process of mussel threads [19, 96, 140, 141].

In order to understand the complex mechanics of the mussel byssus system, recent studies have established robust experimental methods to characterise its tensile properties, focusing primarily on the entire thread-plaque system, the mussel thread or solely on its distal portion [13, 27, 28]. Nevertheless, mechanical properties of the proximal portion or plaque portion have yet to be solely studied due to geometry limits and fragility when subjected to tensile loads [26]. Notably, a fundamental nonlinear spring model was in-

troduced by Waite et al. (2019) to obtain the spring constant and Young's modulus for the plaque [133]. However, these material parameters were obtained by simplifying the stress-strain curve of the combined distal and plaque system into three linear regions [133]. Given the similarity between the nonlinear stress-strain behaviour exhibited by mussel threads and the tensile behaviour observed in rubber materials before failure [90], the difference in calculating the modulus of the distal and plaque portions by simplifying the overall response to linear is non-negligible. Furthermore, the study has not analysed stress-strain curves for the plaque and distal portion separately [133]. Therefore, further investigations on the individual contributions of the distal portion and the plaque to the overall stress-strain response are necessary.

In the present study, we first investigated the microstructure of three different portions within the mussel byssus system and established correlations between the microstructure and mechanical behaviour. Micro-tensile tests were then performed to obtain tensile force-displacement curves for the distal portion, the entire thread (proximal and distal portions), and the entire plaque-thread system. Meanwhile, the side view of plaque deformation was recorded to verify the inverse finite element (FE) approach. Finally, the analytical and FE inverse methods were applied to identify the mechanical behaviours of the proximal and plaque portions. We validated the application of analytical and FE inverse methods in obtaining mechanical behaviours for each of the three portions within the mussel byssus system and determined material constitutive models of those portions. The application of the FE inverse approach to obtain the potential plaque bottom surface detachment radius was also discussed in this research. These studies offer demonstrable evidence of the applicability of inverse methods in the analysis of multi-phase biomaterials and provide insight into the me-

chanical behaviour of each portion of the mussel byssus system for future bio-mimicking.

4.2 Material and methods

4.2.1 Sample preparation procedure

Micro-tensile test sample preparation.

Blue mussels (Mytilus edulis) were collected from the coast of Hunstanton in England and kept in a water tank filled with flowing and oxygen-rich seawater at temperatures between 8°C and 10°C. The collected mussels of 3-5 cm in length were tied to 50×50 mm transparent acrylic sheets to allow plaque deposition (see Appendix C.1). Three different sample types were obtained for micro-tensile testing. The first type comprised whole mussel byssus systems, including an adhesive plaque, distal thread and proximal thread. These were collected by severing mussel threads close to the mussel body using dissecting scissors (Figure 4.1c). The second sample type is mussel threads, including both distal and proximal portions, separated from the adhesive plaques using blades (Figure 4.1c). The third type exclusively encompassed the distal portions of mussel threads, collected using dissecting scissors (Figure 4.1c).

Scanning electron microscopy (SEM) analysis.

The SEM analysis was conducted to investigate the microstructures of the mussel byssus system. The threads and plaques were cut using dissecting scissors to prepare the SEM samples separately. The samples of the

byssal threads and plaques were fixed in a 3.7% formaldehyde and 2.5% glutaraldehyde solution for approximately four hours and stored in Milli-Q water for three days at a temperature of 4°C. The samples were first dehydrated in ethanol at increasing concentrations of 50% (2 times), 70% (2 times), 90% (2 times) and 100% (3 times) and then further dried in hexamethyldisilane (HDMS) 2 times for 5 mins each [16]. After dehydration and drying, samples were sputter coated with 10 nm thick iridium for 120 s using Quorum Q150V Plus and imaged in JEOL 7100F FEG-SEM using an accelerating voltage of 5 kV.

4.2.2 Micro-tensile tests

Two types of micro-tensile tests, plaque tension (Figure 4.2b) and thread tension (distal threads and whole threads) (Figure 4.2c), were conducted on a customised micro-tensile experimental setup (Figure 4.2a). For thread tests, mussel threads were held between two tweezers. The lower tweezer was replaced by an acrylic sheet to which mussel plaques were attached for plaque tests. The upper tweezer is connected to a load cell (Honeywell Model 34, 1000g-10 LBS) to record the loading force. The linear actuator (Thomson MLA11A05) connected to the load cell applies the directional tension to the mussel thread at a slow loading speed of 0.25mm/s to measure the quasi-static tensile responses, which are not sensitive to further reduction of loading speed [142]. The linear actuator is powered by a micro-stepping drive (Kollmorgen P5000) connected to the power supply. A monochrome camera (Thorlabs DCC1545M, 1280 x 1024 pixels, 25 fps), lens system (Navitar 12x Macro Zoom) and mirror were positioned on the acrylic plate's side to record the side view of the plaque deformation process under tension.

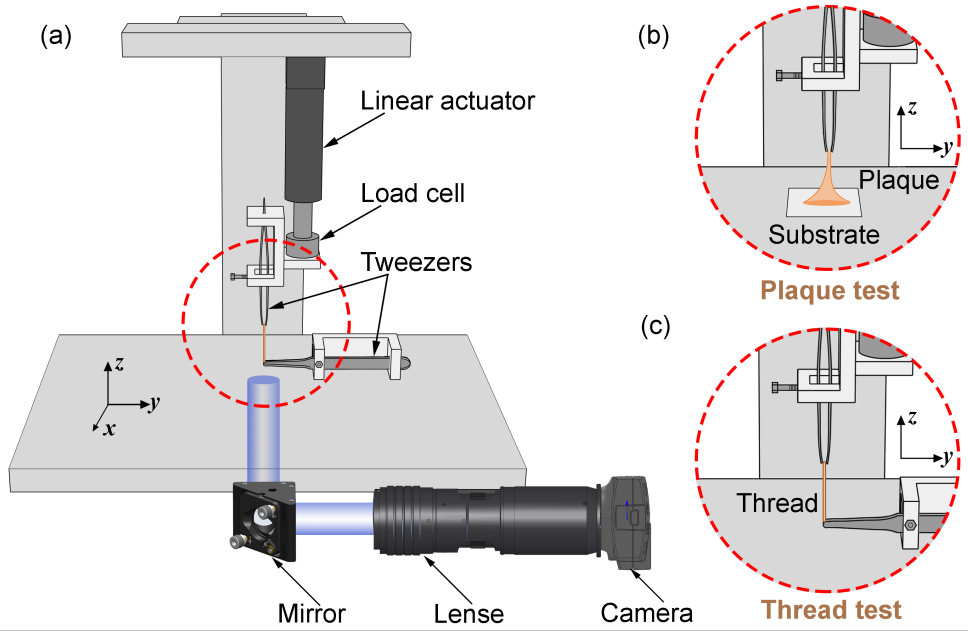


Figure 4.2: (a) Schematic illustration of a customised micro-tensile experimental setup, (b) focused plaque test setup, and (c) focused thread test setup.

4.2.3 Finite element (FE) forward modelling for mussel plaque

A 3D FE model of the mussel plaque was created using ABAQUS/Standard based on the actual measurement from the experiment (Figure 4.3a and c). The diameter of the upper surface and the height of the mussel plaque are approximately 100 μm and 335 μm, respectively (Figure 4.3a). Tensile loads perpendicular to the surface were applied to the upper surface of the plaque using displacement control. The plaque was modelled with 4-node 3D tetrahedral elements in ABAQUS notation (C3D4H elements). The boundary condition of the bottom surface for the plaque model was assumed first to be fully fixed. The Neo-Hookean model was applied to present the mechanical behaviours of mussel plaque. The more detailed equations of this material model can be seen in Section 4.3.1. The mechanical behaviours of the mussel plaque model were iterated in the inverse optimisation algorithm until the tensile force-displacement curve, and the

deformed shapes derived from the FE model synchronised with the results obtained experimentally.

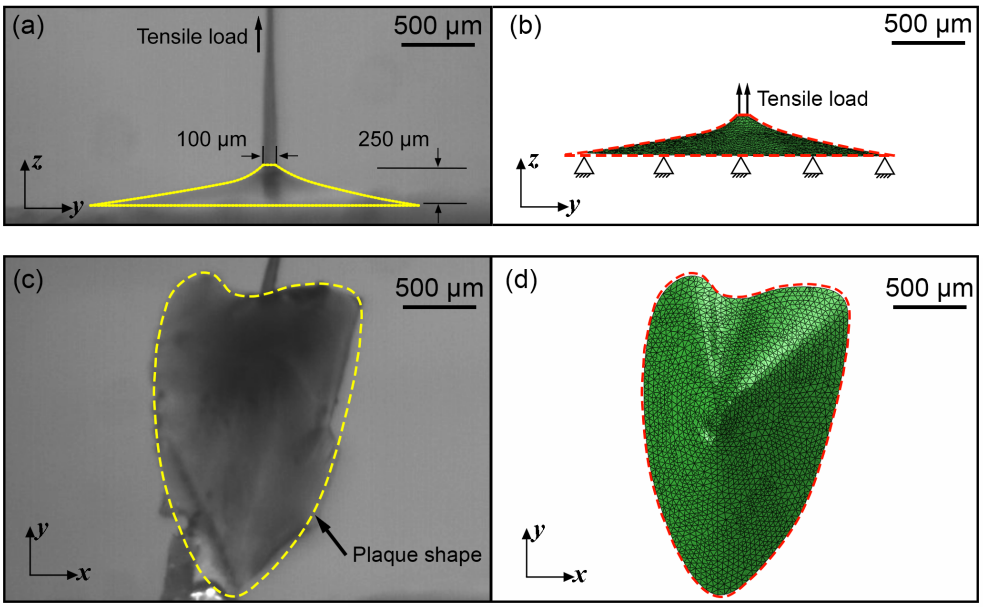


Figure 4.3: (a) Side view of the mussel plaque, (b) side view of FE model of the mussel plaque, (c) bottom view of the mussel plaque, and (d) bottom view of the FE model of the mussel plaque, all under undeformed configuration.

4.2.4 Fundamental of inverse approaches

It was assumed that within a composite material comprising a series of sub-materials, one unidentified sub-material with unknown material parameters exists. Therefore, the inverse method can be applied to identify the mechanical behaviours of the unknown sub-material by simplifying the composite as a series spring system (Figure 4.4a).

The total number of sub-materials was assumed to be p, where the material parameters of the sub-materials with number $p-1$ are known (Figure 4.4a). Therefore, three main inputs in the analytical inverse approach were as follows:

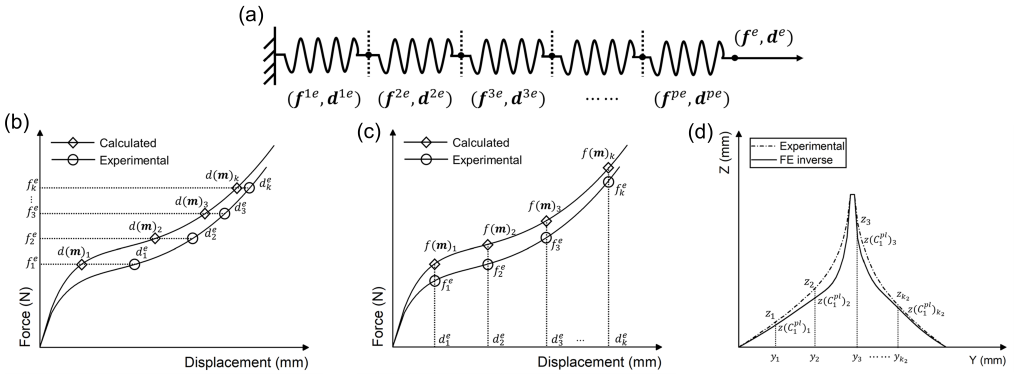


Figure 4.4: (a) Schematic diagram of the simplified spring system, (b) schematic representation of the principle of the inverse method using displacement as a metric, (c) schematic representation of the principle of the inverse method using force as a metric, and (d) schematic of the deformed shape optimisation approach.

1. The experimental force-displacement data of the overall spring system $(\boldsymbol{f}^e, \boldsymbol{d}^e)$, where $\boldsymbol{f}^e = [f_1^e, f_2^e, f_3^e, \cdots, f_k^e]^T$, $\boldsymbol{d}^e = [d_1^e, d_2^e, d_3^e, \cdots, d_k^e]^T$, k is the number of data points obtained from the force-displacement curves (Figure 4.4b and c).

2. Material parameters of known sub-materials $\boldsymbol{\omega}_i$, where i=1, 2, 3, $\cdots$, $p-1$.

3. Guessing material parameters of the unknown sub-material $\boldsymbol{m} = [m_1, m_2, m_3, \cdots, m_q]^T$, where q is the number of material parameters for the unknown sub-material.

As the spring system is compounded in series, the tensile force of the overall spring system should be equal to the tensile force of any sub-material, and the tensile displacement of the overall spring system should equal to the sum of the elongations of all sub-materials:

$$\boldsymbol{f}^e = \boldsymbol{f}^{1e} = \boldsymbol{f}^{2e} = \ldots = \boldsymbol{f}^{pe}$$

$$\boldsymbol{d}^e = \boldsymbol{d}^{1e} + \boldsymbol{d}^{2e} + \cdots + \boldsymbol{d}^{pe} \tag{4.1}$$

Because the material parameters $\boldsymbol{\omega}_i$, material constitutive equations and sizes of the $p-1$ sub-materials were assumed to be known, the elongations of these sub-materials can be calculated based on Eq. 4.1. Meanwhile, the elongation of the unknown sub-material $\boldsymbol{d}^u(\boldsymbol{m})$ can also be calculated using the guessing material parameters $\boldsymbol{m}$, assumed material constitutive equation, measured sizes and the force of unknown sub-materials $\boldsymbol{f}^u(\boldsymbol{m}) = \boldsymbol{f}^e$. Notably, $\boldsymbol{d}^u(\boldsymbol{m})$ and $\boldsymbol{f}^u(\boldsymbol{m})$ denote their values are functions of $\boldsymbol{m}$, and the rule applies to subsequent arguments containing $\boldsymbol{m}$ in parentheses.

Therefore, the displacement of the overall spring system from the analytical inverse approach $\boldsymbol{d}(\boldsymbol{m})$ will be:

$$\boldsymbol{d}(\boldsymbol{m}) = \boldsymbol{d}^1 + \boldsymbol{d}^2 + \cdots + \boldsymbol{d}^{p-1} + \boldsymbol{d}^u(\boldsymbol{m}) \tag{4.2}$$

where $\boldsymbol{d}^1, \boldsymbol{d}^2, \cdots, \boldsymbol{d}^{p-1}$ are the elongation vectors for known sub-materials calculated from the known material parameters $\boldsymbol{\omega}_i$, material constitutive models, measured sizes and experimental forces.

Thus, the residual vector $\boldsymbol{F}(\boldsymbol{m})$ based on the guessing material parameters $\boldsymbol{m}$ can be defined as (Figure 4.4b):

$$\boldsymbol{F}(\boldsymbol{m}) = \boldsymbol{d}^e - \boldsymbol{d}(\boldsymbol{m}) = [F_1(\boldsymbol{m}), F_2(\boldsymbol{m}), F_3(\boldsymbol{m}), \ldots, F_k(\boldsymbol{m})]^T \tag{4.3}$$

If the force is used as the optimisation metrics, the residual vector $\boldsymbol{F}(\boldsymbol{m})$ can be determined as (Figure 4.4c):

$$\boldsymbol{F}(\boldsymbol{m}) = \boldsymbol{f}^e - \boldsymbol{f}(\boldsymbol{m}) \tag{4.4}$$

where $\boldsymbol{f}(\boldsymbol{m})$ is the force vector of the overall spring system based on the guessing material parameters $\boldsymbol{m}$ from the analytical inverse approach.

The optimisation process is achieved by applying the nonlinear least squares estimation function **lsqnonlin** within the Matlab Optimisation Toolbox [143]. This method effectively addresses curve-fitting problems characterised by using the following form of nonlinear least-squares [143]:

$$\min_{\boldsymbol{m}} \|\boldsymbol{F}(\boldsymbol{m})\|_2^2 = \min_{\boldsymbol{m}} \left(F_1(\boldsymbol{m})^2 + F_2(\boldsymbol{m})^2 + F_3(\boldsymbol{m})^2 + \cdots + F_k(\boldsymbol{m})^2\right) \quad (4.5)$$

The lower and upper bounds **lb** and **ub** were set to limit the value ranges of material parameters $\boldsymbol{m}$ and thus accelerate the inverse approach. The functional tolerance θ is initially set to 0.01 in the 'options' and can be changed to the desired degree of precision [143]. When the final change in the sum of squares relative to its initial value is less than the value of the function tolerance, the **lsqnonlin** will stop, and the optimised material parameters $\boldsymbol{m}^*$ will be obtained (Figure 4.5):

$$\min_{\boldsymbol{m}} \|\boldsymbol{F}(\boldsymbol{m})\|_2^2 \leq \theta \quad (4.6)$$

However, if the shape of the material is irregular, the analytical inverse approach is no longer applicable, and the FE-based inverse approach is needed. The ".inp" file for ABAQUS was first written, including the material geometry, known and guessed material parameters, material constitutive models and boundary conditions. A post-processing Python script was then created to extract force-displacement results based on guessing material parameters from the ABAQUS ".odb" file. The remaining optimisation process is consistent with the analytical inverse method by applying **lsqnonlin**, meaning that when Eq. 4.6 is satisfied, the optimised material parameters $\boldsymbol{m}^*$ will be obtained (Figure 4.5).

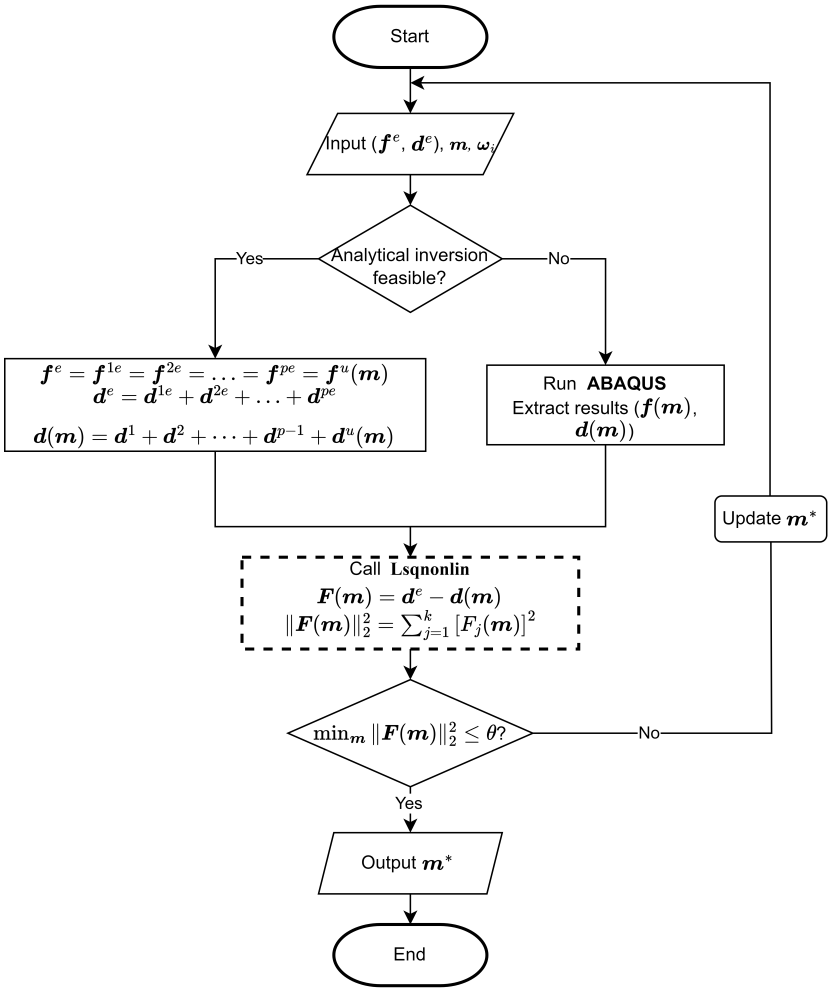


Figure 4.5: Flow chart of both analytical inverse and FE-based inverse procedures.

4.3 Mussel byssus system material constitutive models and inverse procedure

4.3.1 Material constitutive models

Based on the characteristics of the stress-strain curves of the distal and proximal threads and the force-displacement curves of the entire byssus system in the previous literature [6, 26, 27, 91], different materials constitutive models were assumed to present plaques, distal threads and proximal threads, respectively. The incompressible Ogden's model was applied

to the distal threads because the shape of the strain-stress curves for the distal threads has characteristics similar to those of the Ogden's model curve. Similarly, the constitutive model of both the proximal portion and the plaque was assumed to be the incompressible Neo-Hookean material model due to the resemblance of the curve shape.

Notably, in this research, to simplify the calculation process, the cross-sectional area of the thread was assumed to remain unchanged during the uniaxial tensile test. As a result, the nominal stress was considered to be equal to the true (Cauchy) stress. While it is acknowledged that the nominal and true stresses are different in most cases, this assumption was necessary to simplify the modeling for this phase of the study. Regarding the incompressibility assumption for the threads and plaque, experimental verification was challenging due to limitations in available data. Therefore, as a reasonable starting point, the Ogden and Neo-Hookean models were employed under the assumption of incompressibility. This choice reflects an initial approximation and does not imply that the materials are strictly incompressible or that the cross-section is unchanged during deformation. Future studies should focus on addressing these aspects more comprehensively, particularly when applying hyperelastic models to simulate the complex behaviour of such materials.

The strain energy potential W of the three-order Ogden model is expressed in terms of principal stretches as follows [144]:

$$W = \sum_{\beta=1}^{N} \frac{2\mu_\beta}{\alpha_\beta^2} \left(\bar{\lambda}_1^{\alpha_\beta} + \bar{\lambda}_2^{\alpha_\beta} + \bar{\lambda}_3^{\alpha_\beta} - 3 \right) \tag{4.7}$$

where N is the order of strain energy potential ($N = 3$), μ_β and α_β ($\beta = 1, 2, 3$) are six material constants. $\bar{\lambda}_1$, $\bar{\lambda}_2$ and $\bar{\lambda}_3$ are the distortional principal stretches which can be calculated using principal stretches

$\bar{\lambda}_\eta = J^{-\frac{1}{3}} \cdot \lambda_\eta (\eta = 1, 2, 3)$, J is the total volume ratio.

Meanwhile, the strain energy potential of the incompressible Neo-Hookean material model is given below [145]:

$$W = C_1 \left(\bar{\lambda}_1{}^2 + \bar{\lambda}_2{}^2 + \bar{\lambda}_3{}^2 - 3 \right) \tag{4.8}$$

where C_1 is a material constant.

Tensile tests were assumed to be uniaxial. Therefore, the uniaxial stress σ and stretch λ for Ogden's model can be expressed as

$$\sigma = \sum_{\beta=1}^{3} \frac{2\mu_\beta}{\alpha_\beta} \left[\lambda^{\alpha_\beta} - \left(\frac{1}{\sqrt{\lambda}} \right)^{\alpha_\beta} \right] \tag{4.9}$$

The uniaxial stress σ and stretch λ for Neo-Hookean hyperelastic model are defined as shown below:

$$\sigma = 2C_1 \left(\lambda - \frac{1}{\lambda^2} \right) \tag{4.10}$$

4.3.2 Application of inverse approaches to mussel byssus system

Problem definition.

The shorter length of the proximal portion compared to the distal portion of threads and the irregular shape of mussel plaques increase the difficulty of the micro-tensile tests. Therefore, analytical and FE inverse approaches were employed to obtain their mechanical behaviours.

Analytical inverse approach for the proximal thread.

The three portions of the mussel byssus system were simplified as a spring system in series. Tensile force and displacement data for the distal portion $(\boldsymbol{f}_d^e, \boldsymbol{d}_d^e)$ was obtained from the micro-tensile tests for the distal portion, and the stress-strain data $(\boldsymbol{\sigma}_d^e, \boldsymbol{\varepsilon}_d^e)$ can be further calculated by

$$\boldsymbol{\sigma}_d^e = \frac{\boldsymbol{f}_d^e}{\pi r_d^2}$$

$$\boldsymbol{\varepsilon}_d^e = \frac{\boldsymbol{d}_d^e}{l_d} \tag{4.11}$$

where r_d and l_d are the radius and length of the distal portion before tension.

Based on the experiment data and the Ogden model (Eq. 4.9), six material parameters of the distal portion (μ_β, α_β), ($\beta = 1, 2, 3$) can be determined using a simple analytical or FE-based inverse approach shown in Figure 4.5 and were used as input for the further analytical inverse approach.

Next, the tensile force and displacement data of the whole thread (distal and proximal portions) $(\boldsymbol{f}_t^e, \boldsymbol{d}_t^e)$ was also obtained from micro-tensile tests for the whole thread. Based on Eq. 4.1, the following equations can be obtained:

$$\boldsymbol{f}_t^e = \boldsymbol{f}_p^e = \boldsymbol{f}_d^e$$

$$\boldsymbol{d}_t^e = \boldsymbol{d}_p^e + \boldsymbol{d}_d^e \tag{4.12}$$

where $\boldsymbol{f}_p^e = \left[(f_p^e)_1, (f_p^e)_2, \cdots, (f_p^e)_k\right]^T$ and $\boldsymbol{f}_t^e = \left[(f_t^e)_1, (f_t^e)_2, \cdots (f_t^e)_k\right]^T$ are the tensile force vectors of the proximal portion and the distal portion, respectively. $\boldsymbol{d}_p^e = \left[(d_p^e)_1, (d_p^e)_2, \cdots, (d_p^e)_k\right]^T$ and $\boldsymbol{d}_t^e = \left[(d_t^e)_1, (d_t^e)_2, \cdots, (d_t^e)_k\right]^T$ are the elongation vectors of the proximal portion and the distal portion, respectively.

Therefore, the elongations of the distal portion can be calculated based on Eq. 4.9, 4.11 and 4.12, and the six material parameters obtained from the previous distal portion tensile tests:

$$\frac{(f_t^e)_j}{\pi r_d^2} = \sum_{\beta=1}^{3} \frac{2\mu_\beta}{\alpha_\beta} \left[\left(\frac{(d_d^e)_j + l_d}{l_d} \right)^{\alpha_\beta} - \left(\frac{1}{\sqrt{\frac{(d_d^e)_j + l_d}{l_d}}} \right)^{\alpha_\beta} \right] \tag{4.13}$$

where $j = 1, 2, 3, \cdots, k$.

Meanwhile, the elongation of the proximal portion $\boldsymbol{d}(C_1^p)_p$ based on the given material constant C_1^p can be calculated in the analytical inverse approach based on Eq. 4.10 and 4.12:

$$\left(d\left(C_1^p\right)_p \right)_j = l_p \left(\frac{(f_t^e)_j}{2\pi C_1^p r_p^2} + \frac{1}{\left(\frac{\left(d\left(C_1^p\right)_p \right)_j + l_p}{l_p} \right)^2} - 1 \right) \tag{4.14}$$

where r_p and l_p are the radius and length of the proximal portion before tension. $\left(d\left(C_1^p\right)_p \right)_j$ is one data point within $\boldsymbol{d}(C_1^p)_p$ and a function of C_1^p. (The rule also applies to subsequent arguments containing C_1^p in parentheses)

As a result, the tensile displacement of the whole thread based on the given material constant C_1^p can be expressed as

$$\boldsymbol{d}(C_1^p)_t = \boldsymbol{d}(C_1^p)_p + \boldsymbol{d}_d^e \tag{4.15}$$

The residual vector $\boldsymbol{F}(C_1^p)$ based on the given material constant C_1^p then

can be defined as

$$\boldsymbol{F}(C_1^p) = \boldsymbol{d}_t^e - \boldsymbol{d}(C_1^p)_t = [F_1(C_1^p), F_2(C_1^p), F_3(C_1^p), \ldots, F_k(C_1^p)]^T \quad (4.16)$$

If the tensile force was used as metrics, the residual vector $\boldsymbol{F}(C_1^p)$ can be expressed as

$$\boldsymbol{F}(C_1^p) = \boldsymbol{f}_t^e - \boldsymbol{f}(C_1^p)_t \quad (4.17)$$

lsqnonlin was applied for parameter optimisation as Section 4.2.4, and the functional tolerance θ was initially set as 0.01. **lsqnonlin** will stop when the following convergence criterion is satisfied:

$$\min_{C_1^p} \|\boldsymbol{F}(C_1^p)\|_2^2 \leq \theta \quad (4.18)$$

FE-based inverse approach for the mussel plaque.

The FE inverse approach was employed as the irregular shape of mussel plaques makes the above analytical inverse approach not applicable. Micro-tensile tests were first performed on the combined distal and plaque portions because it was difficult to perform experiments on the plaques themselves. Based on Eq. 4.1, the force of the mussel plaque $\boldsymbol{f}_{pl}^e$ can be obtained from the experiment:

$$\boldsymbol{f}_{pl}^e = \boldsymbol{f}_d^e = \boldsymbol{f}_{d+pl}^e \quad (4.19)$$

where $\boldsymbol{f}_d^e$ and $\boldsymbol{f}_{d+pl}^e$ are the tensile force vectors of the distal portion and distal-plaque system, respectively.

Meanwhile, the tensile displacement of the upper surface of the mussel

plaque $\boldsymbol{d}^e_{pl}$ was also measured from the side-view video (Figure 4.11a) to generate the experimental force-displacement data ($\boldsymbol{f}^e_{pl}$, $\boldsymbol{d}^e_{pl}$) as input in the FE inverse approach. The guessing material parameter C_1^{pl} of the mussel plaque was then written on the ABAQUS CAE Interface and updated in **lsqnonlin**. A post-processing Python script was created to extract the force-displacement data ($\boldsymbol{f}(C_1^{pl})_{pl}$, $\boldsymbol{d}(C_1^{pl})_{pl}$) based on the guessing material parameter C_1^{pl} from the ABAQUS .odb file.

The residual vector $\boldsymbol{F}(C_1^{pl})$ and the sum of squared residuals from the force-displacement data based on the guessing material parameter C_1^{pl} can be defined as:

$$\boldsymbol{F}(C_1^{pl}) = \boldsymbol{d}^e_{pl} - \boldsymbol{d}(C_1^{pl})_{pl} = \left[F_1(C_1^{pl}), F_2(C_1^{pl}), \ldots, F_k(C_1^{pl})\right]^T$$

$$\left\|\boldsymbol{F}\left(C_1^{pl}\right)\right\|_2^2 = \sum_{j=1}^{k}\left[F_j\left(C_1^{pl}\right)\right]^2 \tag{4.20}$$

To further optimise the FE inverse approach, the deformed side views of the mussel plaque measured from the experiment were compared with the FE results. It was assumed that the deformed shapes with a total number of k_1 were analysed. For each deformed shape, the leftmost node was set as (0,0) (Figure 4.3a), and nodes with a total number of k_2 were selected on each shape. Graph Grabber v 2.0.1 software was used to obtain the coordinates ($\boldsymbol{y}$, $\boldsymbol{z}$) of selected nodes (https://www.quintessa.org/software). Meanwhile, the coordinates ($\boldsymbol{y}$, $\boldsymbol{z}(C_1^{pl})$) of corresponding nodes based on the guessing material parameter C_1^{pl} were exported from the FE model using a post-processing Python script.

The residual vector $\boldsymbol{F}^s(C_1^{pl})$ of each deformed shape can be expressed as

(Figure 4.4d)

$$\boldsymbol{F}^s(C_1^{pl}) = \boldsymbol{z} - \boldsymbol{z}(C_1^{pl}) = \left[F_1^s(C_1^{pl}), F_2^s(C_1^{pl}), \ldots, F_{k_2}^s(C_1^{pl})\right]^T \tag{4.21}$$

$$\left\|\boldsymbol{F}^s\left(C_1^{pl}\right)\right\|_2^2 = \sum_{h=1}^{k_1}\sum_{g=1}^{k_2}\left[F_g^s\left(C_1^{pl}\right)_h\right]^2 \tag{4.22}$$

The total sum of squared residuals $R(C_1^{pl})$ for both force-displacement curves and deformed shapes is defined below:

$$R(C_1^{pl}) = W_1 \cdot \left\|\boldsymbol{F}\left(C_1^{pl}\right)\right\|_2^2 + W_2 \cdot \left\|\boldsymbol{F}^s\left(C_1^{pl}\right)\right\|_2^2 \tag{4.23}$$

where W_1 and W_2 are the non-negative weights, $W_1, W_2 \in [0, 1]$,
$W_1 + W_2 = 1$. W_1 and W_2 were set to 0.8 and 0.2, respectively, indicating that the accuracy of the force-displacement data is more critical in this research. Their values can be adjusted according to the study interest [146, 147].

lsqnonlin was applied for parameter optimisation as Section 4.2.4, and the functional tolerance θ was initially set as 0.01. The value of θ can be adjusted based on the optimisation condition. **lsqnonlin** will stop when the following convergence criteria are satisfied:

$$\min_{C_1^{pl}}[R(C_1^{pl})] \leq \theta \tag{4.24}$$

The analytical inverse and FE-based inverse procedures specifically for the proximal portion and the plaque portion are summarised in Figure 4.6.

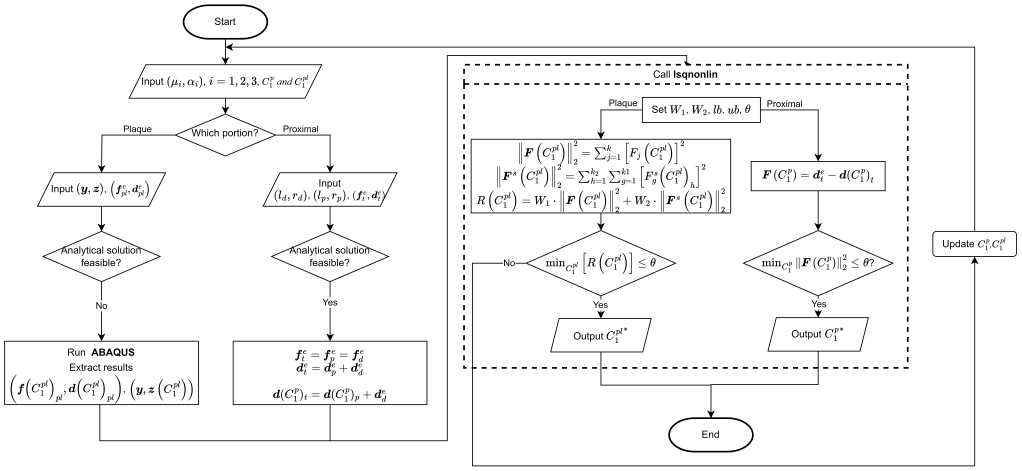


Figure 4.6: Flow chart of determining the mechanical behaviours of the plaque and the proximal portion by using FE-based inverse approach and analytical inverse approach, respectively.

4.4 Results

4.4.1 Microstructures of the mussel byssus system

Four different microstructures from the mussel byssus system were identified by SEM analysis (Figure 4.7c-f). For the proximal portion, it can be seen that numerous folds of various sizes cover almost the entire surface of the proximal portion, and the furrows between the folds are parallel or perpendicular to the longitudinal axis (Figure 4.7c). The surface of the distal portion is smooth, but longitudinal patterns of approximately 1 μm in width can still be seen on the surface (Figure 4.7e). Meanwhile, the surface of the transition part between these two portions has the characteristics of both, with a smoother surface and a reduced number of folds compared to the proximal portion, and longitudinal patterns begin to appear (Figure 4.7d).

Due to the difficulty in identifying the location of the transition portion during the experiments, it was assumed that mussel threads were mainly composed of proximal and distal portions in this research. Furthermore,

the mussel plaque with a porous core structure that is distinctly different from that of the thread is shown in Figure 4.7f. Different microstructural characteristics and protein composition [10, 57, 148] may be the reasons for the difference in mechanical behaviours for different portions and provide evidence for the feasibility of the spring system assumption, which is the main basis of inverse approaches (Figures 4.7a and b).

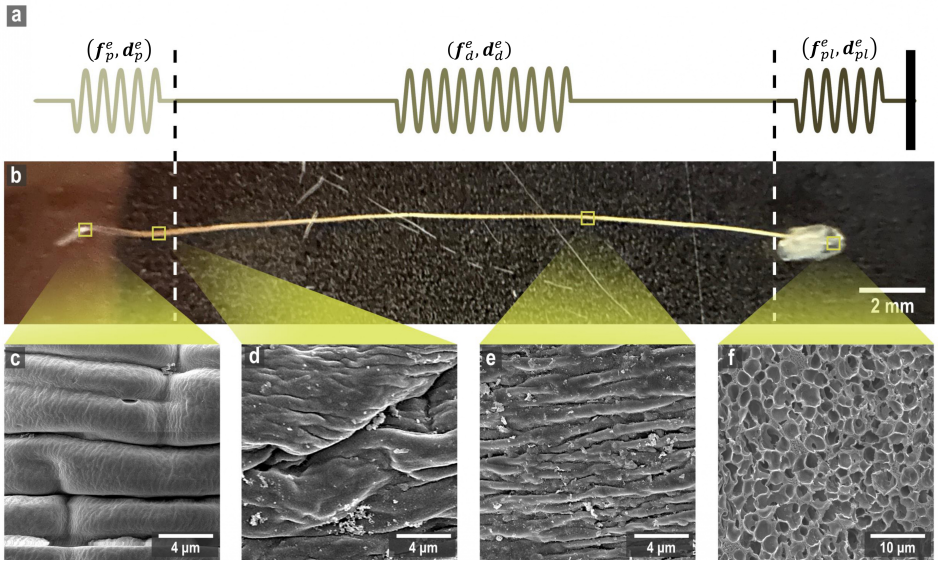


Figure 4.7: (a) The idealisation of the thread-plaque mechanics model, (b) the overall thread-plaque structure, and (c)-(f) the micro-structures of proximal portion, transition portion, distal portion and plaque core, respectively.

4.4.2 Micro-tensile test results

It is evident from Figures 4.8a and b that the force-displacement and strain-stress curves obtained from the tensile tests in the distal portions exhibit different failure points, reflecting the unique characteristics of each thread [28, 89, 93]. Nevertheless, the distal portion tests show consistent failure mechanism patterns, suggesting the applicability of a single material constitutive model to represent the distal portion.

Meanwhile, the force-displacement curves of the combined distal and prox-

imal portions and the combined distal and plaque portions are shown in Figures 4.8c and d, respectively. An inflection point can be found in some of the force-displacement curves of the combined distal and plaque portions (Figure 4.8c), which may indicate that ultimate failure of the combined portions is likely to occur after the yield point of the distal portion. On the contrary, the force-displacement curves of the combined distal and plaque portions did not show an obvious inflection point, suggesting that plaque detachment may occur before the yield point of the distal section. The comparison of Figures 4.8c and d also demonstrates that the failure displacement of the combined distal and proximal portions is larger than the displacement of the combined distal and plaque portions, and the failure force varies from 0.1 N - 0.2 N during these tests.

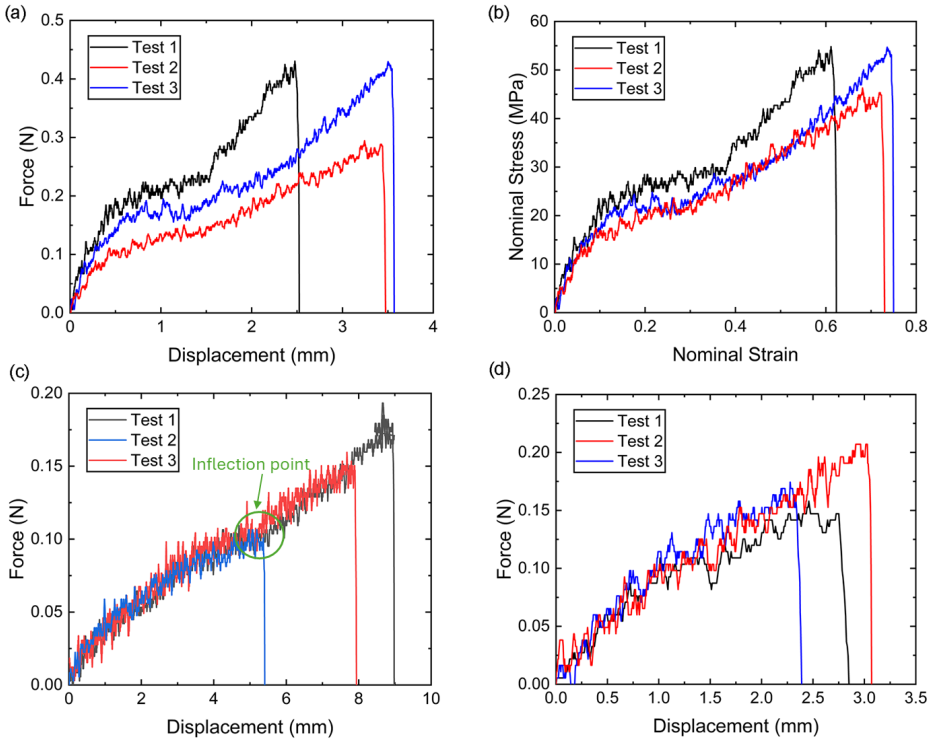


Figure 4.8: (a) The tested distal portion force-displacement curves, (b) the converted nominal stress-strain curves, (c) the tested whole thread (proximal and distal) portion force-displacement curves, and (d) the tested distal-plaque portion force-displacement curves.

4.4.3 mechanical behaviours of individual constituents

mechanical behaviours of the distal portion.

The "fminsearch" method in MATLAB was first used to generate a target curve that closely matched the average curve of the three stress-strain curves of the distal portion (4.8b), as shown in Figure 4.9. The target curve was then used as input to the inverse approach to speed up the inverse calculation. The optimised curves of the analytical and FE inverse approaches with the assumed Ogden model show close agreement with the target curve (Figure 4.9). The mechanical behaviours obtained from both inverse approaches are shown in Table 4.1 and were used as input for the latter proximal and plaque inverse approaches.

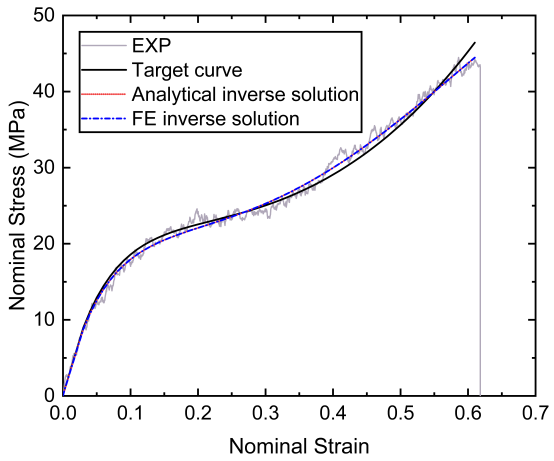


Figure 4.9: The average nominal stress-strain curves of the distal portion obtained by experiment (EXP curve), fitting (target curve) and inverse (analytical and FE inverse curves).

mechanical behaviours of the proximal portion.

The process of optimising the material parameters for the proximal portion followed the method shown in Figure 4.6. Different thread dimensions can

Table 4.1: mechanical behaviours for the distal portion

Material constants	Analytical inverse solution	FE inverse solution
$\mu_1(MPa)$	-529	-528
α_1	7.19	6.69
$\mu_2(MPa)$	425	426
α_2	7.12	6.79
$\mu_3(MPa)$	229	229
α_3	-14.5	-12.4

cause a significant variation in the force-displacement curve. Therefore, instead of using the average experimental value, test 2 was selected from the three thread (proximal and distal) portion force-displacement curves in Figure 4.8a to remove the noise and set it as the target curve. The force-displacement curves from inverse approaches on the basis of the assumed Neo-Hookean model are in good agreement with the experimental result (Figure 4.10). Therefore, the material parameter of the proximal portion C_1^p and residuals from both inverse approaches are given in Table 4.2.

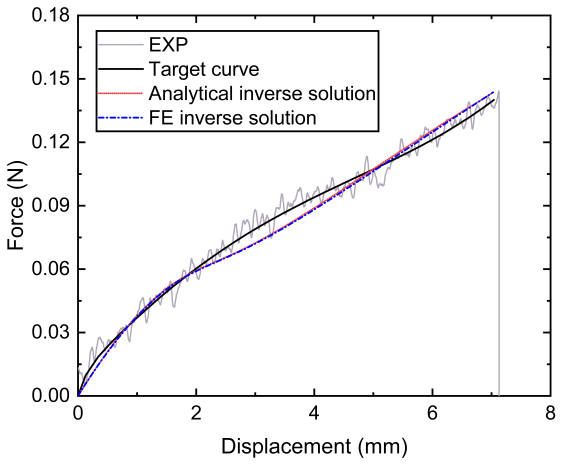


Figure 4.10: Nominal force-displacement curves of the thread (proximal and distal) portion obtained by experiment (EXP curve), fitting (target curve) and inverse (analytical and FE inverse curves).

Table 4.2: Proximal portion material parameter $C_1^p(MPa)$ and the min of the sum of square residuals (N^2)

Inverse methods	$C_1^p(MPa)$	$\min \|\boldsymbol{F}(C_1^p)\|_2^2 (N^2)$
Analytical inverse method	9.16	0.0004
FE-based inverse method	11.2	0.0005

mechanical behaviours of the plaque portion.

Material parameter C_1^{pl} of the plaque portion Due to the complex and challenging nature of conducting tensile tests on the small and fragile mussel plaques, the distal-plaque tensile test results were analysed instead of conducting plaque-only experiments. From the experimental video, the displacement of the plaque portion prior to failure was measured to be 0.25 mm. Subsequently, by applying Eq. 4.19 to the force data obtained from the distal-plaque test 1 (Figure 4.8d), the force-displacement curve for the individual plaque can be constructed, as shown in Figures 4.11b and d. Furthermore, three deformation shapes at different displacements were obtained from test 1 (Figure 4.11a). The leftmost points of the deformed shapes were set as the coordinate origins, and the shapes were further converted into three shape curves using Graph Grabber v 2.0.1 (Figures 4.11c and e).

The experimental force-displacement and shape curves (Figures 4.11b-e) were used as input for the FE inverse approach, then the material parameter for the plaque portion C_1^{pl} was output as 1.2 MPa with a minimum sum of squared residuals 0.137 mm^2 (Table 4.3). The general agreement between the force-displacement curves and the shape curves obtained from the experimental results and the inverse results can be seen in Figures 4.11b and c. However, by carefully comparing the shape curves of the FE and the experiment, it can be observed that the shapes of the FE model with a fully fixed bottom surface showed obvious deformation only in the up-

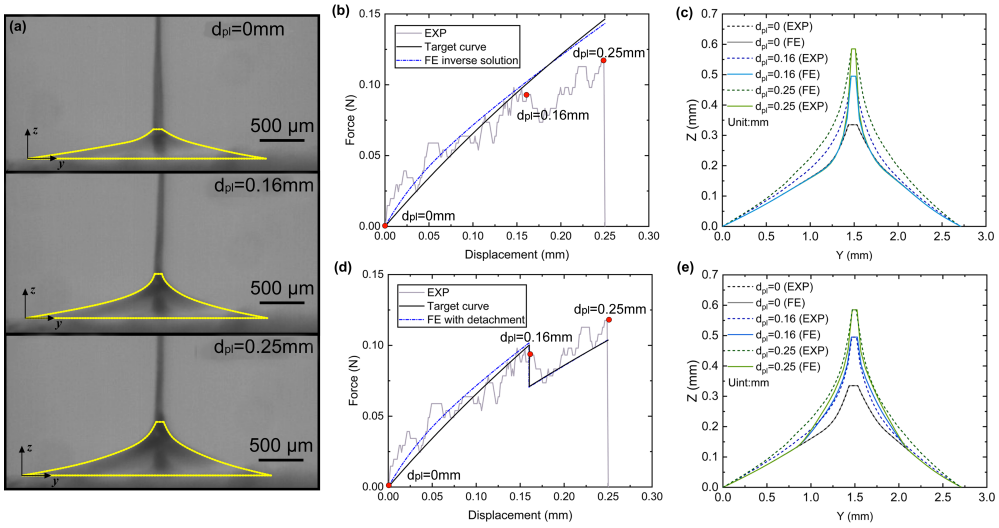


Figure 4.11: (a) The side view of plaque deformation at $d_{pl} = 0mm$, $d_{pl} = 0.16mm$, $d_{pl} = 0.25mm$. (b) The force-displacement curves at $d_{pl} = 0mm, 0.16mm, 0.25mm$ without considering partial detachment at the bottom surface in the FE inverse solution, (c) the deformed shape comparison of the plaque portion at $d_{pl} = 0mm, 0.16mm, 0.25mm$ without considering partial detachment from the bottom surface in the FE inverse solution, (d) the force-displacement curves at $d_{pl} = 0mm, 0.16mm, 0.25mm$ with partial detachment at the bottom surface in the FE inverse solution, and (e) the deformed shape comparison of the plaque portion at $d_{pl} = 0mm, 0.16mm, 0.25mm$ with partial detachment at the bottom surface in the FE inverse solution.

per part (Figure 4.11c). On the other hand, the shapes of the experiment showed a more monolithic deformation, which also occurred in the area of the plaque that is far away from the stretch thread (Figure 4.11c). Meanwhile, after $d_{pl} = 0.16mm$, the experimental curves were slightly lower than the simulated curves (Figure 4.11b). Therefore, the results could indicate a possible partial detachment on the bottom surface at $d_{pl} = 0.16mm$ during the experiment.

Table 4.3: Plaque portion material parameter $C_1^{pl}(MPa)$ and the minimum value of the sum of square residuals (mm^2) from the FE inverse approach

	Inverse output without detachment
C_1^{pl}	1.2
$\min\left[R\left(C_1^{pl}\right)\right]$	0.137

Potential partial bottom surface detachment radius optimisation

In order to further analyse the bottom surface detachment radius at $d_{pl} = 0.16mm$, it was assumed that the detachment area was a circle and that the projection of the centre point on the upper surface to the lower surface was used as the detachment centre point. Furthermore, the material parameter C_1^{pl} was assumed to be the same as $1.2MPa$, and the detachment radius from $d_{pl} = 0.16mm$ to $d_{pl} = 0.25mm$ was assumed to be constant. The updated target force-displacement curve shown in Figure 4.11d was applied as the new input. Meanwhile, the radius of bottom surface detachment was optimised inside the FE inverse approach instead of the material parameter C_1^{pl}. The 3D FE model used within this FE inverse approach was the same as in Section 4.2.3. The only difference was that the fixed boundary conditions at the bottom points within the detachment area were removed at $d_{pl} = 0.16mm$ to simulate the bottom surface detachment during the optimisation process. Specifically, the detachment radius had to be less than the distance from the centre of the detachment to the outer boundary of the bottom surface.

The updated inverse results with detachment can be seen in Figures 4.11d and e with a detachment radius = 0.6 mm and a less minimal sum of squared residuals 0.01 mm^2 (Table 4.4). The FE and experiment deformed shapes at $d_{pl} = 0.16mm$ and $0.25mm$ were more consistent than the previous results (Figures 4.11d and e). The discrepancy between the FE and the experimental deformed shapes at $d_{pl} = 0.25mm$ suggests a possible detachment range greater than 0.6 mm. However, it is important to note that 0.6 mm represents the maximum detachment radius without touching the edge of the bottom surface. This observation suggests that the detachment might be a dynamic process in which the detachment range gradually expands and is not static. Overall, the implementation of shape optimisation

in the mussel plaque's FE inverse approach leads to a more accurate result.

Table 4.4: Bottom surface detachment radius $r_b(mm)$ and the minimum value of the sum of square residuals (mm^2) from the FE inverse approach

	FE inverse approach output with detachment
r_b	0.6
$\min\left[R\left(C_1^{pl}\right)\right]$	0.01

4.5 Discussion

In recent decades, several reports have investigated the tensile stress-strain behaviour of the mussel byssus system as a whole and its distal and proximal portions individually [6, 26, 27, 91]. However, due to the size of the mussel byssus system and the complexity of the biomaterial composition, there are still some challenges to comprehensively understanding its mechanism using experimental or numerical methods. In our study, the analytical and FE inverse approaches were applied for the first time to obtain the mechanical behaviours of the constituents of the mussel byssus system in this investigation, which could simplify the process of obtaining experimentally challenging mechanical behaviours of the mussel byssus system or any other compound material system. The results show that the force-displacement curves based on the identified mechanical behaviours from both inverse approaches are in good agreement with the micro-tensile test results, which demonstrates the feasibility of inverse methods for identifying the mechanical behaviours of biomaterials. Notably, the biological characteristics of mussel plaques contribute to the variability in plaque underside shapes. Even plaques from the same mussel exhibit different structures depending on the temperature or PH levels [16, 21]. This investigation focuses on

the application of the finite element (FE) inverse method, where the selected plaque had a nearly heart-shaped underside. However, in the study of Desmond et al. (2015) or Pang and Liu (2023), the undersides of the plaques showed an oval or square shape [6, 9]. Therefore, the integration of the inverse method with basic mechanical and optical tests is essential for a comprehensive analysis. Furthermore, it is pertinent to highlight that our experimental protocol only applied a stretching angle of 90rather than aligning with the natural growth direction of mussels, as the research focus is to assess the feasibility of inverse methods to obtain the mechanical behaviours of the mussel byssus system. Pang and Liu (2023) have conducted a detailed analysis to explain why the natural growth angle of mussel plaques is close to 15using directional tensile experiments and FE simulations [9]. Additionally, the deformed side shapes and the potential detachment of the plaque bottom surface were also included in the FE inverse approach to further increase the accuracy of the results. Specifically, in the study conducted by Waite et al. (2019), the spring constant and Young's modulus of the mussel plaque were obtained by simplifying the tress-strain curve of the combined distal and plaque system into three linear regions [133], while the consistency between our experimental and inverse curves suggests that the third-order Ogden model may be a more accurate option for characterising the mechanical behaviours of distal threads, and the Neo-Hookean model may be a better choice for describing the mechanical behaviours of both proximal threads and mussel plaques.

In the present study, the tensile behaviour of the different portions of the mussel byssus system, as well as the microstructures of the different portions derived from micro-tensile tests, are also in agreement with the results of previous studies [16, 26, 27, 39]. The unique folds and furrows found in the proximal portion might be one of the reasons why the proximal por-

tion is more deformable than the distal portion, as they allow the proximal portions more room to stretch and expand, helping to dissipate the strain energy (Figures 4.7c and e). Meanwhile, the variety in protein composition could be another reason to explain the differences in the tensile properties of the different portions. The biochemical composition of the mussel byssus system has been well researched, particularly the protein composition and metals [10, 22, 57, 99, 149]. The distal portion is enriched in PreCol-D, whereas the proximal part is enriched in PreCol-P. PreCol-P with elastin-like folding sequences in the flanking domains is embedded in the matrix proteins of the proximal portion to provide greater elasticity. While preCol-D with spider silk-like sequences in the flanking domains could be reinforced with a β-sheet crystalline particle matrix to provide greater strength and toughness in the distal portion [150]. Additionally, the protein compositions of the plaques differ from those of the threads, which are mainly composed of MFPs that help adhesion of the mussel plaque. The mechanical behaviours, chemical composition, and microstructure of these three portions contribute to a better understanding of the mechanism and energy consumption underlying the composite characteristics of the mussel byssus system.

Although identifying the mechanical behaviours of each portion in the mussel byssus system is a significant first step in analysing the mechanism of how mussels remain stable on the seafloor against persistent waves, future investigation is needed once the mechanical behaviours have been obtained. For example, mussel threads are a composite of an external cuticle and a fibrous core, whereas mussel plaques are a composite of a cuticle and a porous core. It is not yet clear how the cuticle layer and core affect tensile behaviour, respectively. Meanwhile, several questions have not been addressed. The failure mechanisms of the mussel byssus system have not

been studied in this research. The potential partial detachment optimisation method in this research provides a potential direction for the future failure mechanisms analysis of the mussel byssus system. The partial detachment process was simplified to occur only at a fixed tensile displacement and follow a circular shape, but the real dynamic detachment at the bottom surface of mussel plaques is more complex. Moreover, the study by Wilhelm et al. (2017) found that due to various forms of microstructural damage, the force-displacement curves of the mussel byssus system under multiple loading cycles showed a hysteresis behaviour, but interestingly the material strength remained comparable to that of the monotonically loaded mussel byssus system [66]. In our research, the hyperelastic material constitute models were applied to describe the mechanical behaviour of the mussel byssus system before failure. However, based on the definition of hyperelastic material, which is if the load is removed, the deformation is fully reversible with no plastic deformation. Therefore, the mussel byssus system was idealised as a hyperelastic material in this research. Future work can focus on simulating and analysing the damage and self-healing of the mussel byssus systems under multiple loading cycles. Additionally, the deformed shapes applied for the partial detachment analysis were 2D. Future work can focus on obtaining more accurate 3D deformed shapes to improve the accuracy of the inverse methods.

In our study, we introduced analytical and FE inverse methods to obtain the mechanical behaviours of the constituents of the mussel byssus system and validated the feasibility of these methods, which provide a new approach to analyse the composite behaviour of the mussel byssus system and any other biocomposite material for future biomaterial mechanism research. Meanwhile, the diversity of mussel byssus system mechanisms also provides many insights for mimetic applications in engineering and mate-

rials design, such as the design of anchor systems using the feature of the mussel byssus system to reduce fatigue in the mooring lines.

4.6 Conclusion

In this research, both analytical and FE inverse methods have been applied for the first time to determine the individual mechanical behaviours of the mussel plaque and the proximal portion. Those inverse methods were critical due to the inherent difficulty in obtaining these properties through conventional tests. The inverse methods utilised experimental force-displacement curves from different constituents of the mussel byssus system and side-deformed shapes of mussel plaques as optimisation metrics.

The findings indicate that these inverse techniques effectively identify the individual mechanical behaviours of the proximal thread and the plaque using reasonably assumed constitutive material models with the sum of square residuals equal to 0.0004 (N^2) and 0.01 (mm^2), respectively. Meanwhile, the results support the accurate representation of the mechanical behaviours of the distal portion with the Ogden model and the proximal and plaque portions with the Neo-Hookean model. Additionally, this study has also conducted a comprehensive characterisation of the microstructure and mechanical behaviours of the three different portions within the mussel byssus system. The distal portion exhibits elevated strength but reduced deformability in contrast to the proximal portion. The variations in the tensile behaviour among these portions could be attributed to differences in their microstructure or chemical composition. Finally, the study has also discussed the application of the FE inverse method for the calculation of the potential plaque bottom surface detachment radius.

The material parameters obtained from the inverse methods offer an opportunity for in-depth analysis of the material behaviour of the mussel byssus system. Future studies could focus on further improving the precision of inverse approaches by assessing the transition mechanisms between different portions and monitoring the dynamic detachment processes of the plaque bottom surface. Additionally, it will be necessary to determine the fracture characteristics of these three portions in the future and simulate the entire fracture tensile process using a comprehensive 3D finite element model of the mussel byssus system.

Chapter 5

Unveiling the deformability of mussel plaque core: the role of pore distribution and hierarchical structure

Publication Information

Title	Unveiling the deformability of mussel plaque core: The role of pore distribution and hierarchical structure
Author	Yulan Lyu, Mengting Tan, Yong Pang, Wei Sun, Shuguang Li, Tao Liu*
Journal	Soft Matter
Status	Published (https://doi.org/10.1039/D4SM00832D)
Year	2024

5.1 Introduction

The mussel byssus system, consisting of protein threads and porous plaques (Figures 5.1a and b), can anchor to almost any surface in harsh marine environments [4, 68, 133, 151]. This 'anchoring' system enables mussels to withstand a force equivalent to approximately 10 times their own weight (Figure 5.1a) [9]. Meanwhile, the high deformability of mussel plaques allows them to undergo significant deformation without fracturing under the strong hydrodynamic forces exerted by the ocean. In nature, mussel plaques undergo directional tensions with pulling angles ranging from 0° to 90°. Our previous study developed a customized microscope system to apply quasi-static tension to mussel plaques and found that they can experience substantial deformation [9], exhibiting up to a 2.8-fold increase in volume when the pulling angle reaches or exceeds 45° (Figure 5.1c).

However, despite thorough studies on the adhesive performance of mussel plaques [1, 6, 40, 44, 152], the cause of their high deformability remains unclear.

Mussel plaques consist of a porous core and a protective cuticle layer (Figure 5.1b) [16, 17, 66, 67]. The cuticle layer is approximately 4 μm thick and is covered by granules about 0.5 μm in size [9]. The plaque features randomly distributed nano- (small-) and micro- (large-) scale pores, with diameters approximately ranging from 50-800 nm to 1-3 μm, respectively (Figure 5.1d, e and f). The obtained pore size ranges are consistent with previous studies [16, 21]. The formation of porous structures is closely related to the seawater temperature and pH levels [16, 21]. The plaque core and cuticle layer work together to enhance deformability and establish a robust load-bearing capacity [6, 9, 153]. The pore structure of significantly deformed plaques has been reported in previous work [66, 154]. However,

the evolution of the pore deformation under external loads, leading to high deformability, remains unclear.

Previous research has suggested that the pore arrangement within the plaque cores might influence the stress heterogeneity and thus have a significant impact on their deformability [134]. However, this study mainly applied ordered pores rather than the natural pore arrangement found in mussel plaques. It is, therefore, crucial to understand the role of the naturally porous structure (Figure 5.1e) on the mechanical behaviours of plaque cores.

This study is motivated by the need to investigate the impact of the plaque core's porous structure on its mechanical performance, with a focus on deformability. We investigated the effects of pore distribution (Figures 5.1d and f) and multi-scale porous structure (Figure 5.1e) on the mechanical properties of plaque cores. The actual pore distribution within plaque cores was determined using scanning electron microscope (SEM) analysis. Scaled distribution parameters were then applied to create two-dimensional (2D) porous representative volume elements (RVEs) for subsequent numerical and experimental investigations of the porous structures. The validated phase field method, incorporating the Neo-Hookean model, was used in the simulations to investigate the effect of pore distribution and multi-scale structure on the failure mechanism of porous RVEs. By fully understanding how the pore distribution and multi-scale porous structure influence the mechanical performance, this study provides valuable insights for designing highly deformable metamaterials inspired by mussel plaques.

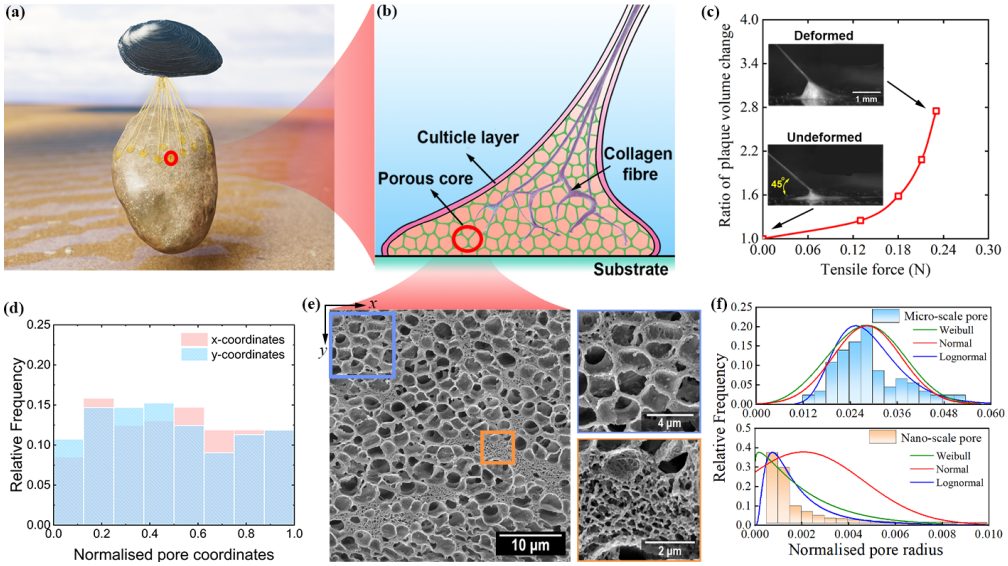


Figure 5.1: (a) Mussel byssus system attached on a rock, (b) schematic diagram of the mussel plaque's microstructure [9], (c) large deformation of mussel plaque under tension, (d) the distribution of normalized x and y coordinates for large pore centres within the mussel plaque core, (e) the SEM photo showing the multi-scale porous structure of mussel plaque core and (f) the distribution of normalized radius for both large-scale (mirco) and small-scale (nano) pores within the mussel plaque core.

5.2 SEM characterisation of mussel plaque core

5.2.1 SEM sample preparation

Blue mussels (Mytilus edulis) were collected from the intertidal zone off the coast of Hunstanton, UK. Subsequently, they were tied to small acrylic plates and kept in a water tank with cold (8°C-10°C), oxygenated, and continuously circulated and filtered artificial seawater. Sea salt (Tropic Marin Pro-Reef Sea Salt, UK) was mixed with fresh water to replicate the salinity and pH levels seen in natural seawater (salinity = 33 ppt and pH = 8). The plaques were separated from the acrylic plates using a razor blade (Accu-Edge® Disposable Microtome Blades S35). The collected plaques were fixed in a solution containing 3.7% formaldehyde and 2.5%

glutaraldehyde for approximately four hours [9, 16]. After that, plaque samples were placed in Milli-Q water at 4°C for three days. The plaques were then sectioned into 20 μm thick slices at a temperature of -20°C using a cryostat (Leica CM1850) and immediately immersed in Milli-Q water to remove the mounting medium [16]. The plaque slices underwent dehydration through sequential concentrations of ethanol and were subjected to two drying cycles of hexamethyldisilane (HDMS) [16]. The dehydrated samples were sputter-coated with a 10 nm thick iridium layer for 120 seconds using a Quorum Q150V Plus and imaged using a JEOL 7100F FEG-SEM with an accelerating voltage set at 5 kV.

5.2.2 The pore distribution analysis for mussel plaque core

Two-dimensional (2D) SEM images have suggested that the pores within the plaque cores are of two different scales, ranging in diameter from 50-800 nm (small-scale pores) to 1-3 μm (large-scale pores) (Figure 5.1e). The pore distribution of large-scale pores within those SEM photos was first examined. A total of nine SEM photographs from various plaques and different locations within the same plaque were analysed to minimize the impact of cut position on the large-scale pore distribution, ensuring that the SEM analysis results were representative (Figures 5.1e, 5.2, D.1 and D.2 in Appendix D.1). The irregular large-scale pores were simplified into circular shapes, as shown by the pore outlines in Figure 5.2. The simplification facilitates a more direct method for obtaining important distribution factors for large-scale pores such as porosity, pore radius, pore number and the coordinates of pore centres, which in turn ensures consistency of analysis. Despite the simplification to circular pores, the main geometric

features of plaque cores were retained, thus ensuring that the pore distribution remained consistent with the original complex structure (Figure D.8) (Details shown in Appendix D.2).

Meanwhile, the radii of large-scale pores and the coordinates of the pore centres were normalised by dividing the length of the squared SEM image edges (l_s) for the distribution analysis. The normalised mean value ($\bar{\mu}_p^*$) and normalised standard deviation value ($\bar{s}_p^*$) of the large-scale pores' radius were calculated as:

$$\bar{\mu}_p^* = \frac{r_{p1} + r_{p2} + \cdots + r_{pm}}{m * l_s} \tag{5.1}$$

$$\bar{s}_p^* = \sqrt{\frac{\sum_{i=1}^{m} \left(\frac{r_{pi}}{l_S} - \bar{\mu}_p^*\right)^2}{m}} \tag{5.2}$$

where r_{pi} is the radius of large-scale pores within the SEM images and m is the number of large-scale pores within the SEM images.

The porosity of large-scale pores within the selected SEM image can be calculated as:

$$\upsilon_l = \frac{\pi r_{p1}^2 + \pi r_{p2}^2 + \cdots + \pi r_{pm}^2}{{l_s}^2} \tag{5.3}$$

It can be observed that the large-scale pore radius consistently follows a lognormal distribution (Figures 5.1e, 5.2, D.1 and D.2). However, the distribution parameters and porosity may be affected by the position of the slices or plaques considered (see Tables 5.1, D.1 and D.2 in Appendix D.1). The range of $\bar{\mu}_p^*$ within the plaques is approximately 0.021-0.043, while the range of $\bar{s}_p^*$ is approximately 0.005-0.014. The porosity of large-scale pores (υ_l) ranges from 23% to 33%. Additionally, the Q-Q plots (quantile-quantile plots) (Figure D.4 in the Appendix D.3) comparing the

x and y coordinates of large-scale pore centres in the nine SEM images (Figures 5.1e, 5.2, D.1 and D.2) show that both the x and y coordinates are consistent with a uniform distribution.

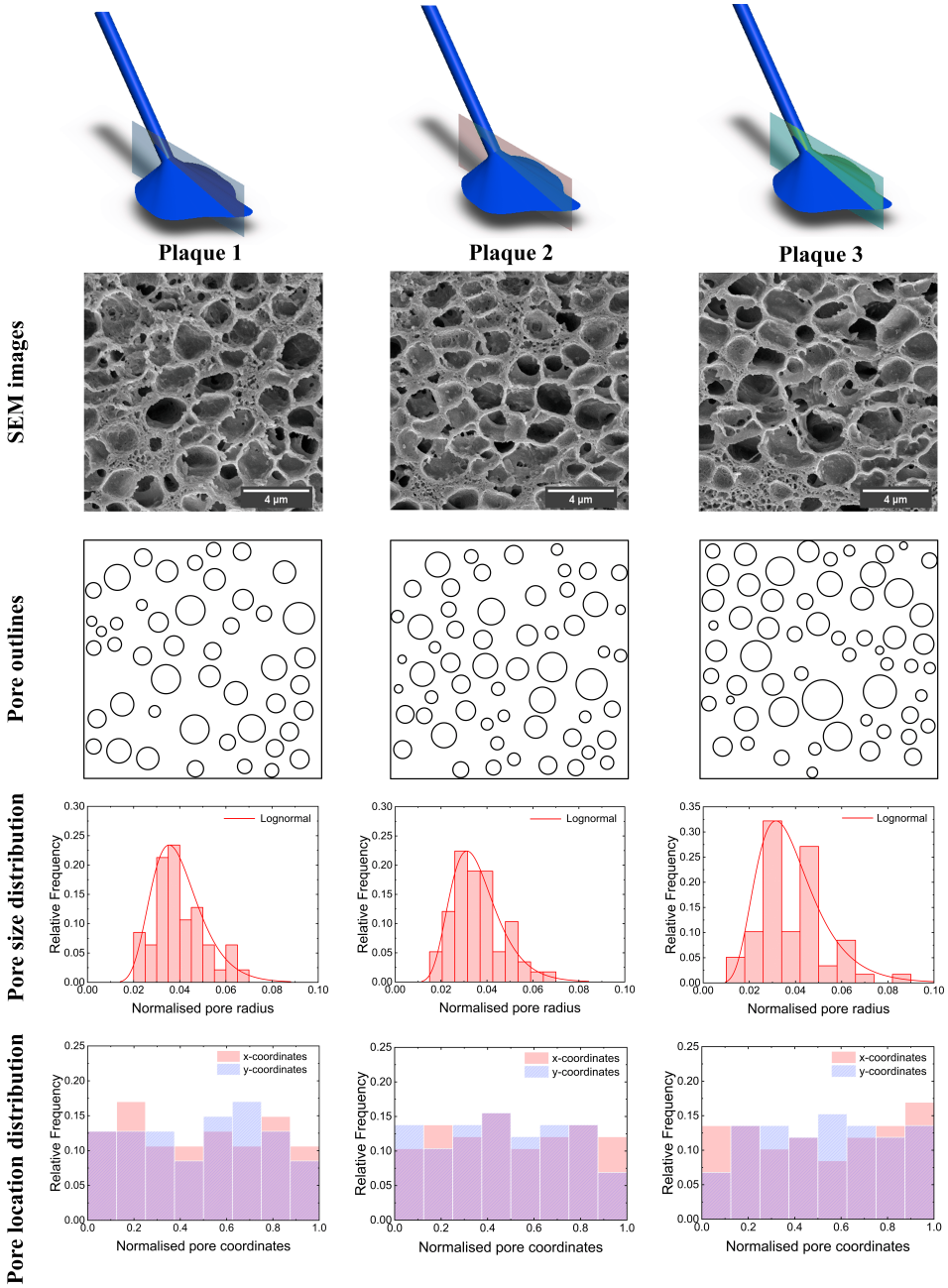


Figure 5.2: Pore size and location distribution analysis for SEM images of different plaques.

Therefore, it can be concluded that the radius of large-scale pores is lognormally distributed, and the coordinates of the large-scale pore centres are

uniformly distributed within the mussel plaque core. Because the distribution parameters and porosity vary for each SEM photo, the parameters of Figure 5.1e were selected and scaled to generate the porous RVEs for further study: υ_l=27%, μ_p^*=1.12 μm and s_p^*=0.34 μm. μ_p^* and s_p^* are the mean and standard deviation values of the lognormal distribution of the large-scale pores within Figure 5.1e, respectively.

Table 5.1: Porosity (υ_l), normalised mean radius ($\bar{\mu}_p^*$) and normalised standard deviation of radius ($\bar{s}_p^*$) of the simplified large-scale pores within the SEM images for different plaques.

	Porosity (υ_l)	$\bar{\mu}_p^*$	$\bar{s}_p^*$
Plaque 1	25%	0.037	0.011
Plaque 2	26%	0.034	0.01
Plaque 3	30%	0.037	0.014

The pore radius distribution of the small-scale pores also follows a lognormal distribution with a mean value of 150 nm and a standard deviation value of 190 nm (Figure 5.1f). The porosity of the small-scale pores (υ_s) in Figure 5.1e was calculated using ImageJ® as 5%. The analysis for the small-scale pore distribution ensured that our main focus remained on the comprehensive study of large-scale pore distributions while still gaining relevant insights into the characteristics of small-scale pores.

5.3 The generation of the porous RVEs

Two types of porous RVEs were generated for the numerical study. The first RVE type investigates the effect of large-scale pores, while the second RVE type examines the impact of the multi-scale architecture of the mussel plaque core.

5.3.1 Generation of single-scale porous RVEs and post-processing procedure

To overcome manufacturing limitations, the plaque pore sizes were scaled up by a factor of 1000, transitioning from microns to millimetres, to enable 3D printing of the test samples. Two-dimensional (2D) square-shaped porous RVEs were generated by using the scaled distribution parameters of the large-scale pores (v_l=27%, μ^*_{ps}=1.12 mm and s^*_{ps}=0.34 mm). The dimensions of the RVEs are 30 x 30 mm, comprising solely large-scale pores with the remaining volume filled with solid material.

The size effect of the porous RVEs was investigated by studying the responses of the porous RVEs with ordered pore arrangement and uniform pore size (details shown in Appendix D.4). The ordered porous RVEs featured porosity that was consistent with that of the large-scale pores obtained in the SEM image (v_l=27%). The pore size within these RVEs was consistent with the scaled mean value of the large-scale pores (μ^*_{ps}=1.12 mm), and the spacing between adjacent pores was the same (Figure D.5 in Appendix D.4). The results obtained from the simulations showed that the RVEs with the 30x30 mm dimension could reflect the macroscopic stress-strain relation of the porous structures (Figures D.6 in Appendix D.4). The macroscopic stress was determined by dividing the reaction force in the tensile direction by the cross-sectional area of the RVE, while the macroscopic strain was calculated by dividing the displacement in the tensile direction by the side length of the RVE.

The commercial FE package ABAQUS was employed to create the single-scale RVEs using Python scripts. Within the Python scripts, the function *random.lognormvariate (μ_p, s_p)* was used to generate pores in the RVEs following a lognormal distribution, where μ_p is the mean value of the normal

distribution corresponding to the lognormal distribution within the SEM image:

$$\mu_p = \ln\left(\frac{\mu_{ps}^{*2}}{\sqrt{\mu_{ps}^{*2} + s_{ps}^{*2}}}\right) = 0.07 \text{ mm} \tag{5.4}$$

s_p is the standard deviation value of the normal distribution corresponding to the lognormal distribution within the SEM image:

$$s_p = \sqrt{\ln\left(\frac{s_{ps}^{*2}}{\mu_{ps}^{*2}} + 1\right)} = 0.3 \text{ mm} \tag{5.5}$$

The coordinates of pore centres follow a uniform distribution in accordance with the coordinate distribution observed in the SEM images (Figures 5.1e, 5.2, D.1, D.2 and D.4). The function *random.uniform (low, high)* was applied in the Python scripts to identify the locations of pores in the RVEs, where 'low' and 'high' are the min value and max value of pore centre coordinates, respectively.

Therefore, in order to ensure all the pores are contained within the RVE, each pore's centre coordinates (x_i, y_i) must adhere to the following relation:

$$(x, y) \in \{(x_i, y_i) \mid r_i \leq x_i \leq w - r_i, r_i \leq y_i \leq w - r_i\}, i \in n \tag{5.6}$$

here, n is the number of pores within the RVE, r_i represents the i th pore radius in the RVE, and w is the side length of the RVE, i.e. w= 30 mm. r_i and $w - r_i$ present 'low' and 'high' in the function *random.uniform(low, high)*, respectively.

Moreover, the distance between the centres of any two pores θ in the RVE

must be greater than the sum of their radii to avoid overlapping:

$$\theta = \sqrt{(x_i - x_j)^2 + (y_i - y_j)^2} > r_i + r_j, i \neq j, i, j \in n \tag{5.7}$$

Consequently, the porous RVEs created through the ABAQUS Python scripts were required to fulfil all the previously mentioned criteria before being subjected to the FE analysis in ABAQUS.

The generated single-scale porous RVEs were discretised using 2D triangular plane stress elements, i.e. CPS3T [155] in ABAQUS notation and analysed using the phase field modelling method via analogy to a coupled heat transfer-displacement analysis [156]. The phase field method is described in more detail in Section 5.4 below.

Following the completion of the ABAQUS calculation, a further Python script was developed with the objective of obtaining the following data from ABAQUS .odb files:

1. The coordinates (x_i, y_i) of all pore centres for each RVE ($i = 1, 2, 3 \ldots n$)
2. The radii r_i of all pores for each RVE
3. The number of pores for each RVE
4. The macroscopic stress-strain curves for each RVE

Furthermore, a MATLAB algorithm was created to extract and calculate various parameters from the stress-strain data sets. These include the strain energy density (φ), strength (σ_{max}), final failure strain (ε_{ff}), and the strain difference ($\Delta\varepsilon$) between the initial failure strain and the final failure strain for each RVE. In particular, the strain energy density (φ) was calculated as the area under the stress-strain curve. The initial failure

strain was defined as the strain value corresponding to the peak strength, and the final failure strain (ε_{ff}) was the strain value corresponding to the point that stress decreased to 0. Additionally, the normalised mean value ($\bar{\mu}$) and normalised standard deviation value ($\bar{s}$) of the pores' radius within each single-scale RVE were calculated as:

$$\bar{\mu} = \frac{r_1 + r_2 + \cdots + r_n}{n * w} \tag{5.8}$$

$$\bar{s} = \sqrt{\frac{\sum_{i=1}^{n} \left(\frac{r_i}{w} - \bar{\mu}\right)^2}{n}} \tag{5.9}$$

5.3.2 Generation of multi-scale porous RVEs and post-processing procedure

To further investigate the influence of multi-scale porous structures on mussel plaque behaviour, three different single-scale RVE FE models were selected. The multi-scale porous structures were 3D in nature, and the cell walls were 2D surfaces. As an approximation, a 2D idealisation was made for the 3D porous structures. The multi-scale porous structures were generated by removing 2D elements in the FE models and reconnecting the nodes using lines. In the simulation, the walls of the pores were represented by these lines. The approximation can be justified as follows. It is a simple way as a first step into the study. On the other hand, it should be capable of offering some qualitative assessment of the behaviour of such structures. As a result of such idealisation, 2D wall surfaces were reduced to 1D elements, which were subsequently simulated using 1D elements in the finite element (FE) models, connecting the nodes to form 2D porous structures. Additionally, for cellular solids made of rubber-like materials, the

type of unit cell primarily determines whether stretch- or bending-governed behaviours during the elastic deformation stage. However, rubber-like materials are highly stretchable, with a failure strain of approximately 1.2 (Figure 5.5). Under large deformations, they ultimately exhibit stretch-governed behaviour regardless of the unit cell type [157, 158]. In this scenario, each truss or the walls of the small pores mainly experience axial tension, similar to the behaviour of truss elements in finite element (FE) simulations. Therefore, truss elements (T2D2T elements [155]) are a good approximation in FE simulations, as they effectively capture the stretch deformations of the walls.

The radius of the truss elements was determined to ensure that the newly generated multi-scale porous RVEs reflected the same overall porosity ($\upsilon = \upsilon_s + \upsilon_l = 32\%$) with the SEM image (Figure 5.1e). The approximate size of the small-scale pores within the multi-scale porous RVEs was set to 0.5 mm, which falls within the scaled range of small-scale pore sizes observed in mussel plaques (0.05 mm-0.8 mm). A size effect study, detailed in the Appendix D.5, confirmed that the size of the small-scale pores within the multi-scale porous RVEs has an insignificant impact on the macroscopic material behaviours (Figure D.7 in the Appendix D.5). Notably, the structural configuration adopted in the multi-scale porous RVEs serves as an approximation for examining the multi-scale porous structure of the mussel plaque. This simplified model was utilised to explore characteristic behaviours of such structures rather than a precise duplication of the plaque's hierarchical structures.

Building on the same material properties and periodic conditions [159, 160] used in the single-scale RVE FE models, the phase field method was applied to analyse the failure behaviour of the multi-scale RVEs (Section 5.4). The stress-strain curves of multi-scale RVEs were extracted from the ABAQUS

.odb files, and fracture paths were analysed using the Abaqus/CAE graphical user interface.

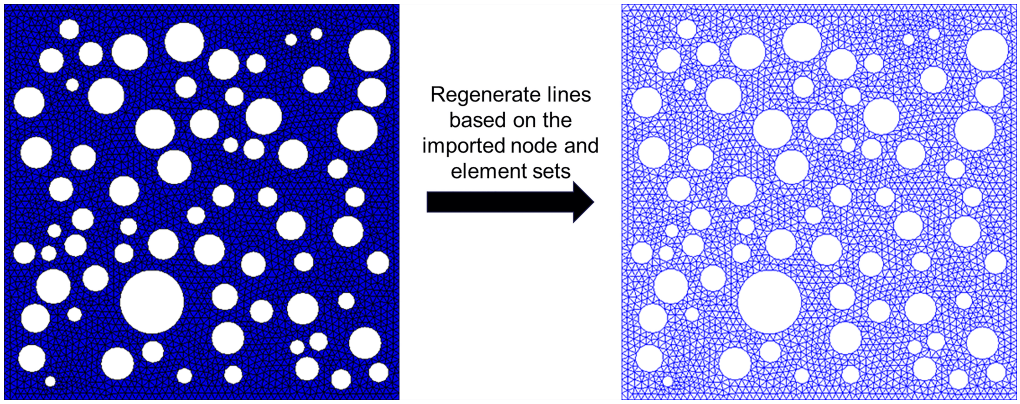


Figure 5.3: Schematic drawing of multi-scale porous RVEs generation (The mesh element type switched from 2D triangular plane stress elements CPS3T to coupled temperature-displacement truss element T2D2T).

5.4 ABAQUS implementation and experimental calibration of the phase field modelling method

5.4.1 Theory of phase field method for fracture modelling

The phase field method was applied to analyse the failure mechanism of test samples and RVEs. The parent material was assumed to be an incompressible Neo-Hookean material. Therefore, in this section, a phase-field method for the incompressible Neo-Hookean material is introduced.

According to the theory of energy conservation, when a crack grows in an arbitrary body Ω, the energy per time unit $\dot{E}$ provided externally is equal to the rate of the strain energy $\dot{U}$ stored in the material and the rate of the

energy $\dot{D}^{diss}$ dissipated from the crack:

$$\dot{E} = \dot{U} + \dot{D}^{\text{diss}} \tag{5.10}$$

Let c denote the phase field variable. The value of c is between 0 and 1, with $c = 0$ and $c = 1$ denoting undamaged materials and fully damaged materials, respectively. The quadratic degradation function $g(c)$ is introduced to control the material stiffness, i.e.,

$$g(c) = (1 - c)^2 \tag{5.11}$$

Therefore, the strain energy stored in the material can be written as the following:

$$U = \int_{\Omega} g(c)\varphi dV \tag{5.12}$$

where φ is the strain energy density.

For incompressible 2D plane stress studies in this research, the strain energy density φ can be expressed as [161]:

$$\varphi = \varphi_{iso}(\boldsymbol{F}) \tag{5.13}$$

where $\boldsymbol{F}$ is deformation gradient tensor, $\varphi_{iso}(\boldsymbol{F})$ is the isochoric strain energy density.

Therefore, based on the vector calculus identity [162] and divergence theorem [163], the rate of the stored strain energy is given by:

$$\dot{U} = \int_{\Omega} \left(\frac{\partial g(c)}{\partial c} \varphi \dot{c} \right) dV + \int_{\partial\Omega} g(c) \frac{\partial \varphi}{\partial \boldsymbol{F}} \cdot \dot{\mathbf{u}} \cdot \mathbf{n} dA - \int_{\Omega} \left(\nabla \cdot \left(g(c) \frac{\partial \varphi}{\partial \boldsymbol{F}} \right) \right) \cdot \dot{\mathbf{u}} dV \tag{5.14}$$

where $\dot{c}$ is the rate of the damage variable, $\dot{\boldsymbol{u}}$ is the velocity field presenting the rate of change of the displacement field $\mathbf{u}$ with respect to time, $\partial\Omega$ is the surface of the volumetric body Ω and $\mathbf{n}$ is the outward normal to the surface $\partial\Omega$. The derivation process for Eq. 5.14 is shown in the Appendix D.6.

Meanwhile, the dissipated crack formation energy density τ was given by Miehe et al. (2010) [164]:

$$\tau = G_c \gamma_l(c, \nabla c) = G_c \left(\frac{c^2}{2l} + \frac{l}{2}(\nabla c \cdot \nabla c) \right) \tag{5.15}$$

where G_c is the critical energy release rate and $\gamma_l(c, \nabla c)$ is the crack density function with length scale parameter l , phase field variable c and the spatial gradient ∇c [164].

Therefore, the energy dissipated by the crack formation D^f and the rate of the dissipated energy from crack formation $\dot{D}^f$ can be written as:

$$D^f = \int_\Omega \tau dV = \int_\Omega G_c \left(\frac{c^2}{2l} + \frac{l}{2}(\nabla c \cdot \nabla c) \right) dV \tag{5.16}$$

$$\dot{D}^f = \int_\Omega G_c \left(\frac{c\dot{c}}{l} + l(\nabla c \cdot \nabla \dot{c}) \right) dV \tag{5.17}$$

Again, based on the vector calculus identity [162] and divergence theorem [163], Eq. 5.17 can be rewritten as:

$$\dot{D}^f = \int_\Omega G_c \dot{c} \left(\frac{c}{l} - l\nabla^2 c \right) dV + \int_{\partial\Omega} G_c l \nabla c \dot{c} \cdot \mathbf{n} dA \tag{5.18}$$

The derivation process for Eq. 5.18 is in the Appendix D.7.

Moreover, a rate of dissipation energy for crack growth $\dot{D}^g$ was introduced

by Pascal et al. (2019) [161]:

$$\dot{D}^g = \int_\Omega \kappa_1 \dot{c}^2 dV \tag{5.19}$$

where scalar κ_1 denotes a viscosity parameter. Thus, the rate of the dissipated energy through the crack can be presented as:

$$\dot{D}^{\text{diss}} = \dot{D}^f + \dot{D}^g = \int_\Omega G_c \dot{c} \left(\frac{c}{l} - l\nabla^2 c \right) dV + \int_{\partial\Omega} G_c l \nabla c \dot{c} \cdot \mathbf{n} dA + \int_\Omega \kappa_1 \dot{c}^2 dV \tag{5.20}$$

Additionally, the external energy can be broadly classified into work done by surface tractions (forces acting on the boundary of the body) and body forces (forces acting throughout the volume of the body). Hence, the rate of external energy $\dot{E}$ can be expressed as:

$$\dot{E} = \int_\Omega \boldsymbol{b} \cdot \dot{\mathbf{u}} dV + \int_{\partial\Omega} \boldsymbol{t} \cdot \dot{\mathbf{u}} dA \tag{5.21}$$

where $\boldsymbol{b}$ presents the volumetric body force vector and $\boldsymbol{t}$ is the surface traction force vector.

Therefore, based on Eqs. 5.10, 5.14, 5.20 and 5.21, it can be obtained as follows:

$$\begin{aligned} \int_\Omega \boldsymbol{b} \cdot \dot{\mathbf{u}} dV + \int_{\partial\Omega} \boldsymbol{t} \cdot \dot{\mathbf{u}} dA = & \int_\Omega \dot{c} \left(\frac{\partial g(c)}{\partial c} \varphi + \frac{G_c c}{l} - G_c l \nabla^2 c + \kappa_1 \dot{c} \right) dV \\ & - \int_\Omega \left(\nabla \cdot \left(g(c) \frac{\partial \varphi}{\partial \boldsymbol{F}} \right) \right) \cdot \dot{\mathbf{u}} dV \\ & + \int_{\partial\Omega} g(c) \frac{\partial \varphi}{\partial \boldsymbol{F}} \cdot \dot{\mathbf{u}} \cdot \mathbf{n} dA + \int_{\partial\Omega} G_c l \nabla c \dot{c} \cdot \mathbf{n} dA \end{aligned} \tag{5.22}$$

Given the macroforce and microforce balances, we can finally obtain the following equations:

$$\nabla \cdot \left(g(c) \frac{\partial \varphi}{\partial F} \right) + \boldsymbol{b} = 0 \tag{5.23}$$

$$\frac{\partial g(c)}{\partial c}\varphi + \frac{G_c c}{l} - G_c l \nabla^2 c + \kappa_1 \dot{c} = 0 \tag{5.24}$$

with the following Neumann boundary conditions that may be applied

$$g(c)\frac{\partial \varphi}{\partial F} \cdot \mathbf{n} = \mathbf{t} \text{ and } G_c l \nabla c \cdot \mathbf{n} = \mathbf{0} \tag{5.25}$$

Based on Eq. 5.24, if $\kappa_1 = 0$, the phase-field response is rate-independent. Alternatively, the response is rate-dependent.

5.4.2 Finite element (FE) analysis implementation

Heat transfer analogy

The strain energy density for the incompressible Neo-Hookean material specifically is shown below:

$$\varphi = C_1 \left(I_1 - 3\right) \tag{5.26}$$

where C_1 is a material constant and I_1 is the first invariant.

Combing Eqs. 5.11, 5.24 and 5.26,

$$\frac{\kappa_1}{G_c l}\dot{c} - \nabla^2 c = \frac{2(1-c)\cdot\left[C_1\left(I_1 - 3\right)\right]}{G_c l} - \frac{c}{l^2} \tag{5.27}$$

The time derivative term of phase field variable $\dot{c}$ can be expressed as:

$$\dot{c} = \frac{dc}{dt} = \frac{\partial c}{\partial t} + \frac{\partial c}{\partial x}\mathrm{v}_x + \frac{\partial c}{\partial y}\mathrm{v}_y + \frac{\partial c}{\partial z}\mathrm{v}_z \tag{5.28}$$

where x, y, z are the spatial coordinates; and $\mathrm{v}_x, \mathrm{v}_y, \mathrm{v}_z$ are the corresponding velocity components.

Because the focus of our research is the progressive and slow fracture of 2D porous structures, it was assumed $v_x \approx v_y \approx v_z \approx 0$. Therefore, Eq. 5.28 can be simplified as:

$$\dot{c} = \frac{dc}{dt} \approx \frac{\partial c}{\partial t} \tag{5.29}$$

Furthermore, Eq. 5.27 can be rewritten as:

$$\frac{\kappa_1}{G_c l}\frac{\partial c}{\partial t} - \nabla^2 c = \frac{2(1-c)\cdot[C_1(I_1-3)]}{G_c l} - \frac{c}{l^2} \tag{5.30}$$

Meanwhile, the field equation of heat transfer given by the first law of thermodynamics reads as,

$$\rho c_p \frac{\partial T}{\partial t} - k\nabla^2 T = q \tag{5.31}$$

where T is the temperature field, $\frac{\partial T}{\partial t}$ is the rate of the temperature field, k is the thermal conductivity, c_p is the specific heat, ρ is the density, and q is the heat source.

Given the similarity of Eqs. 5.30 and 5.31, the phase field model can be implemented via the heat transfer analogy by letting the temperature variable T represent the phase field variable c. Assuming $k = 1$, the equation for the heat source q can be expressed as:

$$q = \rho c_p \frac{\partial T}{\partial t} - \nabla^2 T \equiv \eta \frac{\partial c}{\partial t} - \nabla^2 c = \frac{2(1-c)\cdot[C_1(I_1-3)]}{G_c l} - \frac{c}{l^2} \tag{5.32}$$

where ρc_p is analogised as the fracture parameter η, $\eta = \frac{\kappa_1}{G_c l}$.

ABAQUS implementation

The phase field method was numerically implemented in ABAQUS using combined User subroutines UHYPER and HETVAL. The strain energy density φ of the Neo-Hookean material model was degraded in UHYPER using Eq. 5.11. A local history variable field H introduced by Miehe et al. (2010) [164] was applied to store the value of the strain energy density within the UHYPER and transfer it to the HETVAL subroutine to achieve the temperature analogy. The history variable field H could prevent reversible damage and ensure that the damage variable continues to grow until completely damaged [164]:

$$H = \max_{\beta \in [0,t]} \left(\varphi_{t=\beta} \right) \tag{5.33}$$

Meanwhile, the heat flux (q) and the changing rate of the heat flux (χ) were defined in the HETVAL subroutine as follows:

$$q = \frac{2(1-c)}{G_c l} H - \frac{c}{l^2} \tag{5.34}$$

$$\chi = \frac{\partial q}{\partial T} \equiv \frac{\partial q}{\partial c} = -\left(\frac{1}{l^2} + \frac{2H}{G_c l} \right) \tag{5.35}$$

The coupled temp-displacement solver within the ABAQUS package was used for the FE calculations. The 'steady-state' solver option was employed for rate-independent phase-field analysis (i.e., $\kappa_1 = 0$), while the 'transient' response was used for the rate-dependent phase field model. It is also necessary to define the thermal conductivity (k), density (ρ), and specific heat (c_p) within the material properties for the rate-dependent model, while only the thermal conductivity (k) needs to be defined for the rate-independent model. The material constant C_1, the critical energy release rate G_c and the

length scale l needed to be defined for both models within the Hyperelastic 'User-defined' section. Additionally, the 'Depvar' and 'Heat Generation' options were active to achieve element deletion and the temperature field analogy, respectively. The temperature field was created inside the FE model with magnitude = 0, and the results of the nodal solution temperature (NT11) were plotted to visualise the phase field solution (Element with $NT11 \geq 1$ was deleted).

5.4.3 Material parameters acquisition and model calibration

Single-edge notched tension (SENT) tests

Obtaining precise material properties of mussel plaque soft cores is challenging due to current limitations in technical and experimental methodologies. As the focus of this paper is to understand the effect of the microstructure rather than the material properties of the parent material, TangoBlack Plus FLX980, a soft and highly deformable 3D printing material, was employed to reproduce the scaled microstructure in both numerical and experimental studies. The samples were printed using the Stratasys Objet 260 Connex 3 3D printer, which uses light-based printing techniques, specifically photopolymerisation [165].

Single-edge notched tension (SENT) tests [166] with different notch lengths were carried out to obtain the material parameters of TangoBlack Plus FLX980, including the material constant C_1, critical energy release rate G_c, and length scale l. Rectangular strips used in the SENT tests had a total length of 100 mm (clamp distance 80 mm), a width of 25 mm, a thickness of 1 mm, a notch width of 0.3 mm, and variable notch lengths (α)

ranging from 0 mm to 4 mm (Figure 5.4a) [166, 167]. The sample size was designed based on the rubber fracture experiments conducted by Rivlin and Thomas (1953) [167] and Roucou et al. (2019) [166]. Samples were 3D printed using TangoBlack Plus FLX980. SENT tests were displacement-controlled with a fixed strain rate of 100% strain/min using an INSTRON tensile machine. Since the primary focus of this study does not involve the parent material, the effect of the global strain rate on the parent material was not discussed. Instead, we ensured that the global strain rate was consistent for both SENT tests and following porous sample tensile tests to exclude the effects from the parent material. A Thorlabs DCC1545M CMOS camera, equipped with an imaging lens (focal length of 100 mm), was employed to monitor specimen deformation [168–170]. The CMOS camera was configured at a frame rate of 10 fps and a special resolution of 9.6 pixels/mm.

C_1 and G_c were determined by analysing the nominal stress-strain curves obtained from SENT tests. C_1 was derived by fitting the tensile stress-strain curves prior to failure, and the critical strain energy release rate G_c was computed using the equation below [166, 167]:

$$\begin{aligned} G(\alpha, \lambda) &= 2\alpha K(\lambda) W(\lambda) \\ G_c &= G\left(\lambda_c\right) \end{aligned} \tag{5.36}$$

where G is the strain energy rate, α is the initial notch length, $W(\lambda)$ is the material strain energy density under uniaxial tension, λ_c is the critical stretch value obtained when the applied load abruptly drops to zero in the SENT test, and $K(\lambda)$ is a function of the stretch value λ that can be defined as [166]:

$$K \simeq \frac{3}{\sqrt{\lambda}} \tag{5.37}$$

SENT tests with notch sizes of 2 mm, 3 mm, and 4 mm were simulated to calibrate with experimental results and to obtain the value of the length scale (l). The simulation was carried out using the rate-independent phase field method outlined in Section 5.4, selected specifically for its suitability in modelling the slow fracture process ($\kappa_1 \approx 0$).

Porous samples tensile tests

To further validate the phase field method, three porous samples were 3D printed for uniaxial tensile testing. The porous sample design was based on the size of RVEs and used the scaled distribution parameters for large pores (Figure 5.4b). The uniaxial tensile tests were conducted at a fixed strain rate of 100% strain/min, consistent with the conditions of the SENT experiments. Even though the global strain rate was the same, the local fracture of the porous structure was a dynamic and fast process. Therefore, the phase field rate-dependent model was employed for the simulation. The experimental and simulated tensile stress-strain curves and crack paths for each sample were compared to calibrate the fracture parameter η. Other material parameters, including the material constant (C_1), critical energy release rate (G_c) and length scale (l) were consistent with those calculated in Section 5.4.3.

Calibration results for the phase field modelling methods

The numerical and experimental stress-strain curves corresponding to the SENT tests are shown in Figure 5.5. It can be observed that the experimental curves exhibited a high degree of similarity before the samples failed. This allows for the determination of the material constant C_1, which was found to be 0.09 MPa based on the experimental data prior to failure. Ad-

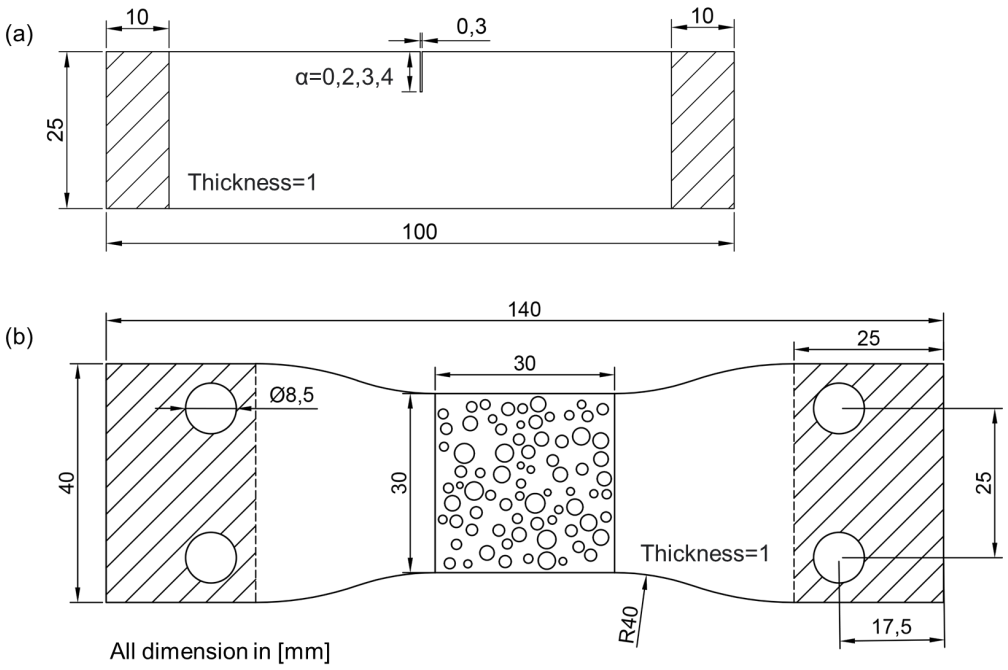


Figure 5.4: Schematic drawings of (a) the SENT test samples and (b) the porous samples for tensile testing.

ditionally, the critical strain energy release rate G_c was calculated to be 0.27 N/mm using Eqs. 5.36 and 5.37. Subsequently, the values of C_1 and G_c were employed in the FE simulations to calibrate the length scale l in the phase field method. The results showed that when $l = 1$ mm, the experimental and simulated results agreed well for all different notch length tests (Figure 5.5).

In addition, three porous samples with the same scaled distribution parameters and porosity (Figure 5.6) were 3D printed to validate the rate-dependent phase field model and to calibrate the fracture parameter η. The results showed that when $\eta = 0.4$, both the stress-strain curves and the failure paths of the simulated and experimental results were in good agreement for all three porous structures (Figure 5.6). Therefore, the material parameters for TangoBlack Plus FLX980 used in the phase field method are summarised in Table 5.2.

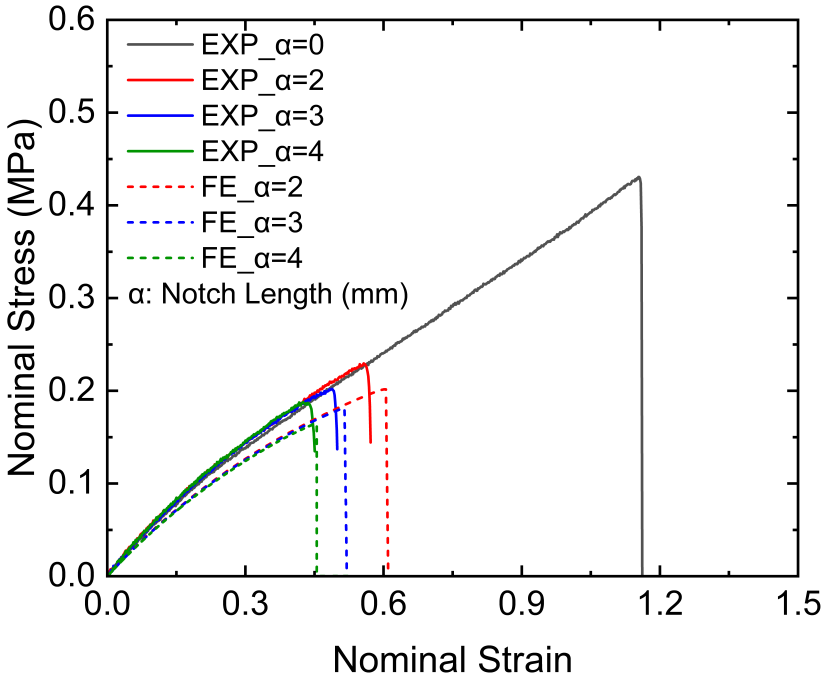


Figure 5.5: Comparison between the numerical and experimental stress-strain curves for samples with different notch lengths during SENT tests.

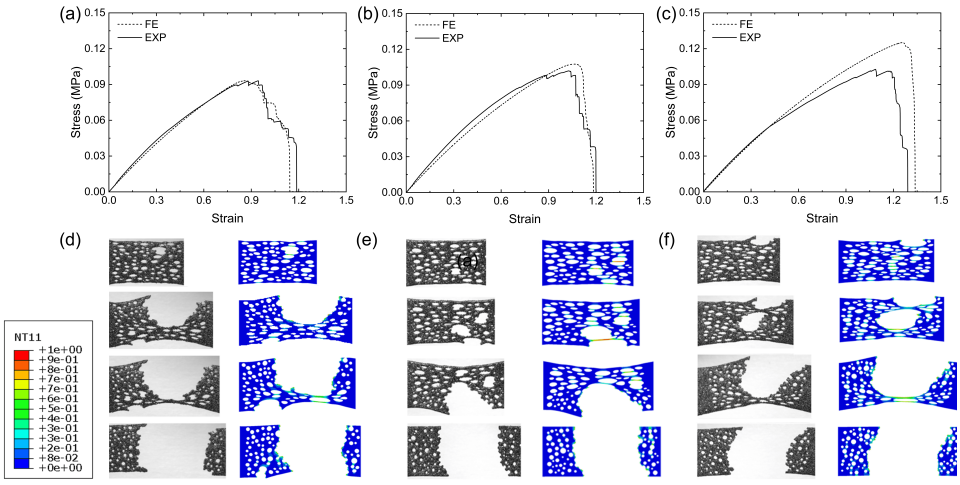


Figure 5.6: Comparison between the (a-c) numerical and experimental stress-strain curves and (d-f) fracture paths for three porous samples in tension (elements with $NT11 \geq 1$ were deleted).

Table 5.2: Material parameters for TangoBlack Plus FLX980.

Material parameters	values
k	1
$C_1(MPa)$	0.09
$G_c(N/mm)$	0.27
$l(mm)$	1
η	0.4

5.5 The failure mechanism analysis of generated RVEs

5.5.1 The effect of large-scale pore distribution on mechanical behaviour

The normalised mean ($\bar{\mu}$) and standard deviation ($\bar{s}$) of the pore radius reflect the statistic characteristic of the pore distribution within the single-scale porous RVEs, raising the question of whether these two parameters have a dominant effect on mechanical behaviour. To address this, Figure 5.7 presents the simulation results for 400 generated RVEs, showing the difference between the initial and final failure strain ($\Delta\varepsilon$), final failure strain (ε_{ff}), strength (σ_{max}), and strain energy density (φ) as functions of the normalised mean ($\bar{\mu}$) and standard deviation ($\bar{s}$). The range of $\bar{\mu}$ (0.025-0.038) and $\bar{\mu}$ (0.007-0.015) of the RVE results shown in Figure 5.7 closely mirrors the range of $\bar{\mu}_p^*$ and $\bar{\mu}_p^*$ observed in the SEM images (Figures 5.1e, 5.2, D.1 and D.2), indicating that the RVE results could reflect the geometrical effect of the microstructures on the mussel plaques.

3D linear regression analysis was used as an estimation method to evaluate the trend of data as functions of $\bar{\mu}$ and $\bar{s}$ (Figure 5.7) [171]:

$$\hat{o} = a_0 + a_1\bar{\mu} + a_2\bar{s} \tag{5.38}$$

where $\hat{o}$ represents the predicted value from the linear regression, and a_0, a_1, a_2 are the regression coefficients.

The Coefficient of Determination R^2 was calculated to measure how well the regression model predicts the real data points (Figure 5.7) [172]:

$$R^2 = 1 - \frac{\sum_{i=1}^{\xi} (o_i - \hat{o}_i)^2}{\sum_{i=1}^{\xi} (o_i - \bar{o})^2} \tag{5.39}$$

where o_i is the i th observed value (i.e., $\Delta\varepsilon$, ε_{ff}, σ_{max}, and φ), $\hat{o}_i$ is the predicted value, $\bar{o}$ is the mean of observed values and ξ is the number of data points (i.e., ξ=400).

R^2 ranges from 0 to 1, where 1 indicates perfect fit, and 0 indicates that the regression model cannot account for any of the variation in the response data around its mean [173]. The nonlinear regression analysis was also conducted to fit the data. However, there was little improvement in the value of R^2. For simplicity, only the results of the linear regression analysis are presented in Figure 5.7.

The results of the linear regression, as shown in Figure 5.7, demonstrate that the overall effects of the normalised standard deviation ($\bar{s}$) on $\Delta\varepsilon$, ε_{ff}, σ_{max}, and φ were statistically insignificant for the 400 samples. Conversely, the regression analysis indicates that an increase in the normalised mean radius ($\bar{\mu}$) led to an overall decreasing trend in strength (σ_{max}), strain energy density (φ), and final failure strain (ε_{ff}), respectively (Figures 5.8b, c and d). While a different overall trend was observed for $\Delta\varepsilon$: as $\bar{\mu}$ increased, the value of $\Delta\varepsilon$ exhibited a slight increase (Figure 5.8a).

It is important to note that linear regression analysis only illustrates the overall trend of the effect of the normalised mean ($\bar{\mu}$) and standard deviation ($\bar{s}$) on macroscopic material properties and cannot capture the high

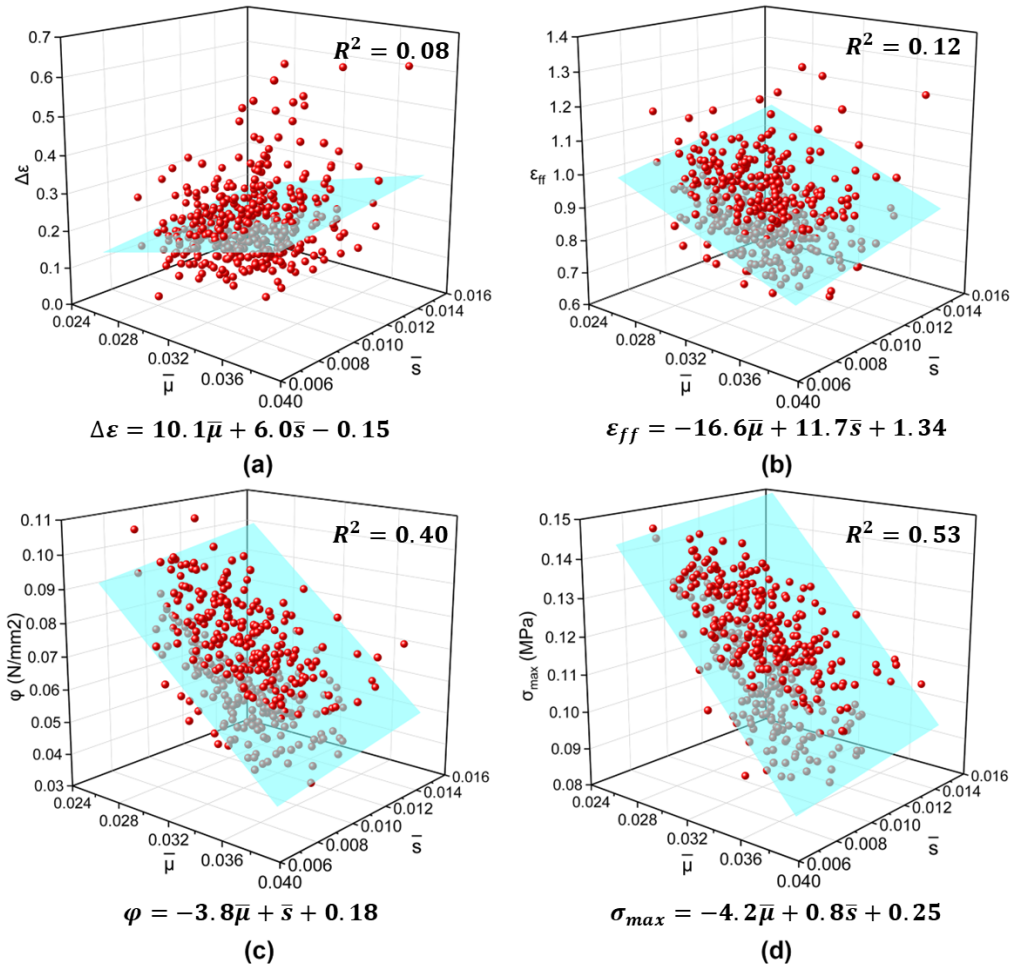


Figure 5.7: The RVE simulation and 3D linear regression results between the normalised mean value standard $\bar{\mu}$, normalised deviation value $\bar{s}$ of the large-scale pore radius and (a) $\Delta\varepsilon$ with a coefficient of determination (R^2) value of 0.08, (b) final failure strain (ε_{ff}) with a R^2 value of 0.12, (c) strength (σ_{max}) with a R^2 value of 0.4, and (d) strain energy density (φ) with a R^2 value of 0.53. The blue planes represent the linear regression surfaces, and the red dots represent the RVE results.

dispersion of the results (Figures 5.7 and 5.8). It can be seen from Figure 5.8 that the same $\bar{\mu}$ can always return scattered $\Delta\varepsilon$, ε_{ff}, σ_{max}, or φ values. This may suggest that while the normalised mean value ($\bar{\mu}$) of the pore radius can influence the final failure strain or other macroscopic material properties of the single-scale RVE, it might not be the sole determining factor. Other factors, such as the interactions between pores or the multi-scale structure, could also play an important role.

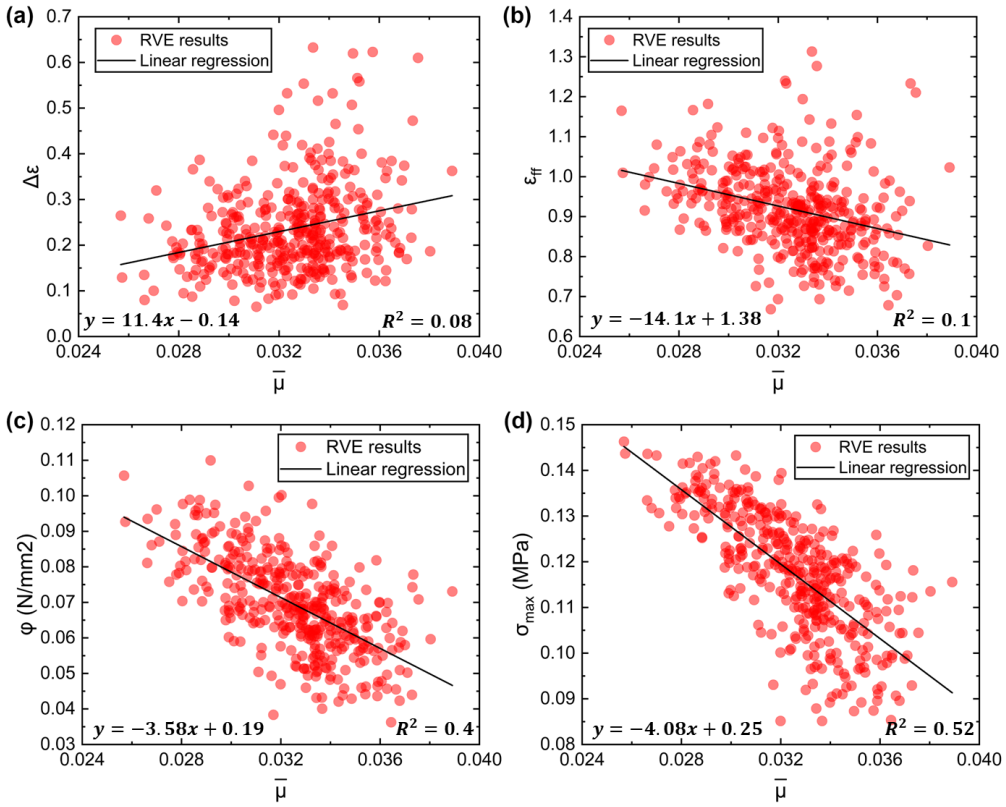


Figure 5.8: The 2D linear regression analysis between the normalised mean value standard $\bar{\mu}$ of the large-scale pore radius and (a) $\Delta\varepsilon$, (b) final failure strain (ε_{ff}), (c) strength (σ_{max}), and (d) strain energy density (φ).

5.5.2 Sudden and progressive failure modes within the single-scale porous RVEs

To better understand the failure mechanism of the single-scale porous RVEs, Figure 5.9 shows the macroscopic stress-strain curve and crack propagation of Sample A, which had the highest values of $\Delta\varepsilon$, ε_{ff}, and φ among the 400 RVE results. For comparison, the stress-strain curves and crack propagation of two additional samples, B and C, are also presented in Figure 5.9. It is noted that samples A, B and C have nearly identical normalised standard deviation ($\bar{s}$) and mean ($\bar{\mu}$) values, with a difference of only ± 0.001.

Two different failure modes were identified from the stress-strain curves of

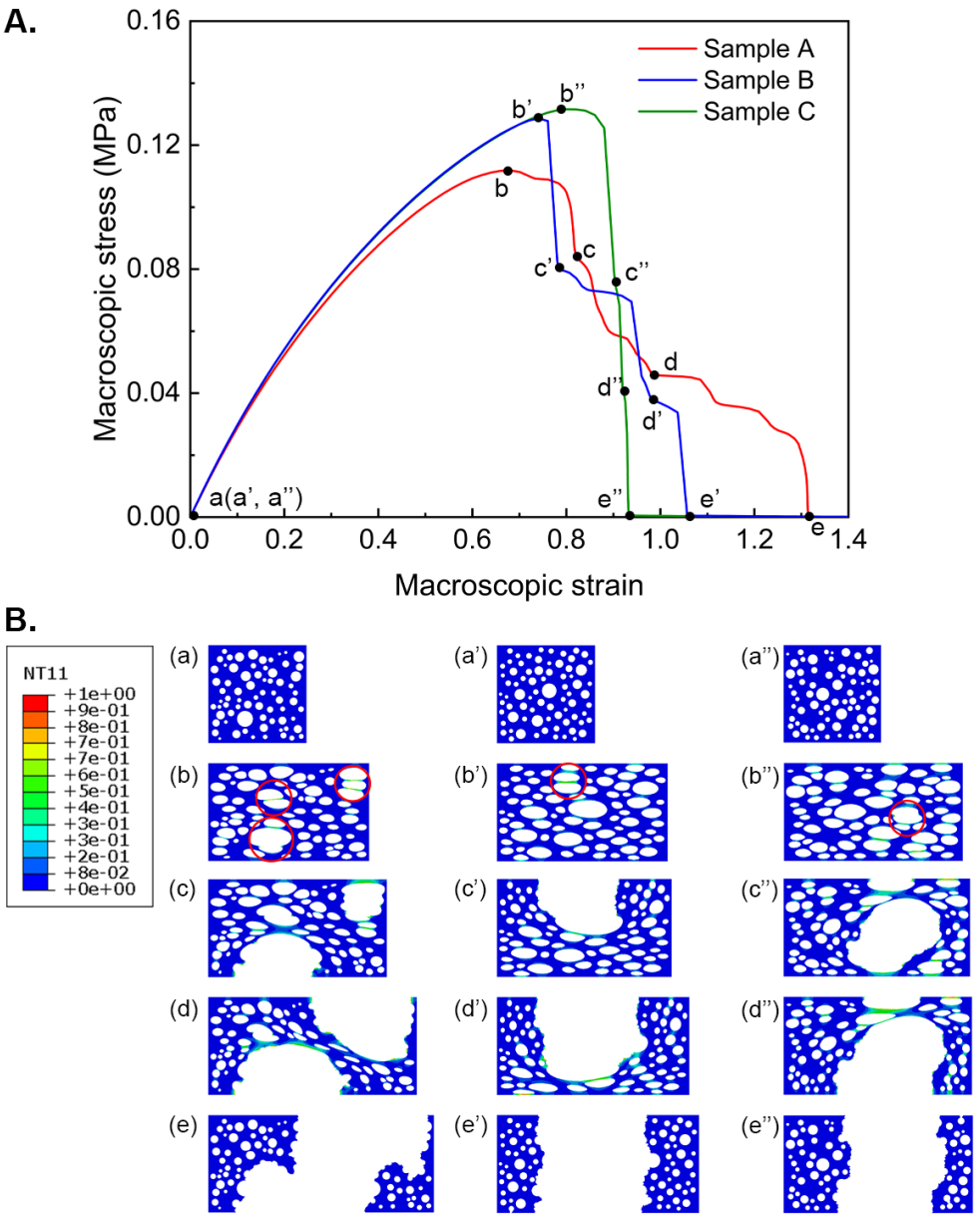


Figure 5.9: (A) The macroscopic stress-strain curves, and (B) crack paths of selected samples with different failure modes.

the samples: progressive failure and sudden failure (Figure 5.9A). For the progressive failure sample (Sample A), the $\Delta\varepsilon$ value was approximately 50% of the final failure strain. In contrast, the $\Delta\varepsilon$ value for the sudden failure sample (Sample C) was close to 0 (Figure 5.9A). The final failure strain of the progressive failure sample (Sample A) was about 1.5 times that of the sudden failure sample (Sample C), but its strength was only approximately 85% of Sample C's strength (Figure 5.9A). Interestingly, the strength of

these samples decreased with increasing $\Delta\varepsilon$ (Figure 5.9A), indicating that the high deformability of the plaques may have been achieved by sacrificing strength.

The crack propagation of Samples A, B and C are presented in Figure 5.9B to further investigate their failure mechanisms. It can be seen from Figure 5.9B that although the normalised standard deviation ($\bar{s}$) and mean ($\bar{\mu}$) of Samples A, B and C are nearly identical, their underlying failure mechanisms are distinct. The damage observed in Sample A initiated at three distinct locations: large pores or closely spaced pores aligned perpendicular to the tensile direction (Figure 5.9B). The scattered locations of the initial damage caused a diffused crack pattern with elongated fracture path, resulting in the progressive failure mode of Sample A. In Sample C, the initial damage occurred at closely clustered pores perpendicular to the tensile direction (Figure 5.9B), rapidly forming a complete fracture path, i.e. concentrated crack pattern. Although another damage was also observed during the failure process, it played a minor role as the initial damage was the primary cause of the failure (Figure 5.9B).

Sample B exhibited a fracture path similar to Sample C (Figure 5.9B). However, unlike the rapidly developing failure observed in Sample C, the failure in Sample B was more progressive (Figure 5.9A). It might be because the blunted cracking observed in Sample B enabled the stress to be distributed and absorbed more energy. While the pore distribution in Sample C may cause the blunted cracking to be insufficient to prevent the rapid crack growth and stress concentration. In addition to the distribution of large-scale pores, the interactions among pores might also influence the failure mechanisms of the RVEs.

5.5.3 The effect of multi-scale porous structures on mechanical behaviour

The SEM images of the mussel plaque core revealed the presence of two different scales of pores (Figure 5.1e). In addition to the large-scale pores that were analysed above, small-scale pores were found to fill the remaining areas of mussel plaques. New multi-scale RVEs based on the three samples selected in Section 5.5.2 were regenerated and analysed to understand the effect of the multi-scale porous structure on the failure mechanism (Figure 5.10).

A comparison of the fracture paths shown in Figures 5.9B and 5.10B reveals that the failure modes were almost identical for all three samples, despite the structural change from the single-scale porous RVE to the multi-scale porous RVE. This suggests that the failure mechanism could be dominated by the large-scale pores.

The stress-strain curves for both multi-scale and single-scale porous RVEs are presented in Figure 5.10A. The multi-scale porous RVEs with 32% porosity exhibited significantly lower stiffness compared to the single-scale porous RVEs with 27% porosity, despite having only a 5% difference in porosity (Figure 5.10A). To understand this mechanism, numerical simulations of solid RVE and small-scale porous RVE with 5% porosity were conducted. These simulations demonstrate that even a small increase in porosity can lead to a substantial decrease in material stiffness due to microstructural changes (details shown in the Appendix D.8). The reduction in stiffness, however, enhanced the final failure strain of the multi-scale porous RVEs (Figure 5.10A). Specifically, the final failure strains of the three multi-scale porous samples increased by 40% (Sample A'), 50% (Sample B'), and 60% (Sample C'), respectively, compared to the single-scale

samples (Figure 5.10A). Meanwhile, the strength of the three multi-scale porous samples decreased by 33% (Sample A'), 31% (Sample B'), and 32% (Sample C'), respectively, due to the reduction in stiffness. This may suggest that the multi-scale porous structure of mussel plaques might improve the deformability by reducing their stiffness, but this could also result in a reduction in strength.

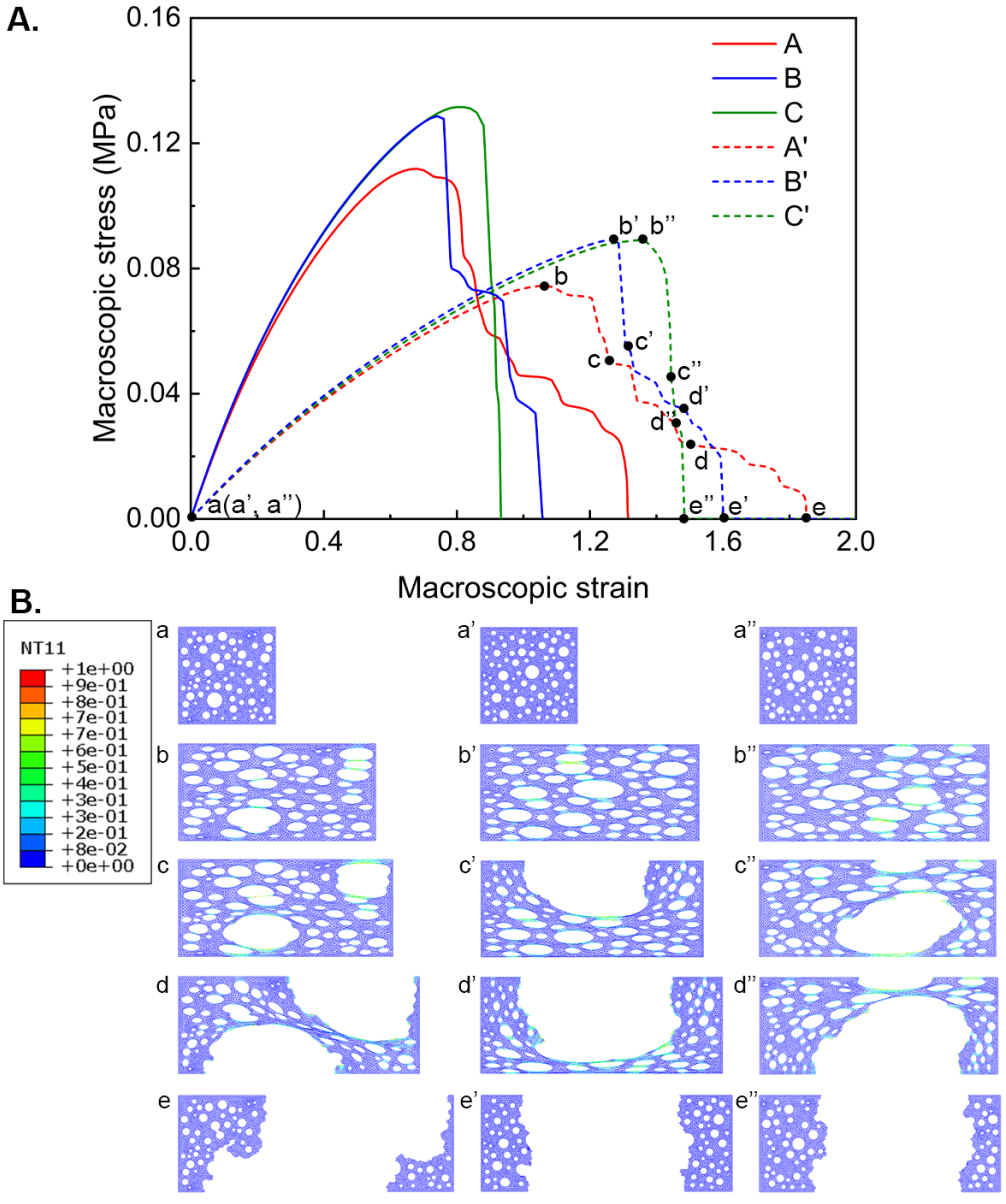


Figure 5.10: (A) The macroscopic stress-strain curves of single and multi-scale porous samples, and (B) crack paths of multi-scale porous samples.

5.6 Discussion

Researchers have consistently focused on understanding the structural and chemical compositions of mussel plaques and their impact on adhesion [6, 16, 30, 40]. Previous study has suggested that the pore arrangement within the plaque core might influence the adhesion ability [134]. However, limited attention has been paid to understanding how pore arrangement affects the mechanical behaviours of the plaque core. Tensile testing of the thread-plaque system reveals that mussel plaques can withstand considerable deformation before detachment, underscoring their high deformability (Figure 5.1c) [9, 153]. This led us to hypothesise that the pore distribution and hierarchical structure of the plaque core might also contribute to its high deformability and potentially impact other tensile properties.

Elbanna et al. (2015) conducted a semi-analytical approach to understand the effect of void arrangement on the adhesion of mussel plaques [134]. They found that plates with larger voids near the attached interface display higher stress heterogeneities, which can trap cracks in regions with low stress, thereby slowing down the propagation of cracks and resulting in higher maximum forces, increased deformability, and enhanced energy dissipation. However, the ordered and graded pores were used in the study, which differs from the natural pore distribution found in the plaque core and may influence the mechanical behaviour [134].

In this research, extensive SEM analysis was employed to obtain the pore distribution of the plaque core. Porous RVEs were generated using scaled distribution parameters to present the main geometric characteristics of the plaque core and conduct the qualitative analysis. Our results demonstrate that large-scale pore distribution significantly impacts the mechanical behaviour of single-scale porous RVEs, including final failure strain, strength,

and strain energy density.

As mentioned above, Elbanna et al. (2015) reached the conclusion that larger voids near the attached interface can lead to higher strength, deformability, and strain energy density. Our RVE-based numerical studies have suggested that increasing the normalised mean value ($\bar{\mu}$) of pore radius can statistically lead to a decreasing trend in these macroscopic material properties: final failure strain, strength, and strain energy density. While the normalised standard deviation value ($\bar{s}$) of the pore radius had an insignificant effect on these properties. Additionally, it was found that the same normalised mean value ($\bar{\mu}$) or normalized standard deviation value ($\bar{s}$) can always return highly scattered macroscopic material property values. This indicates that the values of $\bar{\mu}$ and $\bar{s}$ can not solely determine the mechanical behaviour of single-scale porous RVEs. Other factors, such as the interactions between pores and the hierarchical structure, could also play an important role.

Regarding the interactions between pores, our FE simulation results suggest that two types of failure mechanisms might occur under the same pore distribution, i.e. diffused crack pattern and concentrated crack pattern. The diffuse crack pattern elongated the crack path, which in turn led to the progressive failure mode and an increase in the final failure strain of RVEs. While the concentrated crack pattern led to rapid crack propagation and resulted in a sudden failure mode. The observed findings highlight the crucial role played by pore interactions in influencing mechanical behaviours.

Another factor, i.e. the hierarchical structure, was also examined in this research. The results indicate that the failure modes of the porous RVEs are dominated by the large-scale pores, but the hierarchical structure can

further increase the final failure strain of porous RVEs by reducing stiffness, suggesting it is also a crucial factor in achieving the high deformability of mussel plaques.

This study advances the understanding of how pore distribution and hierarchical structure within the mussel plaque core contribute to its high deformability and other material properties. These insights are crucial for mimicking the unique microstructure in the design of advanced materials. For instance, Bosnjak and Silberstein (2021) presented two chemical pathways to develop highly deformable materials with high toughness. Our research shows that altering the pore distribution or introducing the hierarchical structure might be another potential pathway to design materials with combined strong properties [174].

However, several limitations remain. For instance, the porous RVEs serve as an approximation rather than an exact replication of the porous structure of mussel plaques for the qualitative analysis in this research. In simplified SEM images of large-scale pores (Figure 5.2), the exclusion of overlapping, damaged or incomplete pores and the idealisation of irregular pores as circular may lead to discrepancies between the measurements and the true porosity and pore distribution. Future studies could focus on analysing RVEs that accurately replicate the porous structure of the mussel plaque core for quantitative analysis.[175, 176]. Additionally, understanding the scalability effects of the porous structure is also the focus of future research.

While this study uses 2D SEM images to analyse pore distribution, it is important to acknowledge that 2D data cannot fully capture the true 3D structure of the mussel plaque. The observed 2D pore shapes and sizes can vary significantly depending on the slicing plane, potentially leading

to inaccuracies in representing the 3D porous structure. To address this limitation, future work could employ methods to statistically infer 3D characteristics from 2D data or utilize advanced techniques such as 3D reconstruction or nano-computed tomography (Nano-CT). Once the accurate 3D structure of mussel plaque is obtained, a comprehensive analysis comparing the mussel plaque pore distribution with other potential distributions could be conducted in the future. Despite this, the 2D SEM analysis provides valuable preliminary insights into pore distribution that are essential for understanding the plaque's mechanical behaviour.

5.7 Conclusion

This study has systematically explored the influence of the pore distribution and hierarchical porous structures within the mussel plaque core on its tensile properties, with a specific emphasis on enhancing deformability. Our main conclusions are summarized as follows:

1. The SEM analysis of the mussel plaque core shows there are two different scales of pores within the plaque core: small-scale pores with diameters ranging from 50 nm to 800 nm and large-scale pores with diameters ranging from 1 μm to 3 μm. The size of large-scale pores follows a lognormal distribution, while the location of them follows a uniform distribution.

2. The large-scale pore distribution can significantly influence the final failure strain, strength, and strain energy density of the porous RVEs. Statistically, increasing the normalised mean value ($\bar{\mu}$) of the pore radius can lead to a decreasing trend in the value of the final failure strain, strength and strain energy density. However, the normalised

standard deviation value ($\bar{s}$) of the pore radius had an insignificant effect on these properties. Additionally, the same values of $\bar{\mu}$ or $\bar{s}$ can always return scattered values of the final failure strain, strength and strain energy density, indicating that they cannot solely determine the macroscopic material properties.

3. Two distinct failure modes (sudden and progressive) were identified under the same pore distribution. The interactions between pores led to two different crack patterns: diffused and concentrated. The diffused crack pattern extended the crack path and delayed the failure, which led to a progressive failure mode and higher final failure strain. While the concentrated crack pattern had rapid crack propagation, resulting in a sudden failure mode but with higher strength. This indicates that mussels may enhance the deformability of their plaques by sacrificing the plaques' strength to form the porous plaque core.

4. The multi-scale porous RVEs exhibited identical failure modes to the single-scale porous RVEs, indicating that the failure mechanism of the mussel plaque could be dominated by the large-scale pores. Compared to the single-scale porous RVEs, multi-scale truss RVEs had 40%-60% higher final failure strain but lower stiffness and strength. This suggests that the hierarchical structure of mussel plaques might enhance their deformability by reducing the stiffness.

Chapter 6

A biomimetic application inspired by the mussel byssus system: The quasi-static indentation analysis of carbon-fibre mesh reinforced LLDPE foams

Publication Information

Title	Quasi-static indentation analysis for carbon-fiber mesh reinforced LLDPE Foam inspired by mussel plaques
Author	Yulan Lyu, Yong Pang, Wei Sun, Shuguang Li, Tao Liu*
Status	To be submitted

6.1 Introduction

The mussel byssus system (Figure 6.1a), consisting of high-strength thread and highly deformable plaque, is known for its ability to stabilise the mussels in dynamic tidal environments and have attached force approximately 6 to 10 times mussel weight [9]. The extant literature reveals that mussel byssal threads are composed of an external cuticle layer surrounding an internal fibrous core, whereas mussel plaques feature a similar external cuticle layer encasing an internal soft foamy structure [16, 20, 66, 139, 153, 177, 178] (Figure 6.1b). Meanwhile, recent research progress has also suggested that the high-strength fibres within the mussel thread extended and embedded within the soft foamy core of the mussel plaque, forming a uniquely intricate structure [5] (Figure 6.1c).

However, the effect of this unique structure on the mechanical properties of the mussel byssus system remains unclear. In this context, it is interesting to explore the potential biomimetic design based on this unique structure and understand its mechanical behaviour. Due to the experimental condition limitations, instead of accurately duplicating this structure, the carbon fibre mesh reinforced linear low-density polyethylene (LLDPE) foams were manufactured. The design of the carbon-fibre mesh reinforced LLDPE foam in this study is directly inspired by the unique structure of the mussel byssus system, particularly the interaction between the high-strength threads and the soft, foam-like plaque. In the mussel byssus system, the threads are embedded in a soft matrix, which allows for both flexibility and strength, a combination that provides resilience in the dynamic, high-stress tidal environments. The core mechanism that inspires this research is the ability of the mussel plaque to distribute forces over a large surface area, using a fibrous network that is closely integrated into a softer, more de-

formable matrix. This configuration allows the mussel plaque to efficiently absorb and dissipate mechanical energy, making it resistant to both local damage (e.g., indentation) and larger-scale deformations.

In a similar manner, the carbon-fibre mesh in this study mimics the thread-like fibres in the plaque, embedded within a soft LLDPE foam, to explore how the positioning and number of fibre layers can influence the mechanical behavior under quasi-static indentation. While the mussel plaque uses a combination of natural materials with varying stiffness and elasticity, the carbon-fibre mesh reinforced LLDPE foam simplifies this concept by using an engineered material to achieve a similar balance between stiffness (from the mesh) and deformability (from the foam).

In particular, the quasi-static indentation (QSI) characteristics of the carbon fibre mesh reinforced LLDPE foams were analysed in this research as the first step to understanding the mechanical behaviour of this composite structure and building the foundation for future advanced biomimetic application of the composite structure of the mussel byssus system.

Quasi-static indentation (QSI) tests are a mechanical testing method used to measure the material properties of a specimen by gradually applying a force [179–182]. During these tests, a rigid indenter, often with a well-defined shape, is applied to the material at a consistent and gradual pace, enabling the determination of material properties such as hardness, elasticity, and plasticity [181–184]. In particular, the quasi-static indentation (QSI) tests can be applied to understand the low-velocity impact response and characterise various damage modes of composite structures [185, 186].

Quasi-static indentation (QSI) impact of fibre-sheet reinforced polymeric foams have been extensively studied to understand their failure behaviour under low-velocity impact [179–182]. Flores-Johnson and Li (2011) con-

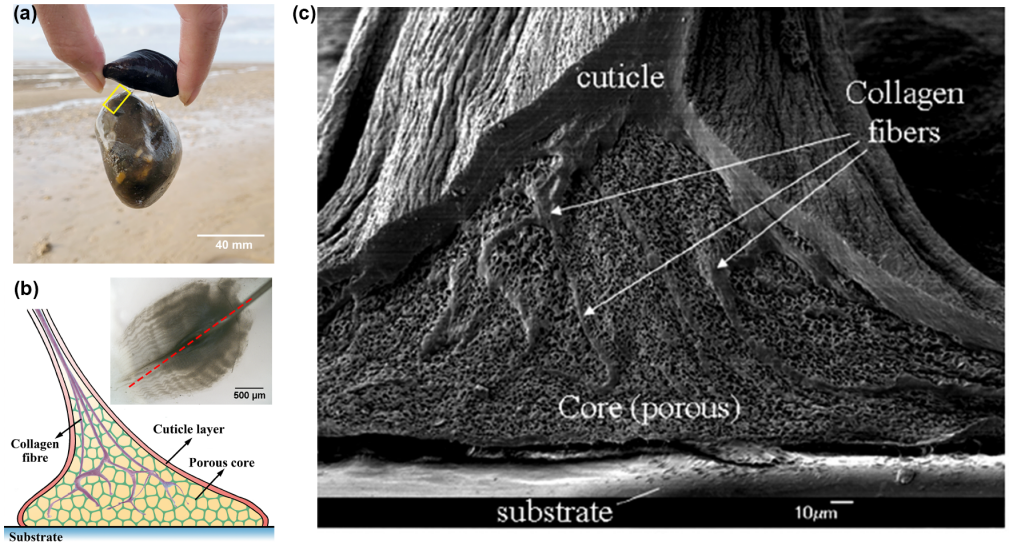


Figure 6.1: (a) A plaque–thread system of a marine mussel (from a blue mussel) [9]. (b) Schematic of the cross-section of a mussel plaque showing the internal structure, with the inset showing the top view of a real mussel plaque and the dashed line showing the direction of the section [9]. (c) Solid foam structure of a byssal adhesive plaque [8].

ducted intensive experimental investigations, concluding that both the indenter nose shape and the density of the foam core significantly influence the QSI response of polymethacrylimide (PMI) foam core reinforced by carbon fibre sheets [180]. Additionally, they also found that the type of support used during testing has a great impact on the indentation load [180]. Beyond PMI, a variety of polymeric foam cores, including polyurethane (PU) [187–189] and polyethyleneterephthalate (PET) [188, 190, 191] have been examined to understand the core material influences on energy absorption under QSI tests. Different fibre sheet reinforcements, such as carbon fibre sheets [180, 192–194] or glass fibre sheets [195–197] have also been employed in different research. Recent studies have progressed to analyse the QSI responses of bio-inspired 3D printed cores with glass fibre sheets, revealing that core geometry significantly affects damage behaviour [198]. This finding suggests a promising direction for the future design of fibre-reinforced materials [198].

However, most studies have focused on analysing the QSI behaviour of polymeric foams reinforced with fibre sheets rather than fibre mesh [179–182, 192–194]. This study focuses on mimicking the configuration of thread fibres embedded within the foamy core of mussel plaques by fabricating the carbon fibre mesh and polymeric foam core as an integrated unit. The fibre mesh is more closely matched to the mussel thread fibre configuration than the fibre sheet. Therefore, this research is driven by the limited understanding of the quasi-static indentation (QSI) characteristics of fibre mesh reinforced polymeric foams and tries to analyse its QSI behaviour as the first step to understanding this composite structure and showing a potential biomimetic example of the mussel byssus system.

Overall, this study systematically reports comprehensive experimental data on the quasi-static indentation (QSI) behaviour of carbon fibre mesh reinforced linear low-density polyethylene (LLDPE) foam for various indenter nose shapes, including flat-circular, hemi-spherical, conical, and truncated. Four distinct configurations of carbon fibre mesh reinforced LLDPE foams were analysed to understand the impact of carbon fibre mesh positioning and the number of layers on their QSI behaviour and failure modes (top-reinforced, bottom-reinforced, double (top and bottom) reinforced, and middle-reinforced). Two different support types (framed support and solid support) were also examined to understand the bending response of the carbon fibre mesh-reinforced LLDPE foams under indentation loading. The findings of this research deepen our understanding of the mechanical behaviour of carbon fibre mesh reinforced LLDPE foams. Most importantly, it builds the foundation for the future biomimetic design of this unique microstructure of the mussel byssus system.

6.2 Experimental methods

6.2.1 Sample preparation and tests setup for uniaxial compression tests

The linear low-density polyethylene (LLDPE) 8035 WS Black 9001 powder was mixed with 2% by weight of the blowing agent azodicarbonamide (ADC/M-C1) (Figure 6.2b) [199]. The material properties of both components are shown in Tables 6.1 and 6.2, respectively [199]. Subsequently, 50 g of the mixed powder was transferred into a 50x50x50 mm (inner cube size) mould, which was securely closed with a lid and fastened using hexagonal bolts (Figure 6.2b). This assembly was placed in an oven and heated at 200°C for one hour (Figure 6.2b). The heat treatment facilitated the fluidisation of the LLDPE and initiated the release of gases from ADC/M-C1 through a chemical reaction, forming bubbles within the molten polymer (Figure 6.3). Following the heating process, the mould was removed from the oven, and the resulting LLDPE foams were allowed to cool at room temperature for 12 hours before being demoulded.

To adhere to ASTM C365 standards [200], which prescribe methods for testing the compressive strength of sandwich core materials, the samples were resized (Figure 6.2b). The initial cubic samples with dimensions of 50x50x50 mm were cut down to smaller cubes measuring 25x25x25 mm (nominal size) to satisfy the minimum facing area requirement of 625 mm^2 for the tests [200].

In the uniaxial compression test, an Instron 68TM-50 test machine with a load capacity of 50 kN was employed (Figure 6.2a), operating at a constant speed of 1 mm/min to satisfy the quasi-static condition requirements

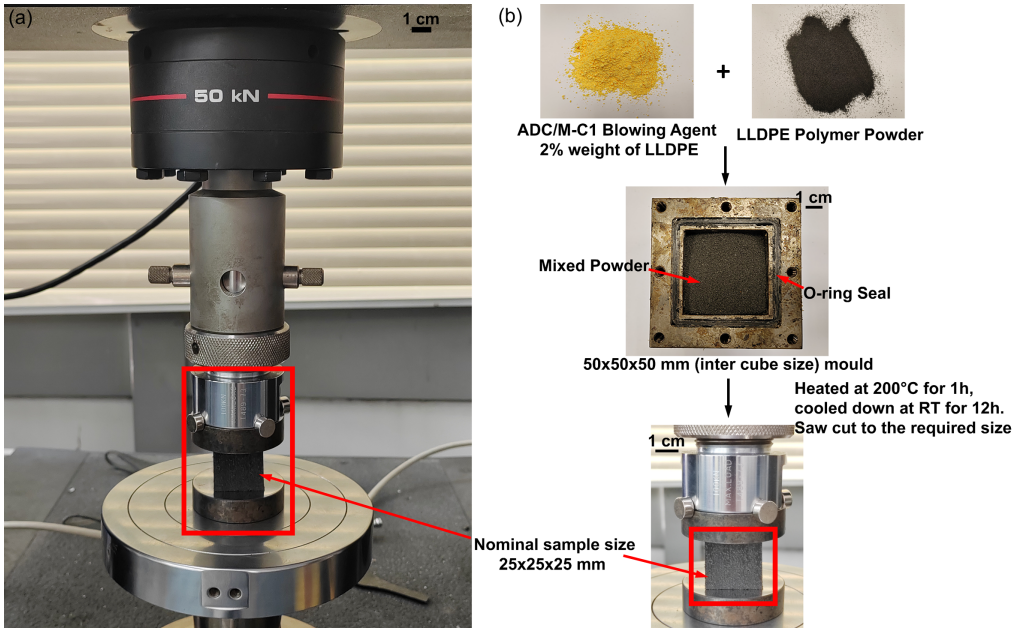


Figure 6.2: (a) Uniaxial compression test setup with an Instron 68TM-50 test machine, and (b) the manufacturing process of the LLDPE foam for the uniaxial compression test.

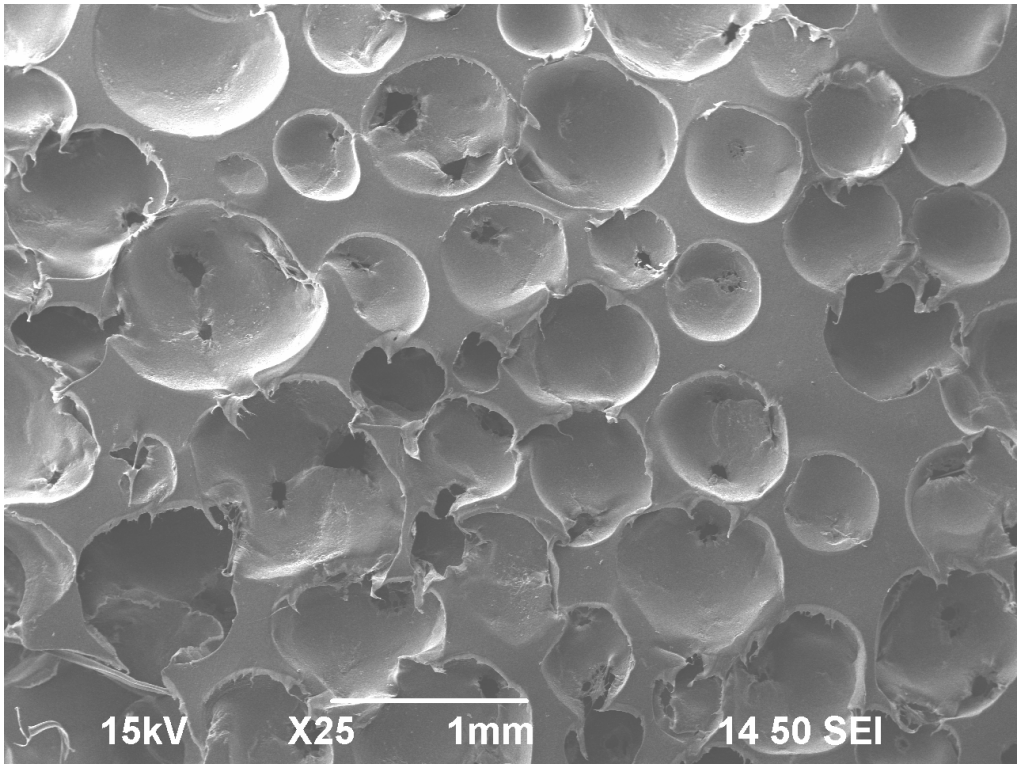


Figure 6.3: A SEM image showing the microstructure of the LLDPE foam.

[187]. Three samples underwent testing, from which stress-strain curves

were derived:

$$\sigma = \frac{F}{A} \tag{6.1}$$

$$\varepsilon = \frac{D}{l} \tag{6.2}$$

where σ is the uniaxial compressive stress, ε is the uniaxial compressive strain. F is the compressive load, D is the compressive displacement. A is the compressed contact surface area (A=625 mm^2) and l is the side length of the sample (l=25 mm).

Table 6.1: Material properties of LLDPE 8035 WS Black 9001 powder.

Melting point	115°C-155°C
Boiling point	Not Applicable
Density	0.910-0.950 g/cm^3
Tensile strength	17 MPa
Flexural modulus	0.35 GPa

Table 6.2: Material properties of the blowing agent ADC/M-C1.

Melting point	>180°C
Decomposes temperature	>75°C
Colour	Yellow
Odour	Negligible

6.2.2 Sample preparation and tests setup of quasi-static indentation tests

In order to create carbon fibre mesh reinforced LLDPE foams for the quasi-static indentation tests, the Mapegrid C 170 high-strength carbon fibre mesh with a 10x10 mm mesh size was incorporated (Figure 6.4d) [201]. The material properties of the carbon fibre mesh, as provided by the supplier, are detailed in Table 6.3 [201]. The carbon fibre mesh was positioned within the mould at designated locations with the mixed powder (Figure

6.4e). This mixed powder is the same mixed powder used in the uniaxial compression test. As the powder melted into a viscous fluid during heating, it naturally adhered to the fibre mesh. This integration continued as the material cooled and was demoulded, forming a unified structure without the typical complications associated with adhesives (Figure 6.4d). 135 g of mixed powder was used per sample to ensure consistent density between the quasi-static indentation test samples and the uniaxial compressed test samples. Subsequently, the demoulded samples (235x80x20 mm) were sectioned into 80x80x20 mm (nominal size) blocks for the experiments (Figure 6.4d). Previous studies have employed sample sizes ranging from 50 to 100 mm in length and 10 to 100 mm in thickness [180, 187, 188, 202]. While there is no set standard for sample dimensions, the sizes used in this study are within the range documented in earlier research [180, 187, 188, 202].

To investigate the impact of carbon-fibre mesh positioning and the number of layers on the quasi-static indentation behaviour of the LLDPE foam, four variants were produced: top-reinforced foam (TOF), middle-reinforced foam (MIF), bottom-reinforced foam (BOF), and double-reinforced foam (DOF) (Figure 6.4e). Quasi-static indentation experiments were conducted on these different fibre-reinforced LLDPE foams, with three specimens examined for each variant to ensure consistency (Appendix E.1). Various indenter nose shapes were used to study their effect on the QSI behaviour of the samples, including flat-circular, hemi-spherical, conical, and truncated indenters (Figure 6.4a). The dimensions of these indenters are consistent with previous research [180] and are shown in Figure 6.4a. The indenters were then installed in a Servo hydraulic load frames Mand (A12) testing machine, and the tests were displacement-controlled at a speed of 1mm/min [187] at room temperature (23°C).

The bending effect was also analysed by comparing the results of the clamp-

ing fixture (framed support) (Figure 6.4b) and those placed directly on the sample stage of the machine (solid support) (Figure 6.4c). The clamping fixture with a 50x50 mm window in the middle was designed to fix the specimens during the indentation tests (Figure 6.4b). Four screws were tightened to make sure there was no movement in the boundaries (Figure 6.4b). The QSI tests under frame support were loaded until a sustained load drop was observed in the force-displacement curve. The QSI tests under solid support were loaded to a displacement of 15 mm to ensure a controlled and safe testing environment, considering the sample thickness of 20 mm. Because the nose length for conical and hemi-spherical indenters was 10 mm, both surface indentation images at d=10 mm and d=15 mm were analysed.

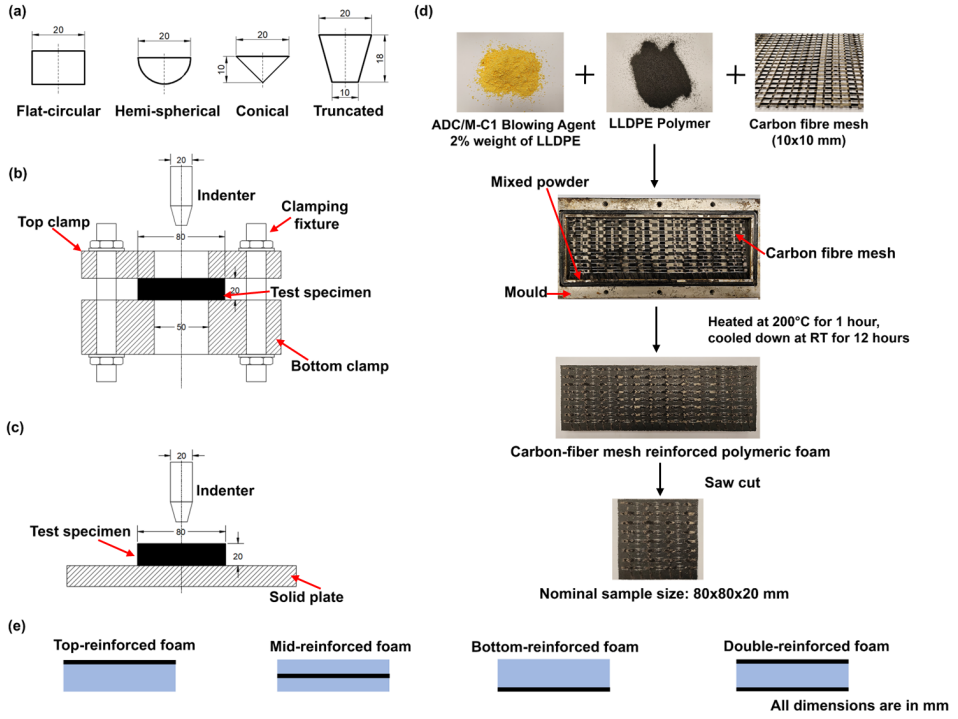


Figure 6.4: (a) The schematic drawings of four different indenter noses, (b) schematic drawings of framed support condition, (c) schematic drawings of solid support condition, (d) the manufacturing process of carbon-fibre reinforced LLDPE foam, and (e) four variants of fibre-reinforced polymeric foams: top-reinforced foam (TOF), mid-reinforced foam (MIF), bottom-reinforced foam (BOF), and top and bottom-reinforced foam (DOF).

Table 6.3: Material properties of the Mapegrid C 170 high-strength carbon fibre mesh.

Tensile strength (kN/m)	>240
Modulus of elasticity (GPa)	$252 \pm 2\%$
Load-resistant area per unit of width (mm^2/m)	48
Equivalent thickness of dry fabric (mm)	0.048
Elongation at failure (%)	2

6.3 The results of experimental studies

6.3.1 Uniaxial compression test results

Figure 6.5 shows uniaxial compressive stress-strain curves for pure LLDPE foams. Three typical regimes were observed from the curves: (1) a linear-elastic regime, (2) a plateau regime characterised by nearly constant or marginally increasing stress, and (3) a densification regime in which stress escalates rapidly with the strain increments. The average values of Young's modulus E, yield strain ε_y and plateau stress σ_{pl} obtained from the linear-elastic regime for three samples were shown in Table 6.4.

Table 6.4: Mechanical properties of pure LLDPE foams.

Young's modulus (MPa)	100
Yield strain	0.1
Plateau stress (MPa)	4.2

6.3.2 Quasi-static indentation (QSI) test results

Quasi-static indentation tests were conducted under two different support conditions: framed support (Figure 6.4b) and solid support (Figure 6.4c). The framed support condition allows for sample bending, whereas the solid support condition restricts it. By comparing the results from these two support conditions, we can gain insights into the effect of bending on the

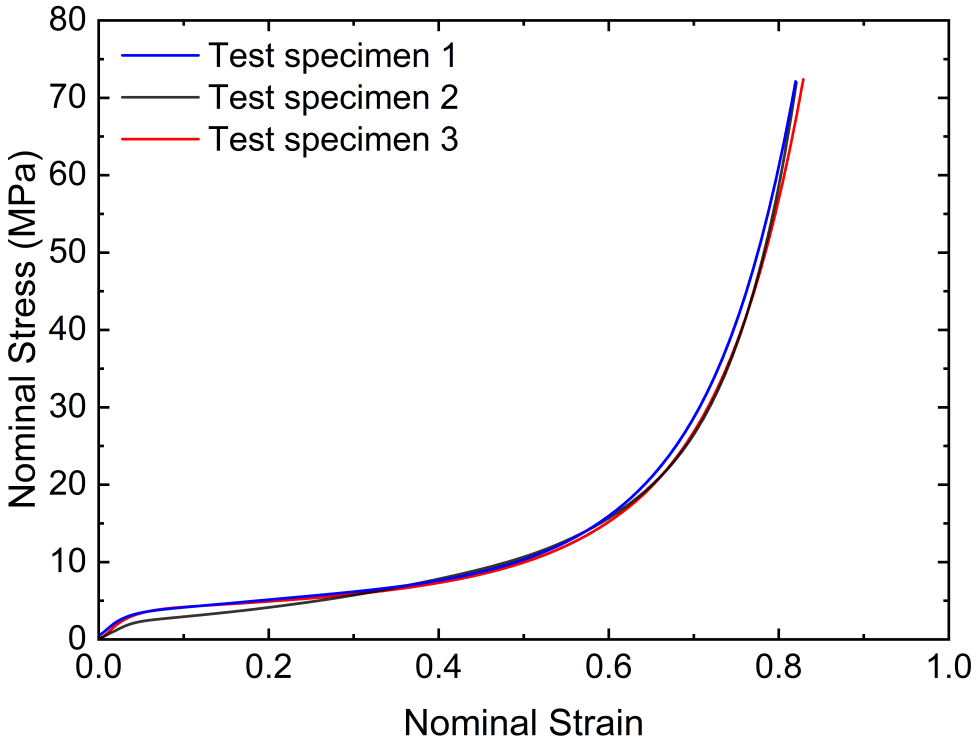


Figure 6.5: The uniaxial compression stress-strain curves for three pure LLDPE foams.

QSI behaviour of fibre mesh-reinforced LLDPE foams and the role of fibre mesh reinforcement under bending effects.

QSI force-displacement curves under framed support

Flat-circular indenter Because the flat-circular indenter nose has the same size as the indenter body, there were no dimensional changes that could affect the QSI behaviours of samples. The strain concentration and stress singularity led to an initial linear-elastic regime in the QSI force-displacement curves under the flat-circular indenter (Figure 6.6a). During this phase, the QSI force-displacement curves for all variants of fibre mesh reinforced LLDPE foams overlapped with that of the pure LLDPE foam (NOF), indicating that the fibre mesh might not contribute to reinforcement during this initial elastic phase (Figure 6.6a).

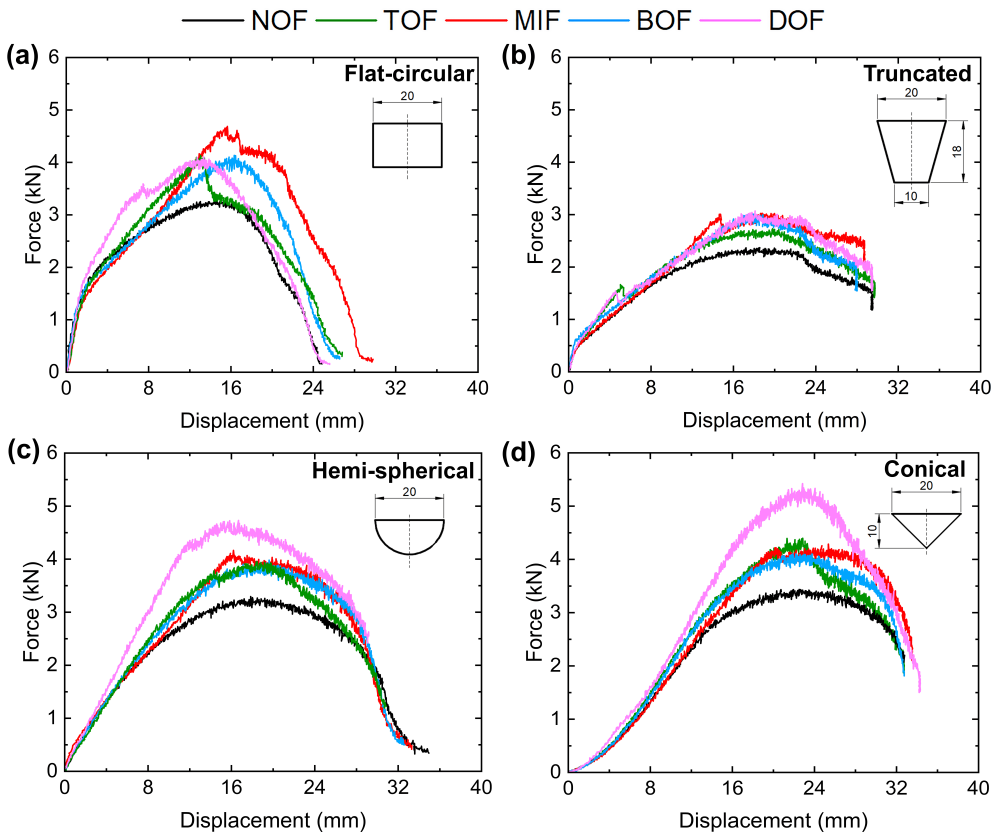


Figure 6.6: The QSI force-indentation displacement curves for five variants of the fibre mesh-reinforced LLDPE foams under four different indenter noses using framed supporting: (a) flat-circular indenter, (b) truncated indenter, (c) hemi-spherical indenter, and (d) conical indenter.

Following the initial elastic stage, the load continued to increase linearly but with varying slopes (Figure 6.6a). The double fibre mesh reinforced LLDPE foam (DOF) exhibited the steepest slope among all variants. The single fibre mesh reinforced LLDPE foams (TOF, MIF and BOF) displayed nearly identical slopes (Figure 6.6a). These slopes were higher than that of the pure LLDPE foam (NOF) but lower than that of the double fibre mesh reinforced LLDPE foam (DOF) (Figure 6.6a). This indicates that the fibre mesh can effectively enhance the stiffness of LLDPE foams under framed support conditions. Increasing the number of fibre mesh layers can further enhance the stiffness, while the position of the fibre mesh appeared to have minimal impact on the reinforcement of the LLDPE foams. Additionally, a sudden drop in force was observed in the MIF, TOF, and DOF

samples, suggesting that fibre breakage might occur to varying degrees in these variants.

Truncated indenter The QSI force-displacement curves under the truncated indenter exhibited an initial linear-elastic phase, similar to the curves observed under the flat-circular indenter (Figure 6.6b). Following this phase, the indentation force continued to increase linearly but with a lower slope. All the fibre mesh reinforced LLDPE foams had slopes almost identical to the pure LLDPE foams during these two phases, indicating that both the position and number of fibre mesh layers had negligible effects on the stiffness of the LLDPE foams (Figure 6.6b).

After these two phases, it was found that the fibre mesh reinforcement can effectively delay the curves' transition to a plateau regime, allowing the foams to reach higher maximum indentation forces under the truncated indenter (Figure 6.6b). However, increasing the number of reinforcing fibre mesh layers under the truncated indenter did not significantly affect the maximum indentation force of the LLDPE foams. A sudden reduction in force was also observed in the TOF, MIF, and DOF samples (Figure 6.6b).

Hemi-spherical indenter The QSI force-displacement curves under a hemi-spherical indenter demonstrated an initial linear-elastic regime (Figure 6.6c). The single fibre mesh-reinforced LLDPE foams (TOF, MIF and DOF) exhibited a slope comparable to that of the NOF samples, while the DOF samples exhibited a higher slope than the others. The alterations in fibre positioning did not affect the slope of the indentation force for single fibre mesh-reinforced LLDPE foams. As the indentation depth continued to increase, the force increase rate for pure LLDPE foam (NOF) samples began to decelerate, eventually reaching a plateau phase. Meanwhile, the force in fibre-reinforced LLDPE foams (TOF, MIF, BOF, and DOF) con-

tinued to rise linearly for a longer period before gradually slowing down and reaching a plateau. There was no abrupt decline in force for any of the curves under the hemi-spherical indenter.

Conical indenter The indentation force exhibited a non-linear increase with an increasing tangent slope for all foam samples under the conical indenter (Figure 6.6d). The QSI force-displacement curves were nearly identical for all foams during the initial non-linear increase stage, indicating that the fibre mesh reinforcement had a negligible effect on indentation resistance in this phase (Figure 6.6d). Following this non-linear increase phase, as the indentation depth increased, the QSI force-displacement curve of the pure LLDPE foam quickly reached the plateau regime (Figure 6.6d).

In contrast, the presence of the fibre mesh effectively delayed the decrease in the slope under the conical indenter, allowing the fibre mesh-reinforced foams to achieve higher indentation resistance forces. The double fibre mesh reinforced foams (DOF) reached the highest maximum indentation force, suggesting that increasing the number of fibre mesh layers can enhance the LLDPE foam's resistance to the conical indenter under framed support (Figure 6.6d). However, in samples containing a single layer of fibre mesh, variations in fibre positioning did not significantly influence the indentation force (Figure 6.6d). Additionally, a sudden drop in force due to fibre mesh breakage was observed in the TOF sample (Figure 6.6d).

QSI material parameters analysis under framed support

To analyse the impact of indenter nose shape and fibre mesh reinforcement on the QSI behaviour of LLDPE foams, three material parameters were extracted from the QSI force-displacement curves under framed support: maximum force, indentation depth at maximum force, and absorbed energy.

The absorbed energy was determined by calculating the area under the force-displacement curve.

Fibre mesh reinforcement could increase the maximum force for LLDPE foams under framed support, regardless of the indenter nose shape (Figure 6.7a). Increasing the fibre mesh layers further increased the maximum force, but this effect was only significant under the conical and hemi-spherical indenters (Figure 6.7a). Conversely, the position of the fibre mesh within single-layer reinforced LLDPE foams had a negligible impact on the maximum force (Figure 6.7a). The truncated indenter consistently exhibited a lower maximum force than the other three, regardless of the fibre mesh reinforcement (Figure 6.7a).

The conical indenter consistently achieved the greatest indentation depths across all fibre mesh configurations, highlighting its higher penetrative capability under maximum force conditions (Figure 6.7b). In contrast, the flat-circular indenter exhibited the least penetration, maintaining the shallowest indentation depths throughout the experimental range (Figure 6.7b).

All sample variants tested under the truncated and flat-circular indenters showed lower energy absorption, suggesting that the samples were less effective at dissipating energy under the impact of these indenters (Figure 6.7c). In comparison to the pure LLDPE foam (NOF), single-layer fibre mesh reinforced foams (TOF, MIF, and BOF) exhibited higher energy absorption capacity, although changing the position of the fibre mesh had a limited effect on the amount of energy absorbed (Figure 6.7c). Moreover, increasing the number of fibre mesh layers can further increase the energy absorption of the carbon fibre mesh reinforced LLDPE foams, with the increase being more pronounced for samples tested under hemi-spherical and

conical indenters (Figure 6.7c).

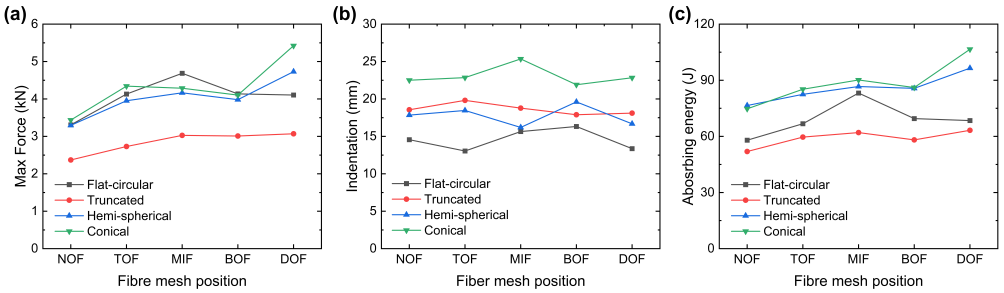


Figure 6.7: Typical material parameters for three variants of the fibre mesh reinforced LLDPE foams with four different indenter noses using framed supporting: (a) max force (kN), (b) indentation depth at max force (mm), and (c) absorbing energy (J).

QSI force-displacement curves under solid support

QSI tests were conducted on five variants of LLDPE foams under solid support conditions: pure LLDPE foams (NOF), LLDPE foams reinforced with top fibre mesh (TOF), middle fibre mesh (MIF), bottom fibre mesh (BOF), and double fibre mesh (DOF). The QSI force-indentation displacement curves for these fibre-mesh reinforced LLDPE foams using different indenters are illustrated in Figure 6.8.

Under flat-circular indenters, the QSI force-displacement curves revealed three distinct regimes: (1) linear-elastic, (2) plateau, and (3) densification (Figure 6.8a). The overall force-displacement curves exhibited minimal differences among all five sample types, suggesting that the positioning and number of fibre mesh layers had a limited impact on the QSI behaviour of LLDPE foams under solid support. Notably, fluctuations were observed in the curves of the TOF, MIF and DOF samples, indicating the potential fibre breakage, though this did not significantly affect the overall QSI force-displacement responses (Figure 6.8a).

Similarly, the QSI force-displacement curves obtained with the truncated

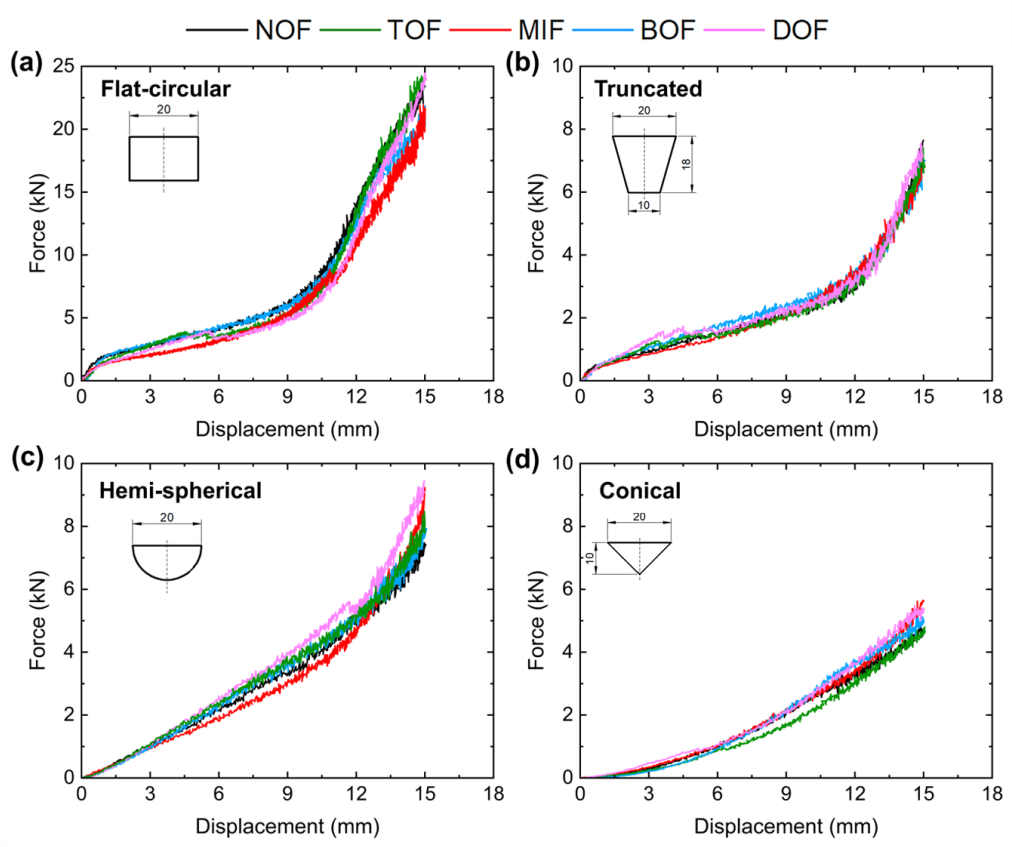


Figure 6.8: The QSI force-indentation displacement curves for three variants of the fibre mesh-reinforced LLDPE foams with four different indenter noses using solid supporting: (a) Flat-circular indenter, (b) truncated indenter, (c) hemi-spherical indenter, and (d) conical indenter.

indenter also displayed three distinct regimes (Figure 6.8b). Nevertheless, the recorded forces were found to be smaller than those observed under the flat-circular indenter. This may be attributed to the smaller contact area and the resulting localised stress concentration. The near coincidence of the curves for all five foam types under the truncated indenter suggests that fibre mesh reinforcement might have minimal influence on the LLDPE foams' QSI performance under solid support. Fluctuations were observed in both TOF and DOF samples between d=3-6 mm (Figure 6.8b).

In contrast to the flat-circular and truncated indenters, the curve under the hemi-spherical indenter began with a linear increase in force with indentation depth, transitioning gradually into the densification phase (Figure

6.8c). The similarity in curves across different sample types shows the negligible effect of fibre mesh under solid support conditions. An obvious fluctuation was found in the DOF sample (Figure 6.8c).

Under the conical indenter, the force increased non-linearly with an increasing slope as the indentation depth grew (Figure 6.8d). However, the resistance force under the conical indenter was lower than that under the other three indenters. The curves for different fibre mesh reinforcement types were almost identical, with fluctuations observed in the TOF and DOF samples. This indicates a consistent response regardless of the fibre mesh reinforcement, emphasising the limited role of fibre mesh in reinforcing LLDPE foams under solid support.

6.3.3 The QSI behaviour comparison between framed and solid support

This section compares QSI force-displacement curves and surface indentation images for NOF and TOF LLDPE foams under framed and solid support conditions. The analysis of DOF, MIF, and BOF LLDPE foams has been omitted because their curves lack sensitivity to the fibre mesh position/number under solid support, and their surface indentations are similar to those observed in NOF and TOF LLDPE foams.

The QSI behaviour comparison of pure LLDPE foams (NOF) between framed and solid support

Figure 6.9 presents the QSI force-displacement curves and surface indentation images of pure LLDPE foams under different indenters and support conditions. The results demonstrated distinct differences in QSI responses

and surface indentation characteristics between different indenters and support conditions.

The greatest discrepancy between the QSI force-displacement curves under two different support conditions was observed under the flat-circular indenter (Figure 6.9a). The curves observed under framed support exhibited only two regimes: linear elastic and plateau. However, the curves observed under solid support included an additional densification regime along with these two regimes (Figure 6.9a). This may be because the large contact area of the flat-circular indenter crushed the foam and caused it to reach the densification stage more quickly, resulting in an exponential increase in the indentation force under solid support. In contrast, the window in the framed support allowed bending deformation, leading to a reduction in the densification and indentation force of the foams. A similar phenomenon was observed in the QSI force-displacement curves with the truncated indenter (Figure 6.9b). However, because the contact area of the truncated indenter is smaller than that of the flat-circular indenter, the difference in force between the two curves was considerably less—6 kN compared to 20 kN for the flat-circular indenter at d=15 mm (Figure 6.9b).

For the hemi-spherical indenter, the QSI force-indentation curve under solid support exhibited a linear elastic regime up to 10 mm. Between 10 mm and 15 mm, the indenter body began to crush the foam, causing the curve to transition from the linear elastic regime to a densification regime (Figure 6.9c). In contrast, the force-displacement curves of the frame-supported foams showed a nonlinear and slow increase under hemi-spherical indenter, while the slope of the curve gradually decreased (Figure 6.9c). The observed difference may be attributed to bending deformation under framed support. However, because the contact area of the hemispherical indenter increased gradually during compression, the resulting force difference

was less pronounced compared to the flat-circular indenter, which has a constant and larger contact area (Figures 6.9a and c).

The QSI force-displacement curves under the conical indenter exhibited nonlinear behaviour in both support conditions (Figure 6.9d). The curves were characterised by a gradual increase in force at lower displacements, followed by a more abrupt rise as displacement increased (Figure 6.9d). However, for the frame-supported foam, the force-displacement curve showed a smaller increase in force at higher displacements compared to the solid-supported foam (Figure 6.9d). This suggests that bending deformation under the frame support may also reduce localized stress concentration and densification with the conical indenter.

The surface indentation images provided corroboration of these findings. As displacement increased, the bending deformation in the frame-supported foams became more pronounced, leading to shallower indentations compared to the solid-supported foams, regardless of the indenter shape (Figure 6.9).

The QSI behaviour comparison of top fibre mesh reinforced (TOF) LLDPE foams between framed and solid support

The impact of varying support types on QSI responses and surface indentation of the top fibre mesh-reinforced LLDPE foams (TOF) was investigated, as illustrated in Figure 6.10.

The overall QSI force-displacement curves for the top fibre mesh-reinforced LLDPE foams were similar to those of pure LLDPE foams (Figures 6.9 and 6.10). The QSI curves for the top fibre mesh-reinforced LLDPE foams under solid support showed fluctuations in all four indentations, which might

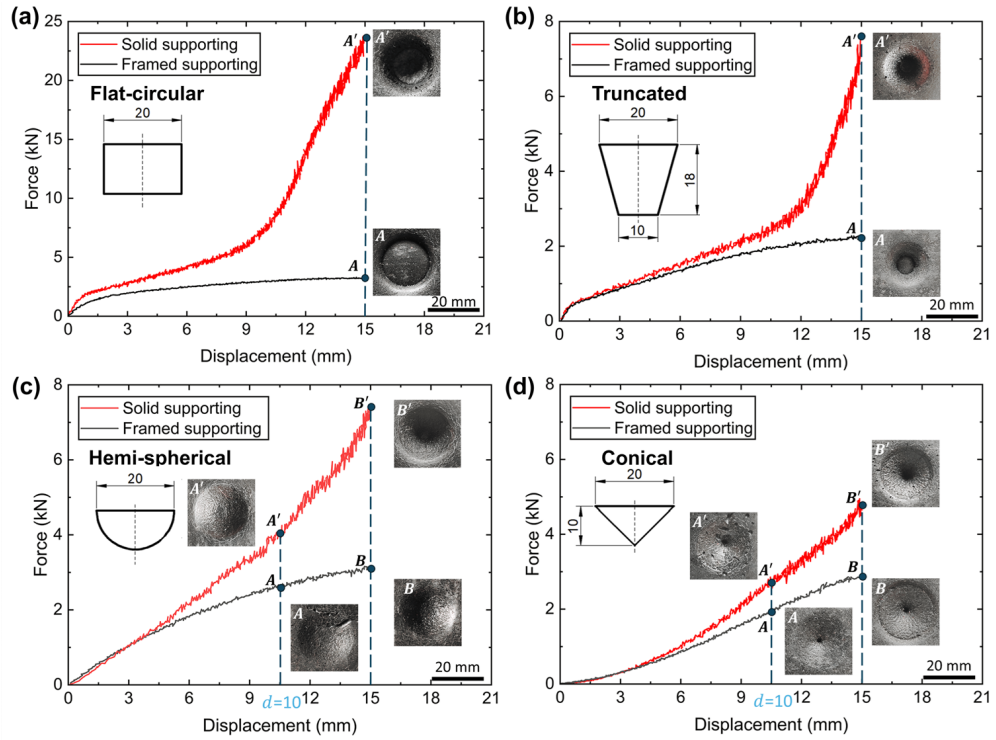


Figure 6.9: Comparison of QSI force-indentation displacement curves and surface indentation of frame-supported and solid-supported LLDPE foams: (a) flat-circular indenter, (b) truncated indenter, (c) hemi-spherical indenter, and (d) conical indenter.

be attributed to fibre breakage (Figure 6.10). In particular, the fibre mesh under the flat-circular and truncated indenters showed apparent breakage in the surface indentation images (Figures 6.10c and d). In contrast, the QSI curves for the top fibre mesh-reinforced LLDPE foams under framed support only showed fluctuations under flat-circular and truncated indenters (Figures 6.10a and b). Notably, under the flat-circular indenter, the fluctuations in the curve under framed support occurred later than those under solid support, suggesting that bending deformation from the framed support could reduce localized stresses and delay fibre mesh breakage (Figures 6.10a).

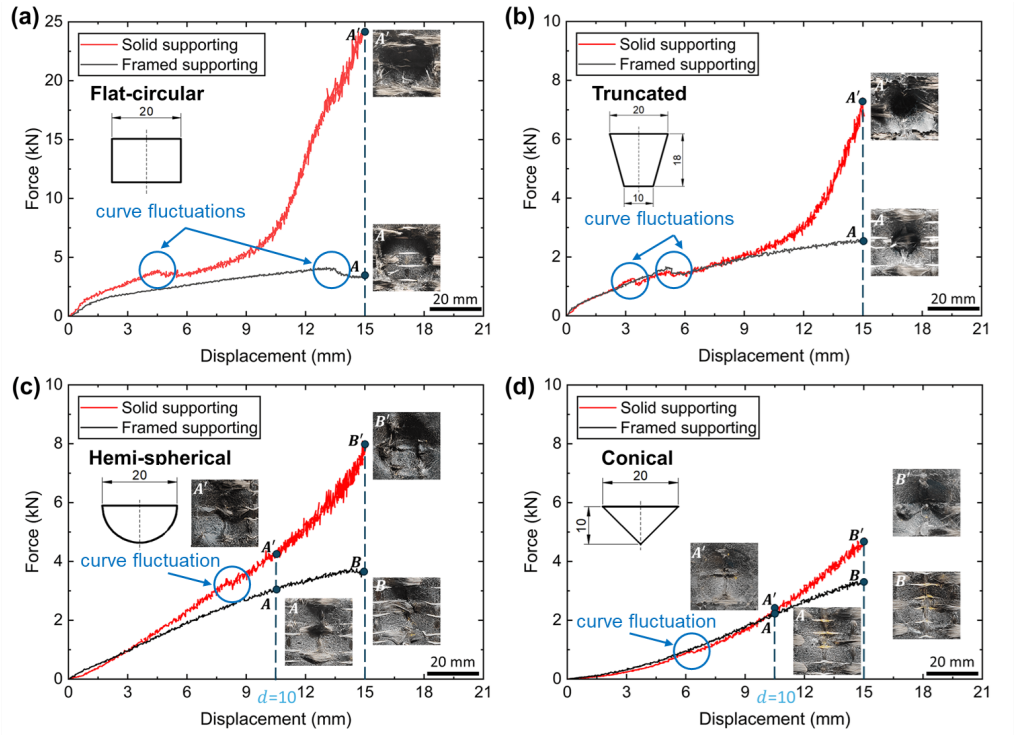


Figure 6.10: Comparison of QSI force-indentation displacement curves and surface indentation of top fibre mesh reinforced LLDPE foams with framed and solid supporting: (a) flat-circular indenter, (b) truncated indenter, (c) hemi-spherical indenter, and (d) conical indenter.

6.3.4 Fibre mesh failure modes analysis

The fibre mesh failure was mainly concentrated in the TOF samples and the top surface of DOF samples across all four indentations under solid support, with the failure mode being fibre breakage (Figure 6.10).

Two different failure modes of the fibre mesh were observed when the foams were subjected to failure under frame support: fibre breakage and fibre pull-out (Figure 6.11). Fibre breakage was observed at the top surface of TOF and DOF samples under all indenter types, whereas fibre pull-out was noted in MIF, BOF, and the bottom surface of DOF samples under all indenters (Figure 6.11). These findings indicate that the indenter nose shapes might have a negligible effect on the failure modes of the fibre mesh. Instead, the failure modes are primarily influenced by the fibre mesh's location within

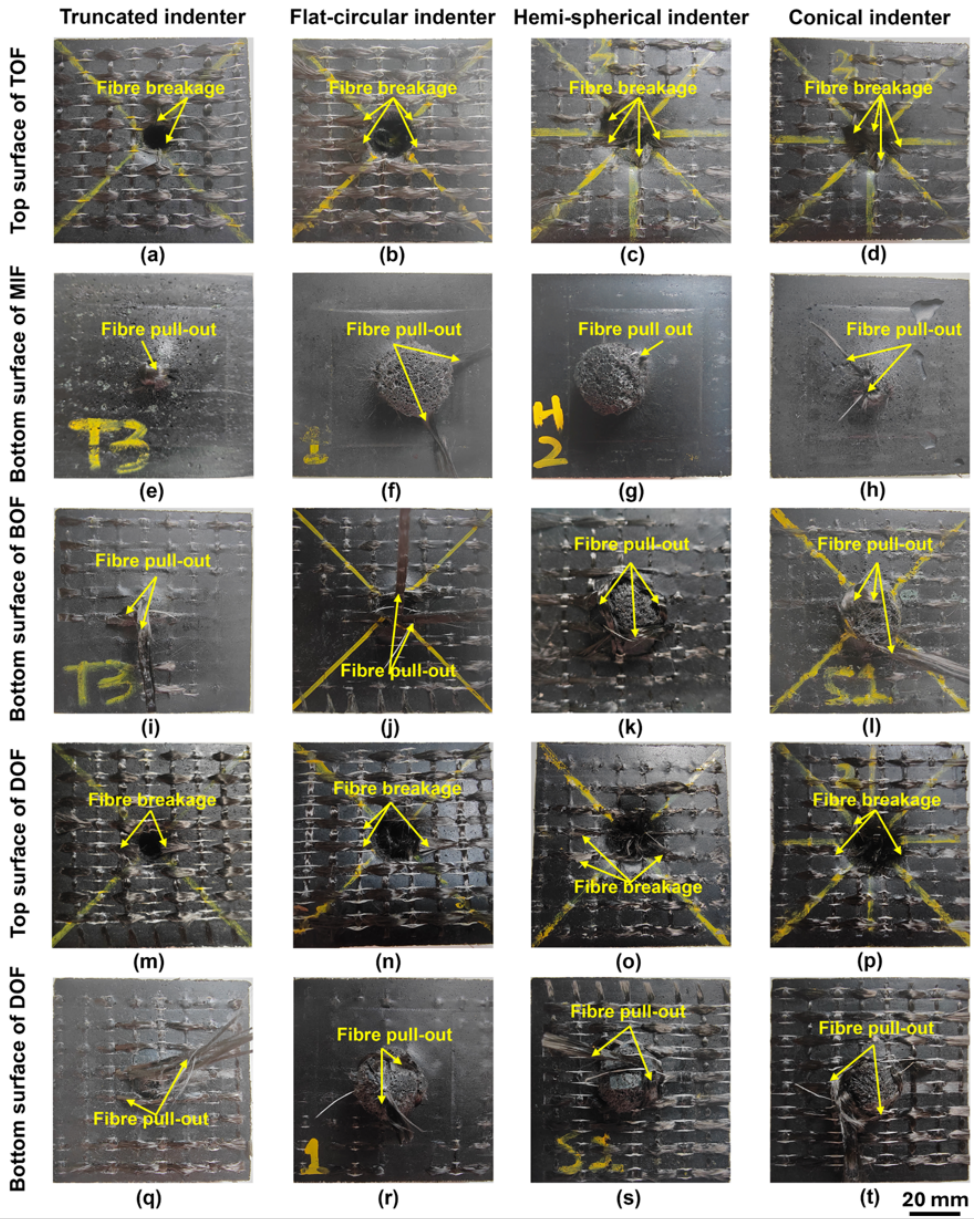


Figure 6.11: The fibre mesh failure modes under framed support: (a)-(d) fibre breakage on the top surface of TOF samples under four indenters, (e)-(h) fibre pull-out on the bottom surface of MIF samples under four indenters, (i)-(l) fibre pull-out on the bottom surface of BOF samples under four indenters, (m)-(n) fibre breakage on the top surface of DOF samples under four indenters and (q)-(t) fibre pull-out on the bottom surface of DOF samples under four indenters.

the foams.

6.4 Discussion

This study was inspired by the unique structure of mussel thread fibres embedded within the plaques' foam core and demonstrated a preliminary biomimetic application based on the mussel byssus system. The carbon-fibre mesh-reinforced linear low-density polyethylene (LLDPE) foams inspired by this unique structure were therefore manufactured. While previous studies have extensively explored fibre sheet reinforcements in polymeric foams [180, 187, 188], this study focuses on the QSI behaviour of fibre mesh reinforced LLDPE foams as it is more structurally similar to the interaction within the mussel byssus system (Figure 6.1c).

Under solid support, the carbon fibre mesh reinforced LLDPE foams under a flat-circular indenter exhibited the highest indentation force regardless of the fibre mesh. It is likely due to the extensive contact area causing a crushing effect. In contrast, foams tested under the conical indenter demonstrated the lowest indentation force among the four indenter types under solid support, as the deformation was dominated by tearing, with no significant crushing of the foam core after the initial perforation. Foams subjected to hemi-spherical and truncated indenters displayed intermediate indentation resistance under solid support. Similar effects from the indenter nose shape were also observed in fly ash-reinforced polyurethane foams [187], glass-fibre fabric-reinforced polymer sandwich panels [188] and carbon fibre fabric reinforced polymer polymeric foams [180]. However, our study revealed that the number and position of the fibre mesh had an insignificant effect on the QSI behaviour of carbon fibre mesh reinforced LLDPE foams under solid support. The conclusion is different from the previous studies that found the fibre sheet reinforcement can effectively improve the QSI resistance of the fibre sheet reinforced polymeric foams

[179, 180]. This discrepancy might indicate that, compared to fibre mesh, fibre sheets can provide more substantial reinforcement for the foam core under solid support. The overall QSI response of carbon fibre mesh reinforced LLDPE foams under solid support is predominantly governed by the properties of the LLDPE foam core.

Comparing the QSI behaviour of carbon fibre mesh-reinforced LLDPE foams under solid and framed support reveals a key difference. The indenter resistance of all foams is lower under framed support than under solid support, regardless of the indenter type. This could be attributed to the qualitative observation that the QSI behaviour of carbon fibre mesh-reinforced LDPE foam supported by the frame is a combination of local indentation and global bending. The framed support allowed global bending deformation within the foams, which reduced the indentation resistance and densification effect compared to the solid support. However, unlike the limited effect of fibre mesh reinforcement under solid support, the fibre mesh reinforcement under framed support could effectively enhance the indentation resistance of LLDPE foams by reducing the bending effect. Increasing the number of fibre mesh layers further increased indentation resistance, particularly under hemispherical and conical indenters. In contrast, the positioning of the fibre mesh layer had minimal impact on the indentation resistance of LLDPE foams. Additionally, unlike the carbon fibre mesh reinforced foams in our research, the support condition had a less pronounced effect on carbon fibre sheet reinforced foams [180]. This might indicate that the carbon fibre sheet could better reduce the foam bending under framed support, thus increasing resistance to indentation and reducing the difference between support conditions.

Two distinct fibre failure modes were observed in the carbon fibre mesh reinforced LLDPE foams under framed support: fibre breakage, concen-

trated in TOF samples and the top surface of DOF samples, and fibre pull-out, concentrated in MIF samples, BOF samples, and the bottom surface of DOF samples. While previous studies have indicated that indenter nose shape can influence fibre failure modes in carbon fibre sheet reinforced foams under framed support [180], our findings suggest that in carbon fibre mesh reinforced foams, the failure modes are primarily influenced by the positioning of the fibre mesh layer. The fibre breakage in top surface reinforcement might be due to the direct and high stress experienced at the surface, leading to immediate failure of the fibre mesh. In contrast, fibre pull-out in middle and bottom reinforcement layers may be driven by shear forces and the load transfer process within the foam matrix, causing the fibres to be extracted rather than broken.

Overall, this research provides a preliminary biomimetic example based on the microstructure of the mussel byssus system and lays the groundwork for further research into the characterisation of this unique system. From a materials research point of view, this study investigated the effect of fibre mesh reinforcement on the QSI response of the LLDPE foam and compared them with fibre sheet reinforcement used in previous studies. However, several limitations remain in this research. For instance, the elastic recovery of the LLDPE foams was not analysed in this study. The manufacturing process and sample preparation might result in slight variations between samples. The effects of the relative sizes of the fibre mesh and indenter on the QSI behaviour of the fibre mesh reinforce foams remain unknown. The friction effect between the fixture and the samples remains unclear. Therefore, future work can focus on addressing these limitations and further experimenting with different types of foams or fibre meshes. Most importantly, from the biomimetic design perspective, future research should focus on replicating the unique structure of the foam core

with embedded fibres of the mussel byssus system. For example, advanced 3D printing technology can be used to achieve replication and help explore the mechanical reasons behind this unique structure.

6.5 Conclusion

This chapter shows a preliminary biomimetic example of the microstructure of the mussel byssus system. The carbon-fibre mesh reinforced LLDPE foams were inspired by the mussel plaque foam core with embedded thread fibres. The investigation into the quasi-static indentation (QSI) behaviour of carbon-fibre mesh reinforced LLDPE foams, highlights several critical findings:

1. **Influence of indenter nose shape**: The shape of the indenter nose significantly impacts the QSI behaviour of carbon-fibre mesh reinforced LLDPE foams. A flat-circular indenter exhibited the highest resistance due to a larger crushing contact area under solid support. Conversely, the conical indenter showed the least resistance and smallest crushing area post-initial perforation under solid support. Truncated and hemispherical indenters demonstrated intermediate resistance levels.

2. **Effect of support conditions**: Support conditions are critical in influencing the QSI behaviour of the foams. Under framed support, indentation resistance was markedly lower across all indenter types than solid support due to extensive bending and distributed damage. While solid support conditions can induce foam densification, leading to a rapid increase in indentation force.

3. **Impact of fibre mesh reinforcement**: Under framed support, fibre mesh reinforcement can effectively reduce sample bending and enhance indentation resistance, including maximum indentation force and absorbed energy. Increasing the number of fibre mesh layers can further improve the indentation resistance of LLDPE foams, particularly with hemi-spherical and conical indenters. However, altering the positions of single-layer fibre meshes had a limited effect on indentation resistance under framed support. In contrast, under solid support, the interaction between the indenter and the foam core was the main determinant of the QSI behaviour, while the fibre mesh had an insignificant effect on the QSI behaviour.

4. **Fiber mesh failure modes**: Under solid support, fibre breakage was observed in TOF samples and on the top surface of DOF samples. Under framed support, two failure modes were found when the foams were subjected to failure: fibre breakage and fibre pull-out. Fibre breakage predominantly occurred in TOF samples and the top surface of DOF samples, while fibre pull-out was observed in MIF, BOF, and the bottom surface of DOF samples. Fibre mesh failure modes were more significantly influenced by fibre mesh positioning than by indenter shape.

Given these findings, further exploration of the mechanical principles behind the formation of the unique mussel byssus system is warranted. These findings highlight the need for the precise replication of the microstructure of the mussel byssus system and further advanced mechanical studies.

Chapter 7

Conclusions and future work

7.1 Conclusions

Numerous studies have investigated the chemical compositions of the mussel byssus system and the development of mussel chemistry-inspired materials. However, the mechanics of the mussel byssus system and its components remain largely unexplored, with limited attention given to structural and mechanical biomimetic applications. Several research gaps are identified after extensively reviewing the literature on the structural and chemical composition, mechanical properties, and biomimetic products inspired by the mussel byssus system. For instance, the mechanical behaviours of each component of the mussel byssus system have not been clearly determined; the relationship between the unique microstructure of mussel plaques and their mechanical properties is not well understood; and the development of biomimetic materials based on the mechanics and microstructural composition of the mussel byssus system is limited. Based on these identified research gaps, this thesis aims to delve deeper into the mechanics of the mussel byssus system and explore the biomimetic potential based on its

mechanics and microstructure. The overarching conclusions of this thesis are drawn below from the studies presented in chapters 4 to 6.

7.1.1 Determining mechanical behaviours of the constituents of the mussel byssus system

This chapter aimed to investigate the microstructural compositions and determine the mechanical behaviours of each component of the mussel byssus system. It also discussed the potential relationship between microstructural compositions and mechanical behaviours.

Analytical and FE inverse methods were developed to determine the individual mechanical behaviours of the mussel plaque and proximal thread. The results of micro-tensile tests and optical tests were utilised as optimisation metrics within the inverse approaches. The findings demonstrate that these inverse methods successfully identify the mechanical behaviours of the proximal thread and the plaque, with the sum of squared residuals 0.0004 (N^2) and 0.01 (mm^2), respectively. The distal thread portion exhibits greater tensile strength but lower deformability than the proximal thread portion, which can be modelled using the Ogden material constitutive model. In contrast, the proximal portion and plaque are more deformable but have low strength, best described by the Neo-Hookean material model. The variations in tensile behaviour among these three components were found to be related to differences in their microstructure.

This chapter presents efficient inverse methods combined with simple micro-tensile and optical tests to determine the mechanical behaviours of individual components of the mussel byssus system. The results provide a foundation for a detailed study of the link between microstructure and

tensile properties, offering insights into biomimetic design based on the microstructural characteristics.

7.1.2 Unveiling the deformability of mussel plaque core: the role of pore distribution and hierarchical structure

This chapter explored the relationship between the pore distribution and hierarchical structure of the porous mussel plaque and its tensile behaviours, focusing on high deformability.

Intensive SEM analysis was conducted to obtain the microstructural characteristics of the mussel plaque. The results showed that the large-scale pore radius follows a lognormal distribution while the location follows a uniform distribution. The scaled large-scale pore parameters based on the SEM analysis and porosity measurements were employed to generate the 2D representative volume elements (RVEs) for the qualitative analysis. The phase field method, calibrated by experiments, was employed to analyse the effect of large-scale pore distribution and hierarchical structure on the failure mechanism and tensile properties of the porous RVEs, respectively. The results demonstrate that large-scale pore distribution can effectively affect the tensile properties of porous RVEs, including the strength, strain energy density and the final failure strain, but it is not the sole determining factor. While large-scale pore distribution primarily determines the failure modes of the porous RVEs, the hierarchical structure further enhances the final failure strain by reducing the stiffness of the RVEs. These findings indicate that both pore distribution and hierarchical structure could be the key factors contributing to the high deformability of mussel plaques.

This chapter provides a qualitative analysis of the relationship between the microstructure of mussel plaques and their mechanical properties and failure mechanisms. The results deepen our understanding of this relationship and offer insights into mimicking the unique structure of mussel plaques to design disordered porous structures with high deformability using minimal material.

7.1.3 A biomimetic application inspired by the mussel byssus system: the quasi-static indentation analysis of carbon-fibre mesh reinforced LLDPE foams

This chapter aimed to provide a preliminary biomimetic example of the microstructures of the mussel byssus system. Specifically, carbon-fibre mesh-reinforced LLDPE foams, inspired by the foam core of mussel plaque embedded with thread fibre, were manufactured for the quasi-static indentation (QSI) analysis to understand the effect of fibre mesh reinforcement.

A series of QSI tests were conducted on carbon-fibre mesh reinforced LLDPE foams with various indenter nose shapes, support conditions, and fibre mesh layer numbers and locations. The results find that both indenter nose shapes and support conditions can significantly affect the QSI behaviours of the samples. Meanwhile, the fibre mesh reinforcement can increase the indentation resistance of samples under framed support by reducing the foam bending while having an insignificant effect on LLDPE foams under solid support, where the foam core dominates the QSI behaviour. The location of the fibre mesh also had an insignificant effect on the QSI resistance of LLDPE foams. Additionally, the fibre mesh failure modes were found

to be related to its location under framed support, with the top layer experiencing fibre breakage and the bottom/middle layer experiencing fibre pull-out.

This chapter demonstrated an example of biomimetic design inspired by the microstructure of the mussel byssus system and built the foundation for future advanced biomimetic applications. Meanwhile, the impact of indenter nose shapes, support conditions, and the number and location of fibre mesh reinforcement on the QSI behaviour of LLDPE foams are investigated, providing insights for future carbon-fibre reinforcement design and biomimetic design based on the mussel byssus system.

7.2 Future work

The findings presented in this thesis deepen our understanding of the mechanics of the mussel byssus system and provide insights into its biomimetic design potentials. While significant features have been studied, several areas require more comprehensive investigation. Future research should explore the following subjects:

1. In Chapter 4, the three components of the mussel byssus system were assumed to be three individual materials; however, they are composite materials consisting of an outer cuticle and different inner cores. Future research could further determine the material properties of the individual cores and the cuticle layer. The hyperelastic material constitutive models (Ogden and Neo-Hookean models) were applied to describe the tensile behaviour of the mussel byssus system components. However, we did not conduct unloading tests to determine if they were real hyperelastic materials. Future research can focus on

analysing the dynamic response of the mussel byssus system. The failure mechanism of the mussel byssus system was not analysed in this research, and the detachment process of the system was largely simplified. Future studies can try to obtain the dynamic 3D detachment process of the mussel byssus system and apply it as the optimization metric to improve the accuracy of the inverse methods.

2. In Chapter 5, the effect of large-scale pore distribution and hierarchical structure of the porous core of mussel plaques on their mechanical behaviour was investigated, with a focus on high deformability. Extensive SEM analysis provided insights into the microstructure of mussel plaques and obtained its pore distribution parameters. However, the analysis was conducted based on 2D SEM images, and the SEM analysis is destructive, which might affect the pore distribution of mussel plaques. Future research should conduct less destructive 3D scans to achieve a more comprehensive understanding of the porous structure. The 2D porous RVEs applied in this study were only for qualitative analysis. The simplified pore distribution and hierarchical structure could affect the values of the distribution parameters. Future research can focus on accurately replicating the 3D porous structure of mussel plaque and analysing its mechanical behaviour. Obtaining the real material properties of the porous core in the future is also crucial to further investigate the impact of the microstructure. Additionally, the distribution parameters obtained from the SEM analysis were scaled from micrometres to millimetres to overcome the manufacturing limitation. Future research should try to investigate the microstructure's scalability effects. Meanwhile, using artificial intelligence (AI) or machine learning techniques in the future can help obtain more accurate statistical conclusions.

3. In Chapter 6, a preliminary biomimetic example inspired by the mussel plaque's foam core embedded with the mussel thread fibres was presented. The carbon-fibre mesh reinforcement LLDPE foams, where carbon-fibre mesh presenters the thread fibre and LLDPE foams present the plaque core, were manufactured as a unit. The quasi-static indentation (QSI) behaviour of the carbon-fibre mesh reinforcement LLDPE foams was analysed. From the biomimetic perspective, based on the findings within this research, future work can explore using more advanced technology like 3D printing to accurately replicate the high-strength fibre-embedded foams within the mussel byssus system. Then, we can analyse its mechanical behaviour, which would be more representative. From the material research perspective, future research can explore different methods, such as analytical or numerical methods, to present the QSI behaviour of carbon fibre-reinforced LLDPE foams. Analysing the elastic recovery of the LLDPE foams and the effect of the clamp fixture during the QSI tests are also essential in the future. Moreover, future research could investigate the effect of the relative sizes between the indenter nose, fibre mesh, and samples on QSI behaviours.

Bibliography

[1] Heather G Silverman and Francisco F Roberto. Understanding marine mussel adhesion. *Marine biotechnology*, 9:661–681, 2007.

[2] A. Hagenau, H. A. Scheidt, L. C. Serpell, D. Huster, and T. Scheibel. Structural analysis of proteinaceous components in byssal threads of the mussel mytilus galloprovincialis. *Macromolecular Bioscience*, 9:162–168, 2009.

[3] Sijia Li, Jingsi Chen, Jingyi Wang, and Hongbo Zeng. Anti-biofouling materials and surfaces based on mussel-inspired chemistry. *Materials Advances*, 2(7):2216–2230, 2021.

[4] J Herbert Waite and Matthew J Harrington. Following the thread: Mytilus mussel byssus as an inspired multi-functional biomaterial. *Canadian Journal of Chemistry*, 100(3):197–211, 2022.

[5] Bruce P Lee, Phillip B Messersmith, Jacob N Israelachvili, and J Herbert Waite. Mussel-inspired adhesives and coatings. *Annual review of materials research*, 41:99–132, 2011.

[6] Kenneth W Desmond, Nicholas A Zacchia, J Herbert Waite, and Megan T Valentine. Dynamics of mussel plaque detachment. *Soft matter*, 11(34):6832–6839, 2015.

[7] Qi Guo, Jingsi Chen, Jilei Wang, Hongbo Zeng, and Jing Yu. Recent

progress in synthesis and application of mussel-inspired adhesives. *Nanoscale*, 12(3):1307–1324, 2020.

[8] J Herbert Waite, Niels Holten Andersen, Scott Jewhurst, and Chengjun Sun. Mussel adhesion: finding the tricks worth mimicking. *The journal of adhesion*, 81(3-4):297–317, 2005.

[9] Yong Pang, Wei Sun, and Tao Liu. Quasi-static responses of marine mussel plaques detached from deformable wet substrates under directional tensions. 480(2290):20230465, 2024.

[10] Xiao-Xia Qin, Kathryn J Coyne, and J Herbert Waite. Tough tendons: mussel byssus has collagen with silk-like domains. *Journal of Biological Chemistry*, 272(51):32623–32627, 1997.

[11] Shiguo Li, Zhiqiang Xia, Yiyong Chen, Yangchun Gao, and Aibin Zhan. Byssus structure and protein composition in the highly invasive fouling mussel limnoperna fortunei. *Frontiers in Physiology*, 9:418, 2018.

[12] J Herbert Waite. Adhesion in byssally attached bivalves. *Biological Reviews*, 58(2):209–231, 1983.

[13] JE Smeathers and JFV Vincent. Mechanical properties of mussel byssus threads. *Journal of Molluscan Studies*, 45(2):219–230, 1979.

[14] Shanna L Brazee and Emily Carrington. Interspecific comparison of the mechanical properties of mussel byssus. *The Biological Bulletin*, 211(3):263–274, 2006.

[15] Trevor Pearce and Michael LaBarbera. A comparative study of the mechanical properties of mytilid byssal threads. *Journal of Experimental Biology*, 212(10):1442–1448, 2009.

[16] Emmanouela Filippidi, Daniel G DeMartini, Paula Malo de Molina, Eric W Danner, Juntae Kim, Matthew E Helgeson, J Herbert Waite, and Megan T Valentine. The microscopic network structure of mussel (mytilus) adhesive plaques. *Journal of The Royal Society Interface*, 12(113):20150827, 2015.

[17] Nadine R Martinez Rodriguez, Saurabh Das, Yair Kaufman, Jacob N Israelachvili, and J Herbert Waite. Interfacial ph during mussel adhesive plaque formation. *Biofouling*, 31(2):221–227, 2015.

[18] Niels Holten-Andersen, Thomas E Mates, Muhammet S Toprak, Galen D Stucky, Frank W Zok, and J Herbert Waite. Metals and the integrity of a biological coating: the cuticle of mussel byssus. *Langmuir*, 25(6):3323–3326, 2009.

[19] Stefan Zechel, Martin D Hager, Tobias Priemel, and Matthew J Harrington. Healing through histidine: Bioinspired pathways to self-healing polymers via imidazole–metal coordination. *Biomimetics*, 4(1):20, 2019.

[20] Q. Xu, M. Xu, C. K. Lin, Q. Zhen, R. Zhang, X. Dong, Z. Yida, S. Tian, Y. Tian, and Z. Xia. Metal coordination-mediated functional grading and self-healing in mussel byssus cuticle. *Advanced Science*, 6, 2019.

[21] Justin H Bernstein, Emmanouela Filippidi, J Herbert Waite, and Megan T Valentine. Effects of sea water ph on marine mussel plaque maturation. *Soft Matter*, 16(40):9339–9346, 2020.

[22] Dong Soo Hwang, Hongbo Zeng, Admir Masic, Matthew J Harrington, Jacob N Israelachvili, and J Herbert Waite. Protein-and metal-dependent interactions of a prominent protein in mussel adhesive plaques. *Journal of biological chemistry*, 285(33):25850–25858, 2010.

[23] Wei Wei, Jing Yu, Christopher Broomell, Jacob N Israelachvili, and J Herbert Waite. Hydrophobic enhancement of dopa-mediated adhesion in a mussel foot protein. *Journal of the American Chemical Society*, 135(1):377–383, 2013.

[24] Eugene Kim, Bin Dai, James B Qiao, Wenlu Li, John D Fortner, and Fuzhong Zhang. Microbially synthesized repeats of mussel foot protein display enhanced underwater adhesion. *ACS applied materials & interfaces*, 10(49):43003–43012, 2018.

[25] John Gosline, Margo Lillie, Emily Carrington, Paul Guerette, Christine Ortlepp, and Ken Savage. Elastic proteins: biological roles and mechanical properties. *Philosophical Transactions of the Royal Society of London. Series B: Biological Sciences*, 357(1418):121–132, 2002.

[26] Emily C Bell and John M Gosline. Mechanical design of mussel byssus: material yield enhances attachment strength. *Journal of Experimental Biology*, 199(4):1005–1017, 1996.

[27] Emily Carrington and John M Gosline. Mechanical design of mussell byssus: Load cycle and strain rate dependence. 2004.

[28] N Aldred, T Wills, DN Williams, and AS Clare. Tensile and dynamic mechanical analysis of the distal portion of mussel (mytilus edulis) byssal threads. *Journal of the Royal Society Interface*, 4(17):1159–1167, 2007.

[29] Z. Qin and M. J. Buehler. Impact tolerance in mussel thread networks by heterogeneous material distribution. *Nature Communications*, 4, 2013.

[30] Jeremy R Burkett, Jessica L Wojtas, Joshua L Cloud, and Jonathan J

Wilker. A method for measuring the adhesion strength of marine mussels. *The Journal of Adhesion*, 85(9):601–615, 2009.

[31] Hilary Ann Price. Seasonal variation in the strength of byssal attachment of the common mussel mytilus edulis l. *Journal of the Marine Biological Association of the United Kingdom*, 60(4):1035–1037, 1980.

[32] MY Ünlü and SW Fowler. Factors affecting the flux of arsenic through the mussel mytilus galloprovincialis. *Marine Biology*, 51:209–219, 1979.

[33] Kasandra-Zorica Ivanić, Zoran Tadić, and Mislav Ante Omazić. Biomimicry–an overview. *The holistic approach to environment*, 5(1):19–36, 2015.

[34] Fuyu Song, Jiahui Zhang, Jie Lu, Yi Cheng, Yehan Tao, Changyou Shao, and Haisong Wang. A mussel-inspired flexible chitosan-based bio-hydrogel as a tailored medical adhesive. *International Journal of Biological Macromolecules*, 189:183–193, 2021.

[35] Kai U Claussen, Reiner Giesa, Thomas Scheibel, and Hans-Werner Schmidt. Learning from nature: synthesis and characterization of longitudinal polymer gradient materials inspired by mussel byssus threads. *Macromolecular rapid communications*, 33(3):206–211, 2012.

[36] Marie Krogsgaard, Vicki Nue, and Henrik Birkedal. Mussel-inspired materials: self-healing through coordination chemistry. *Chemistry–A European Journal*, 22(3):844–857, 2016.

[37] Miriam Simmons. *Structure and Formation of Byssal Threads in Freshwater Zebra and Quagga Mussels (Dreissena Spp.)*. McGill University (Canada), 2021.

[38] Thomas P Bonner and Rebecca L Rockhill. Ultrastructure of the byssus of the zebra mussel (dreissena polymorpha, mollusca: Bivalvia). *Transactions of the American Microscopical Society*, pages 302–315, 1994.

[39] EE Vekhova. The byssal apparatus in the pacific mussel, mytilus trossulus (bivalvia, mytilidae), from the sea of japan. *Biology Bulletin*, 48(9):1443–1451, 2021.

[40] J. H. Waite. Mussel adhesion – essential footwork. *Journal of Experimental Biology*, 220:517–530, 2017.

[41] C. Liu, S. Li, J. Huang, Y. Liu, G. Jia, L. Xie, and R. Zhang. Extensible byssus of pinctada fucata: ca2+-stabilized nanocavities and a thrombospondin-1 protein. *Scientific Reports*, 5, 2015.

[42] C. Liu, L. Xie, and R. Zhang. Ca2+ mediates the self-assembly of the foot proteins of pinctada fucata from the nanoscale to the microscale. *Biomacromolecules*, 17:3347–3355, 2016.

[43] Marcela Areyano, Eric Valois, Ismael Sanchez Carvajal, Ivan Rajkovic, William R Wonderly, Attila Kossa, Robert M McMeeking, and J Herbert Waite. Viscoelastic analysis of mussel threads reveals energy dissipative mechanisms. *Journal of the Royal Society Interface*, 19(188):20210828, 2022.

[44] Daanish Aleem Qureshi, Stephen Goffredo, Yongtae Kim, Yulong Han, Ming Guo, Seunghwa Ryu, and Zhao Qin. Why mussel byssal plaques are tiny yet strong in attachment. *Matter*, 5(2):710–724, 2022.

[45] Michael A McCartney. Structure, function and parallel evolution of the bivalve byssus, with insights from proteomes and the zebra

mussel genome. *Philosophical Transactions of the Royal Society B*, 376(1825):20200155, 2021.

[46] E. Filippidi, T. R. Cristiani, C. D. Eisenbach, J. H. Waite, J. N. Israelachvili, B. K. Ahn, and M. T. Valentine. Toughening elastomers using mussel-inspired iron-catechol complexes. *Science*, 358:502–505, 2017.

[47] C. N. Z. Schmitt, A. Winter, L. Bertinetti, A. Mašić, P. Strauch, and M. J. Harrington. Mechanical homeostasis of a dopa-enriched biological coating from mussels in response to metal variation. *Journal of the Royal Society Interface*, 12:20150466, 2015.

[48] Z. Zhao, Y. Shan, H. Wang, H. Lu, X. Liu, B. Wang, and X. Song. Sustainable cement-free soil stabilization via a mussel mimicry, water-resistant hydrogel. *Chemistry of Materials*, 34:10443–10450, 2022.

[49] Jared M Lucas, Eleonora Vaccaro, and J Herbert Waite. A molecular, morphometric and mechanical comparison of the structural elements of byssus from mytilus edulis and mytilus galloprovincialis. *Journal of Experimental Biology*, 205(12):1807–1817, 2002.

[50] Christine V Benedict and J Herbert Waite. Location and analysis of byssal structural proteins of mytilus edulis. *Journal of morphology*, 189(2):171–181, 1986.

[51] ChengJun Sun and J Herbert Waite. Mapping chemical gradients within and along a fibrous structural tissue, mussel byssal threads. *Journal of Biological Chemistry*, 280(47):39332–39336, 2005.

[52] N. Holten-Andersen, M. J. Harrington, H. Birkedal, B. P. Lee, P. B. Messersmith, K. Y. C. Lee, and J. H. Waite. Ph-induced metal-ligand cross-links inspired by mussel yield self-healing polymer net-

works with near-covalent elastic moduli. *Proceedings of the National Academy of Sciences*, 108:2651–2655, 2011.

[53] M. J. Harrington, A. Mašić, N. Holten-Andersen, J. H. Waite, and P. Fratzl. Iron-clad fibers: a metal-based biological strategy for hard flexible coatings. *Science*, 328:216–220, 2010.

[54] C. Monnier, D. G. DeMartini, and J. H. Waite. Intertidal exposure favors the soft-studded armor of adaptive mussel coatings. *Nature Communications*, 9, 2018.

[55] J Herbert Waite, Xiao-Xia Qin, and Kathryn J Coyne. The peculiar collagens of mussel byssus. *Matrix biology*, 17(2):93–106, 1998.

[56] XIAOXIA Qin and J Herbert Waite. Exotic collagen gradients in the byssus of the mussel mytilus edulis. *Journal of Experimental Biology*, 198(3):633–644, 1995.

[57] Kathryn J Coyne, Xiao-Xia Qin, and J Herbert Waite. Extensible collagen in mussel byssus: a natural block copolymer. *Science*, 277(5333):1830–1832, 1997.

[58] HILARY ANN PRICE. Structure and formation of the byssus complex in mytilus (mollusca, bivalvia). *Journal of Molluscan studies*, 49(1):9–17, 1983.

[59] A. Reinecke, G. Brezesinski, and M. J. Harrington. Ph-responsive self-organization of metal-binding protein motifs from biomolecular junctions in mussel byssus. *Advanced Materials Interfaces*, 4, 2016.

[60] H. Zhao and J. H. Waite. Proteins in load-bearing junctions: the histidine-rich metal-binding protein of mussel byssus,. *Biochemistry*, 45:14223–14231, 2006.

[61] Tue Hassenkam, Thomas Gutsmann, Paul Hansma, Jason Sagert, and J Herbert Waite. Giant bent-core mesogens in the thread forming process of marine mussels. *Biomacromolecules*, 5(4):1351–1355, 2004.

[62] M. J. Harrington and J. H. Waite. Holdfast heroics: comparing the molecular and mechanical properties ofmytilus californianusbyssal threads. *Journal of Experimental Biology*, 210:4307–4318, 2007.

[63] Stefanie Krauss, Till Hartmut Metzger, Peter Fratzl, and Matthew James Harrington. Self-repair of a biological fiber guided by an ordered elastic framework. *Biomacromolecules*, 14(5):1520–1528, 2013.

[64] Chengjun Sun, Jared M Lucas, and J Herbert Waite. Collagen-binding matrix proteins from elastomeric extraorganismic byssal fibers. *Biomacromolecules*, 3(6):1240–1248, 2002.

[65] L. Li, H. Peng, Y. Du, H. Zheng, A. Yang, G. Lv, and H. Li. An antibacterial biomimetic adhesive with strong adhesion in both dry and underwater situations. *Journal of Materials Chemistry B*, 10:1063–1076, 2022.

[66] Menaka H Wilhelm, Emmanouela Filippidi, J Herbert Waite, and Megan T Valentine. Influence of multi-cycle loading on the structure and mechanics of marine mussel plaques. *Soft Matter*, 13(40):7381–7388, 2017.

[67] Arnold Tamarin, Pathicia Lewis, and Joan Askey. The structure and formation of the byssus attachment plaque in mytilus. *Journal of morphology*, 149(2):199–221, 1976.

[68] Christine V Benedict and J Herbert Waite. Composition and ul-

trastructure of the byssus of mytilus edulis. *Journal of morphology*, 189(3):261–270, 1986.

[69] Qi Lin, Delphine Gourdon, Chengjun Sun, Niels Holten-Andersen, Travers H Anderson, J Herbert Waite, and Jacob N Israelachvili. Adhesion mechanisms of the mussel foot proteins mfp-1 and mfp-3. *Proceedings of the National Academy of Sciences*, 104(10):3782–3786, 2007.

[70] Hongbo Zeng, Dong Soo Hwang, Jacob N Israelachvili, and J Herbert Waite. Strong reversible fe3+-mediated bridging between dopa-containing protein films in water. *Proceedings of the National Academy of Sciences*, 107(29):12850–12853, 2010.

[71] Russell J Stewart, Todd C Ransom, and Vladimir Hlady. Natural underwater adhesives. *Journal of Polymer Science Part B: Polymer Physics*, 49(11):757–771, 2011.

[72] Vladimir V Papov, Thomas V Diamond, Klaus Biemann, and J Herbert Waite. Hydroxyarginine-containing polyphenolic proteins in the adhesive plaques of the marine mussel mytilus edulis (∗). *Journal of Biological Chemistry*, 270(34):20183–20192, 1995.

[73] J Herbert Waite and Xiaoxia Qin. Polyphosphoprotein from the adhesive pads of mytilus edulis. *Biochemistry*, 40(9):2887–2893, 2001.

[74] Leszek M Rzepecki, Karolyn M Hansen, and J Herbert Waite. Characterization of a cystine-rich polyphenolic protein family from the blue mussel mytilus edulis l. *The Biological Bulletin*, 183(1):123–137, 1992.

[75] Daniel G DeMartini, John M Errico, Sebastian Sjoestroem, April Fenster, and J Herbert Waite. A cohort of new adhesive proteins

identified from transcriptomic analysis of mussel foot glands. *Journal of the Royal Society Interface*, 14(131):20170151, 2017.

[76] Chuan-li Qin, Qi-dong Pan, Qi Qi, Mei-hua Fan, Jing-jing Sun, Nan-nan Li, and Zhi Liao. In-depth proteomic analysis of the byssus from marine mussel mytilus coruscus. *Journal of proteomics*, 144:87–98, 2016.

[77] Koji Inoue, Yasuhiro Takeuchi, Daisuke Miki, and Satoshi Odo. Mussel adhesive plaque protein gene is a novel member of epidermal growth factor-like gene family (∗). *Journal of Biological Chemistry*, 270(12):6698–6701, 1995.

[78] Hua Zhao, Nicholas B Robertson, Scott A Jewhurst, and J Herbert Waite. Probing the adhesive footprints of mytilus californianus byssus. *Journal of Biological Chemistry*, 281(16):11090–11096, 2006.

[79] Qingye Lu, Eric Danner, J Herbert Waite, Jacob N Israelachvili, Hongbo Zeng, and Dong Soo Hwang. Adhesion of mussel foot proteins to different substrate surfaces. *Journal of The Royal Society Interface*, 10(79):20120759, 2013.

[80] Eric Valois, Razieh Mirshafian, and J Herbert Waite. Phase-dependent redox insulation in mussel adhesion. *Science advances*, 6(23):eaaz6486, 2020.

[81] Pegah Kord Forooshani and Bruce P Lee. Recent approaches in designing bioadhesive materials inspired by mussel adhesive protein. *Journal of Polymer Science Part A: Polymer Chemistry*, 55(1):9–33, 2017.

[82] Sungbaek Seo, Saurabh Das, Piotr J Zalicki, Razieh Mirshafian, Claus D Eisenbach, Jacob N Israelachvili, J Herbert Waite, and

B Kollbe Ahn. Microphase behavior and enhanced wet-cohesion of synthetic copolyampholytes inspired by a mussel foot protein. *Journal of the American Chemical Society*, 137(29):9214–9217, 2015.

[83] Dong Soo Hwang and J Herbert Waite. Three intrinsically unstructured mussel adhesive proteins, mfp-1, mfp-2, and mfp-3: Analysis by circular dichroism. *Protein Science*, 21(11):1689–1695, 2012.

[84] Wei Wei, Jing Yu, Matthew A Gebbie, Yerpeng Tan, Nadine R Martinez Rodriguez, Jacob N Israelachvili, and J Herbert Waite. Bridging adhesion of mussel-inspired peptides: Role of charge, chain length, and surface type. *Langmuir*, 31(3):1105–1112, 2015.

[85] Jing Yu, Wei Wei, Eric Danner, Rebekah K Ashley, Jacob N Israelachvili, and J Herbert Waite. Mussel protein adhesion depends on interprotein thiol-mediated redox modulation. *Nature chemical biology*, 7(9):588–590, 2011.

[86] Qiang Wei, Katharina Achazi, Hendrik Liebe, Andrea Schulz, Paul-Ludwig Michael Noeske, Ingo Grunwald, and Rainer Haag. Mussel-inspired dendritic polymers as universal multifunctional coatings. *Angewandte Chemie International Edition*, 53(43):11650–11655, 2014.

[87] Sascha CT Nicklisch, Jamie E Spahn, Hongjun Zhou, Cristina M Gruian, and J Herbert Waite. Redox capacity of an extracellular matrix protein associated with adhesion in mytilus californianus. *Biochemistry*, 55(13):2022–2030, 2016.

[88] JA Allen, M Cook, DJ Jackson, S Preston, and EM Worth. Observations on the rate of production and mechanical properties of the byssus threads of mytilus edulis l. *Journal of Molluscan Studies*, 42(2):279–289, 1976.

[89] Hilary Ann Price. Byssus thread strength in the mussel, mytilus edulis. *Journal of Zoology*, 194(2):245–255, 1981.

[90] Eleonora Vaccaro and J Herbert Waite. Yield and post-yield behavior of mussel byssal thread: a self-healing biomolecular material. *Biomacromolecules*, 2(3):906–911, 2001.

[91] J Herbert Waite, Eleonora Vaccaro, Chengjun Sun, and Jared M Lucas. Elastomeric gradients: a hedge against stress concentration in marine holdfasts? *Philosophical Transactions of the Royal Society of London. Series B: Biological Sciences*, 357(1418):143–153, 2002.

[92] Jose MF Babarro and Emily Carrington. Byssus secretion of mytilus galloprovincialis: effect of site at macro-and micro-geographical scales within ría de vigo (nw spain). *Marine Ecology Progress Series*, 435:125–140, 2011.

[93] Gretchen M Moeser and Emily Carrington. Seasonal variation in mussel byssal thread mechanics. *Journal of Experimental Biology*, 209(10):1996–2003, 2006.

[94] Yvette L Garner and Marian K Litvaitis. Effects of artificial epibionts on byssogenesis, attachment strength, and movement in two size classes of the blue mussel, mytilus edulis. *Invertebrate Biology*, 136(1):15–21, 2017.

[95] Xinguo Zhao, Shuge Sun, Wei Shi, Xuemei Sun, Yan Zhang, Lin Zhu, Qi Sui, Bin Xia, Keming Qu, Bijuan Chen, et al. Mussel byssal attachment weakened by anthropogenic noise. *Frontiers in Marine Science*, 8:821019, 2021.

[96] Chengjun Sun, Eleonora Vaccaro, and J Herbert Waite. Oxidative stress and the mechanical properties of naturally occurring chimeric

collagen-containing fibers. *Biophysical Journal*, 81(6):3590–3595, 2001.

[97] Matthew J Harrington, Himadri S Gupta, Peter Fratzl, and J Herbert Waite. Collagen insulated from tensile damage by domains that unfold reversibly: In situ x-ray investigation of mechanical yield and damage repair in the mussel byssus. *Journal of structural biology*, 167(1):47–54, 2009.

[98] Matthew J Harrington, Franziska Jehle, and Tobias Priemel. Mussel byssus structure-function and fabrication as inspiration for biotechnological production of advanced materials. *Biotechnology journal*, 13(12):1800133, 2018.

[99] Clemens NZ Schmitt, Yael Politi, Antje Reinecke, and Matthew J Harrington. Role of sacrificial protein–metal bond exchange in mussel byssal thread self-healing. *Biomacromolecules*, 16(9):2852–2861, 2015.

[100] Amanda Andersen, Yaqing Chen, and Henrik Birkedal. Bioinspired metal–polyphenol materials: Self-healing and beyond. *Biomimetics*, 4(2):30, 2019.

[101] Niels Holten-Andersen, Matthew J Harrington, Henrik Birkedal, Bruce P Lee, Phillip B Messersmith, Ka Yee C Lee, and J Herbert Waite. ph-induced metal-ligand cross-links inspired by mussel yield self-healing polymer networks with near-covalent elastic moduli. *Proceedings of the National Academy of Sciences*, 108(7):2651–2655, 2011.

[102] J Herbert Waiter. Reverse engineering of bioadhesion in marine mussels. *Annals of the New York Academy of Sciences*, 875(1):301–309, 1999.

[103] Emily C Bell and John M Gosline. Strategies for life in flow: tenacity, morphometry, and probability of dislodgment of two mytilus species. *Marine Ecology Progress Series*, 159:197–208, 1997.

[104] Wei-Yan Quan, Zhang Hu, Hua-Zhong Liu, Qian-Qian Ouyang, Dong-Ying Zhang, Si-Dong Li, Pu-Wang Li, and Zi-Ming Yang. Mussel-inspired catechol-functionalized hydrogels and their medical applications. *Molecules*, 24(14):2586, 2019.

[105] Eric W Danner, Yajing Kan, Malte U Hammer, Jacob N Israelachvili, and J Herbert Waite. Adhesion of mussel foot protein mefp-5 to mica: an underwater superglue. *Biochemistry*, 51(33):6511–6518, 2012.

[106] Sascha CT Nicklisch, Saurabh Das, Nadine R Martinez Rodriguez, J Herbert Waite, and Jacob N Israelachvili. Antioxidant efficacy and adhesion rescue by a recombinant mussel foot protein-6. *Biotechnology progress*, 29(6):1587–1593, 2013.

[107] Emily Carrington. Seasonal variation in the attachment strength of blue mussels: causes and consequences. *Limnology and Oceanography*, 47(6):1723–1733, 2002.

[108] Matthew N George and Emily Carrington. Environmental post-processing increases the adhesion strength of mussel byssus adhesive. *Biofouling*, 34(4):388–397, 2018.

[109] Haeshin Lee, Bruce P Lee, and Phillip B Messersmith. A reversible wet/dry adhesive inspired by mussels and geckos. *Nature*, 448(7151):338–341, 2007.

[110] Bruce P Lee, Ameya Narkar, and Randall Wilharm. Effect of metal ion type on the movement of hydrogel actuator based on catechol-

metal ion coordination chemistry. *Sensors and Actuators B: Chemical*, 227:248–254, 2016.

[111] Qiang Zhang, Gabit Nurumbetov, Alexandre Simula, Chongyu Zhu, Muxiu Li, Paul Wilson, Kristian Kempe, Bin Yang, Lei Tao, and David M Haddleton. Synthesis of well-defined catechol polymers for surface functionalization of magnetic nanoparticles. *Polymer Chemistry*, 7(45):7002–7010, 2016.

[112] Qiaochu Li, Devin G Barrett, Phillip B Messersmith, and Niels Holten-Andersen. Controlling hydrogel mechanics via bio-inspired polymer–nanoparticle bond dynamics. *ACS nano*, 10(1):1317–1324, 2016.

[113] Wei-Chen Huang, Faisal Ali, Jingsi Zhao, Kelsey Rhee, Chenchen Mou, and Christopher J Bettinger. Ultrasound-mediated self-healing hydrogels based on tunable metal–organic bonding. *Biomacromolecules*, 18(4):1162–1171, 2017.

[114] Yanhua Zhao, Yang Wu, Liang Wang, Manman Zhang, Xuan Chen, Minjie Liu, Jun Fan, Junqiu Liu, Feng Zhou, and Zuankai Wang. Bio-inspired reversible underwater adhesive. *Nature communications*, 8(1):2218, 2017.

[115] Marie Krogsgaard, Manja A Behrens, Jan Skov Pedersen, and Henrik Birkedal. Self-healing mussel-inspired multi-ph-responsive hydrogels. *Biomacromolecules*, 14(2):297–301, 2013.

[116] Thi-Ngoc Pham, Ching-Fang Su, Ching-Chia Huang, and Jeng-Shiung Jan. Biomimetic hydrogels based on l-dopa conjugated gelatin as ph-responsive drug carriers and antimicrobial agents. *Colloids and Surfaces B: Biointerfaces*, 196:111316, 2020.

[117] Robert Bogue. Recent developments in adhesive technology: a review. *Assembly Automation*, 31(3):207–211, 2011.

[118] Christian Heinzmann, Souleymane Coulibaly, Anita Roulin, Gina L Fiore, and Christoph Weder. Light-induced bonding and debonding with supramolecular adhesives. *ACS applied materials & interfaces*, 6(7):4713–4719, 2014.

[119] Michael T Northen, Christian Greiner, Eduard Arzt, and Kimberly L Turner. A gecko-inspired reversible adhesive. *Advanced Materials*, 20(20):3905–3909, 2008.

[120] Changjiang Fan, Jiayin Fu, Wenzhen Zhu, and Dong-An Wang. A mussel-inspired double-crosslinked tissue adhesive intended for internal medical use. *Acta biomaterialia*, 33:51–63, 2016.

[121] Ning Chen, Liming Qin, and Qinmin Pan. Mussel-inspired healing of a strong and stiff polymer. *Journal of Materials Chemistry A*, 6(15):6667–6674, 2018.

[122] Zijian Gao, Lijie Duan, Yongqi Yang, Wei Hu, and Guanghui Gao. Mussel-inspired tough hydrogels with self-repairing and tissue adhesion. *Applied Surface Science*, 427:74–82, 2018.

[123] Juan V Alegre-Requena, Marleen Häring, Raquel P Herrera, and David Díaz Díaz. Regulatory parameters of self-healing alginate hydrogel networks prepared via mussel-inspired dynamic chemistry. *New Journal of Chemistry*, 40(10):8493–8501, 2016.

[124] Jeongwook Lee, Kyeol Chang, Sunhye Kim, Vikas Gite, Hoeil Chung, and Daewon Sohn. Phase controllable hyaluronic acid hydrogel with iron (iii) ion–catechol induced dual cross-linking by utilizing the gap of gelation kinetics. *Macromolecules*, 49(19):7450–7459, 2016.

[125] Si Yu Zheng, Hongyao Ding, Jin Qian, Jun Yin, Zi Liang Wu, Yihu Song, and Qiang Zheng. Metal-coordination complexes mediated physical hydrogels with high toughness, stick–slip tearing behavior, and good processability. *Macromolecules*, 49(24):9637–9646, 2016.

[126] Miroslav Mrlik, Mário Špírek, Jassim Al-Khori, Ali Abdulrahman Ahmad, Jaroslav Mosnaček, Mariam AlAli AlMaadeed, and Peter Kasak. Mussel-mimicking sulfobetaine-based copolymer with metal tunable gelation, self-healing and antibacterial capability. *Arabian Journal of Chemistry*, 13(1):193–204, 2020.

[127] Chaehoon Kim, Hirotaka Ejima, and Naoko Yoshie. Non-swellable self-healing polymer with long-term stability under seawater. *RSC advances*, 7(31):19288–19295, 2017.

[128] Aleksander Cholewinski, Fut Kuo Yang, and Boxin Zhao. Algae–mussel-inspired hydrogel composite glue for underwater bonding. *Materials horizons*, 6(2):285–293, 2019.

[129] Haeshin Lee, Shara M Dellatore, William M Miller, and Phillip B Messersmith. Mussel-inspired surface chemistry for multifunctional coatings. *science*, 318(5849):426–430, 2007.

[130] Michaël W Kulka, Ievgen S Donskyi, Nina Wurzler, Dirk Salz, Özlem Özcan, Wolfgang ES Unger, and Rainer Haag. Mussel-inspired multivalent linear polyglycerol coatings outperform monovalent polyethylene glycol coatings in antifouling surface properties. *ACS Applied Bio Materials*, 2(12):5749–5759, 2019.

[131] Yeonwoo Jeong, Jun Hyung Ryu, Yoon Kwon Nam, Seung Pyo Gong, and Sung Min Kang. Enhanced adhesion of fish ovarian germline stem cells on solid surfaces by mussel-inspired polymer coating. *Marine Drugs*, 17(1):11, 2018.

[132] Zhen-Xing Wang, Cher-Hon Lau, Nai-Qing Zhang, Yong-Ping Bai, and Lu Shao. Mussel-inspired tailoring of membrane wettability for harsh water treatment. *Journal of Materials Chemistry A*, 3(6):2650–2657, 2015.

[133] Noy Cohen, J Herbert Waite, Robert M McMeeking, and Megan T Valentine. Force distribution and multiscale mechanics in the mussel byssus. *Philosophical Transactions of the Royal Society B*, 374(1784):20190202, 2019.

[134] Ahmed Ghareeb and Ahmed Elbanna. On the role of the plaque porous structure in mussel adhesion: implications for adhesion control using bulk patterning. *Journal of Applied Mechanics*, 85(12):121003, 2018.

[135] Pablo V Perepelizin and Demetrio Boltovskoy. Thermal tolerance of limnoperna fortunei to gradual temperature increase and its applications for biofouling control in industrial and power plants. *Biofouling*, 27(6):667–674, 2011.

[136] Jon D Witman and Thomas H Suchanek. Mussels in flow: drag and dislodgement by epizoans. *Marine Ecology Progress Series*, 16(3):259–268, 1984.

[137] Yiran Li and Yi Cao. The molecular mechanisms underlying mussel adhesion. *Nanoscale Advances*, 1(11):4246–4257, 2019.

[138] DJ Crisp, G Walker, GA Young, and AB Yule. Adhesion and substrate choice in mussels and barnacles. *Journal of Colloid and Interface Science*, 104(1):40–50, 1985.

[139] N Holten-Andersen and JH Waite. Mussel-designed protective coat-

ings for compliant substrates. *Journal of dental research*, 87(8):701–709, 2008.

[140] Matthew J Harrington and J Herbert Waite. Holdfast heroics: comparing the molecular and mechanical properties of mytilus californianus byssal threads. *Journal of Experimental Biology*, 210(24):4307–4318, 2007.

[141] Quan Xu, Meng Xu, Chun-Yu Lin, Qiang Zhao, Rui Zhang, Xiaoxiao Dong, Yida Zhang, Shouceng Tian, Yu Tian, and Zhenhai Xia. Metal coordination-mediated functional grading and self-healing in mussel byssus cuticle. *Advanced Science*, 6(23):1902043, 2019.

[142] Yong Pang, Wei Sun, and Tao Liu. Quasi-static responses of marine mussel plaques detached from deformable wet substrates under directional tensions. In *Proceedings A*, volume 480, page 20230465. The Royal Society, 2024.

[143] MATLAB User's Guide. The mathworks. *Inc., Natick, MA*, 5(333):4, 1998.

[144] Raymond William Ogden. Large deformation isotropic elasticity–on the correlation of theory and experiment for incompressible rubberlike solids. *Proceedings of the Royal Society of London. A. Mathematical and Physical Sciences*, 326(1567):565–584, 1972.

[145] Ronald S Rivlin. Large elastic deformations of isotropic materials iv. further developments of the general theory. *Philosophical transactions of the royal society of London. Series A, Mathematical and physical sciences*, 241(835):379–397, 1948.

[146] D. S. Schnur and Nicholas Zabaras. An inverse method for determining elastic material properties and a material interface. *International*

Journal for Numerical Methods in Engineering, 33(10):2039–2057, 1992.

[147] Wei Sun, Zhufeng Yue, Zhixun Wen, and Ming Li. An overview on material parameter inverse and its application to miniaturized testing at elevated temperature. *Journal of Materials Research and Technology*, 2022.

[148] Jia Wang and Thomas Scheibel. Recombinant production of mussel byssus inspired proteins. *Biotechnology Journal*, 13(12):1800146, 2018.

[149] Michael H Suhre, Melanie Gertz, Clemens Steegborn, and Thomas Scheibel. Structural and functional features of a collagen-binding matrix protein from the mussel byssus. *Nature communications*, 5(1):3392, 2014.

[150] Adrian V Golser and Thomas Scheibel. Routes towards novel collagen-like biomaterials. *Fibers*, 6(2):21, 2018.

[151] N Aldred, LK Ista, ME Callow, JA Callow, GP Lopez, and AS Clare. Mussel (mytilus edulis) byssus deposition in response to variations in surface wettability. *Journal of the Royal Society Interface*, 3(6):37–43, 2006.

[152] Nandika Bandara, Hongbo Zeng, and Jianping Wu. Marine mussel adhesion: biochemistry, mechanisms, and biomimetics. *Journal of adhesion science and technology*, 27(18-19):2139–2162, 2013.

[153] Yulan Lyu, Yong Pang, Tao Liu, and Wei Sun. Determining hyperelastic properties of the constituents of the mussel byssus system. *Soft Matter*, 2024.

[154] Younghoon Kwon, Justin H Bernstein, Noy Cohen, and Megan T Valentine. On-demand manufacturing capabilities of mussels enable robust adhesion to geometrically complex surfaces. *ACS Biomaterials Science & Engineering*, 7(11):5099–5106, 2021.

[155] Abaqus Scripting User's Manual. Abaqus 6.11. *http://130.149*, 89(2080):v6, 2012.

[156] Yousef Navidtehrani, Covadonga Betegón, and Emilio Martínez-Pañeda. A simple and robust abaqus implementation of the phase field fracture method. *Applications in Engineering Science*, 6:100050, 2021.

[157] Yanchu Zhang, Kunhao Yu, Kyung Hoon Lee, Ketian Li, Haixu Du, and Qiming Wang. Mechanics of stretchy elastomer lattices. *Journal of the Mechanics and Physics of Solids*, 159:104782, 2022.

[158] Tingyao Li, Yanhui Jiang, Kunhao Yu, and Qiming Wang. Stretchable 3d lattice conductors. *Soft Matter*, 13(42):7731–7739, 2017.

[159] Akash Singh Bhuwal, Yong Pang, Ian Ashcroft, Wei Sun, and Tao Liu. Discovery of quasi-disordered truss metamaterials inspired by natural cellular materials. *Journal of the Mechanics and Physics of Solids*, 175:105294, 2023.

[160] AS Bhuwal, Y Pang, T Liu, I Ashcroft, and W Sun. Data-driven design of high ductile metamaterials under uniaxial tension. In *Current Perspectives and New Directions in Mechanics, Modelling and Design of Structural Systems*, pages 333–338. CRC Press, 2022.

[161] Pascal J Loew, Bernhard Peters, and Lars AA Beex. Rate-dependent phase-field damage modeling of rubber and its experimental param-

eter identification. *Journal of the Mechanics and Physics of Solids*, 127:266–294, 2019.

[162] Javier Bonet and Richard D Wood. *Nonlinear continuum mechanics for finite element analysis*. Cambridge university press, 1997.

[163] WF Pfeffer. The divergence theorem. *Transactions of the American Mathematical Society*, 295(2):665–685, 1986.

[164] Christian Miehe, Martina Hofacker, and Fabian Welschinger. A phase field model for rate-independent crack propagation: Robust algorithmic implementation based on operator splits. *Computer Methods in Applied Mechanics and Engineering*, 199(45-48):2765–2778, 2010.

[165] Stratasys Object260. Connex3 objet260 3d printer for multi-color multi-material models. https://www.stratasys.com/3d-printers/objet260-connex3. [Online; accessed 26-July-2024].

[166] David Roucou, Julie Diani, Mathias Brieu, and Armel Mbiakop-Ngassa. Critical strain energy release rate for rubbers: single edge notch tension versus pure shear tests. *International Journal of Fracture*, 216:31–39, 2019.

[167] Ronald S Rivlin and A Gr Thomas. Rupture of rubber. i. characteristic energy for tearing. *Journal of polymer science*, 10(3):291–318, 1953.

[168] Yong Pang, Suxia Huang, Hezong Li, Tao Liu, and Wei Sun. Elastic–plastic strain conversion of a thin-plate miniaturized tensile test based on crosshead measurement via an analytical method. *Theor. Appl. Fract. Mech.*, page 104532, 2024.

[169] Yong Pang, Bernard K Chen, Siu Fung Yu, and Siva N Lingamanaik.

Enhanced laser speckle optical sensor for in situ strain sensing and structural health monitoring. *Optics Letters*, 45(8):2331–2334, 2020.

[170] Yong Pang, Bernard K Chen, Wencheng Liu, Siu Fung Yu, and Siva N Lingamanaik. Development of a non-contact and non-destructive laser speckle imaging system for remote sensing of anisotropic deformation around fastener holes. *NDT & E International*, 111:102219, 2020.

[171] David A Freedman. *Statistical models: theory and practice*. cambridge university press, 2009.

[172] Jay L Devore. Probability and statistics. *Pacific Grove: Brooks/Cole*, 2000.

[173] Nico JD Nagelkerke et al. A note on a general definition of the coefficient of determination. *biometrika*, 78(3):691–692, 1991.

[174] Nikola Bosnjak and Meredith N Silberstein. Pathways to tough yet soft materials. *Science*, 374(6564):150–151, 2021.

[175] Anchana Wongsto and Shuguang Li. Micromechanical fe analysis of ud fibre-reinforced composites with fibres distributed at random over the transverse cross-section. *Composites Part A: Applied Science and Manufacturing*, 36(9):1246–1266, 2005.

[176] Shuguang Li and Elena Sitnikova. *Representative volume elements and unit cells: concepts, theory, applications and implementation*. Woodhead Publishing, 2019.

[177] Eli D Sone. Interfacial phenomena in marine and freshwater mussel adhesion. *Biological adhesives*, pages 129–151, 2016.

[178] Haeshin Lee, Norbert F Scherer, and Phillip B Messersmith. Single-molecule mechanics of mussel adhesion. *Proceedings of the National Academy of Sciences*, 103(35):12999–13003, 2006.

[179] EA Flores-Johnson and QM Li. Indentation into polymeric foams. *International Journal of Solids and Structures*, 47(16):1987–1995, 2010.

[180] EA Flores-Johnson and QM Li. Experimental study of the indentation of sandwich panels with carbon fibre-reinforced polymer face sheets and polymeric foam core. *Composites Part B: Engineering*, 42(5):1212–1219, 2011.

[181] Giancarlo Caprino, Massimo Durante, Claudio Leone, and Valentina Lopresto. The effect of shear on the local indentation and failure of sandwich beams with polymeric foam core loaded in flexure. *Composites Part B: Engineering*, 71:45–51, 2015.

[182] AM Boyce, HC Tankasala, and NA Fleck. Indentation of a layer on foam substrate. *International Journal of Mechanical Sciences*, 150:379–392, 2019.

[183] Stephanie G Nunes, Luís Guilherme G Reichwald, Wanderley FA Júnior, Andrea Manes, Sandro C Amico, et al. Quasi-static indentation and low-velocity impact response of aramid/epoxy composites. *4th Brazilian Conferece o Composite Materials*, pages 323–329, 2018.

[184] Seyed Ahmad Taghizadeh, Mohsen Naghdinasab, Hamidreza Madadi, and Amin Farrokhabadi. Investigation of novel multi-layer sandwich panels under quasi-static indentation loading using experimental and numerical analyses. *Thin-Walled Structures*, 160:107326, 2021.

[185] Milad Saeedifar and Hossein Hosseini Toudeshky. The effect of interlaminar and intralaminar damage mechanisms on the quasi-static indentation strength of composite laminates. *Applied Composite Materials*, 30(3):871–886, 2023.

[186] Alan T Nettles and Michael J Douglas. A comparison of quasi-static indentation to low-velocity impact. Technical report, 2000.

[187] Ashish Singh Pareta, PK Singh, Arnab Sarkar, and SK Panda. Quasi-static indentation damage mechanics of pu foam core reinforced with fly ash particulate. *Journal of Cellular Plastics*, 59(1):47–63, 2023.

[188] M Garrido, R Teixeira, JR Correia, and LS Sutherland. Quasi-static indentation and impact in glass-fibre reinforced polymer sandwich panels for civil and ocean engineering applications. *Journal of Sandwich Structures & Materials*, 23(1):194–221, 2021.

[189] Houcine Zniker, Bennaceur Ouaki, Said Bouzakraoui, Mohamed Ebn-Touhami, and Hicham Mezouara. Energy absorption and damage characterization of gfrp laminated and pvc-foam sandwich composites under repeated impacts with reduced energies and quasi-static indentation. *Case studies in construction materials*, 16:e00844, 2022.

[190] Fatih Balıkoğlu, Tayfur Kerem Demircioğlu, Mehmet Özer, and Ali Işıktaş. Investigation on the mechanical properties of resin pin-reinforced marine sandwich composite structures under quasi-static indentation load. *Niğde Ömer Halisdemir Üniversitesi Mühendislik Bilimleri Dergisi*, 13(2):690–696, 2024.

[191] Muhammad Aqil Alimin Mohd Ridzuan, Azrin Hani Abdul Rashid, Nurul Zakiah Zamri Tan, and Asyran Muhammad Azman. Numerical simulation of cross-ply r-pet laminated composites subjected to

quasi-static indentation test. *Progress in Engineering Application and Technology*, 3(1):769–779, 2022.

[192] Alok Kumar, Chinmaya Kumar Sahoo, and A Arockiarajan. Study of damage behavior and repair effectiveness of patch repaired carbon fiber laminate under quasi-static indentation loading. *Defence Technology*, 34:29–41, 2024.

[193] Kui Wang, Wanying Zhu, Shixian Li, Yong Peng, and Said Ahzi. Investigations of quasi-static indentation properties of 3d printed polyamide/continuous kevlar/continuous carbon fiber composites. *Journal of Applied Polymer Science*, 139(32):e52758, 2022.

[194] Wanying Zhu, Shixian Li, Yong Peng, Kui Wang, and Said Ahzi. Effect of continuous fiber orientations on quasi-static indentation properties in 3d printed hybrid continuous carbon/kevlar fiber reinforced composites. *Polymers for Advanced Technologies*, 34(5):1565–1574, 2023.

[195] Pravin P Patil and Manish Kumar Lila. The tension and quasi-static indentation properties of coir/glass fibre reinforced hybrid composites. *Webology*, 18(5):2856–2861, 2021.

[196] Ilya Izyan Shahrul Azhar, Aidah Jumahat, Noor Leha Abdul Rahman, Ramzi Khiari, and Muhammad Afnan Jamal Abd Nasir. Maximum quasi-static indentation stress analysis of flax/epoxy and glass/epoxy polymer composites. *International Journal of Integrated Engineering*, 14(9):1–7, 2022.

[197] Norman Osa-Uwagboe, Amadi Gabriel Udu, Vadim V Silberschmidt, Konstantinos P Baxevanakis, and Emrah Demirci. Damage assessment of glass-fibre-reinforced plastic structures under quasi-static indentation with acoustic emission. *Materials*, 16(14):5036, 2023.

[198] Muthukumaran Gunasegeran, Maiarutselvan Vasudevan, Manoharan Ramamoorthy, Anandababu Arumugam, et al. Investigation of quasi-static indentation on sandwich structure with gfrp face sheets and pla bio-inspired core: Numerical and experimental study. *Thin-Walled Structures*, 184:110501, 2023.

[199] Shunze Cao, Tao Liu, Arthur Jones, and Walid Tizani. Particle reinforced thermoplastic foams under quasi-static compression. *Mechanics of Materials*, 136:103081, 2019.

[200] ASTM International. ASTM C365/C365M-16: Standard Test Method for Flatwise Compressive Properties of Sandwich Cores, 2016.

[201] Mapei. Mapegrid c 170, 2024. Accessed: 2024-07-29.

[202] Ummu Raihanah Hashim, Aidah Jumahat, and Muhammad Fashan Md Ghazali. Quasi-static indentation properties of aluminium foam-frp sandwich panel. *Int. J. Eng. Technol*, 7(3), 2018.

[203] Martin B Wilk and Ram Gnanadesikan. Probability plotting methods for the analysis for the analysis of data. *Biometrika*, 55(1):1–17, 1968.

Appendices

Appendix A

Table A.1: Publication(s) contribution

Thesis Chapter	Publication Title	Status	% of student contribution	Co-author name(s) and % of Co-author's contribution
Chapter 4	Determining hyperelastic properties of the constituents of the mussel byssus system	Published	70%	Y.P.(10%), W.S.(10%), T.L.(10%)
Chapter 5	Unveiling the deformability of mussel plaque core: the role of pore distribution and hierarchical structure	Published	60%	M.T.(10%), Y.P. (10%), W.S.(5%), S.L.(5%), T.L.(10%)
Chapter 6	Quasi-static indentation analysis for carbon-fibre mesh reinforced LLDPE foams inspired by mussel plaques	To be submitted	75%	Y.P.(5%), S.L.(5%), W.S.(5%), T.L.(10%)

Appendix B

AWERB Cover Form (non-licensed study pro-forma)

Application to use animals in a non-licensed study in the UK

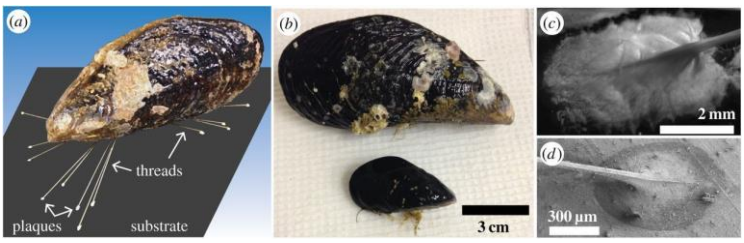
Name of applicant	Miss Yulan Lyu, Mr Tom Mazin, Dr Yong Pang, & Dr Tao Liu
Title of study	Mechanics and biomimicking of marine mussel plaques
School	Faculty of Engineering
Study location	Civil Engineering Small Structure Lab Room L2-A60

The Animal Welfare & Ethical Review Body (AWERB) exists to ensure that the use of all animals at the University of Nottingham is carefully considered and justified and that proper account is taken of all possibilities for reduction, refinement, and replacement (the 3Rs). To enable this, requests to use animals in studies where Home Office licence authority is not required, must be submitted to AWERB and the required information provided below. The completed form should be submitted to AWERB via bsu@nottingham.ac.uk. When approved, an approval reference number will be provided to the applicant which must be used if ordering animals for use in the non-licensed study.

The information you submit below allows AWERB to fulfil its role in safeguarding the University by providing it with oversight of all animal studies being undertaken by UK-based University staff. Importantly, this process also safeguards you from potential prosecution under the Animal Welfare Act 2006 by verifying that the proposed studies do not require Home Office license authority. Please provide information in non-technical language accessible to the lay members of the AWERB.

Study details

Key words (max 5)	Mussel thread/plaque, bio-inspired composites	
Expected duration of the study	3 years	
Species and expected number of animals to be used in total	marine mussel, approximately 5 kg	
Purpose of the study *Indicate 'Yes' against each category that applies.*	Basic research	*Yes*
	Translational and applied research	
	Regulatory use and routine production	
	Protection of the natural environment in the interests of the health or welfare of humans or animals	
	Preservation of species	
	Higher education or training	
	Forensic enquiries	
Scientific background *Briefly summarise the current position in this research area that justifies why this work is being done (information given here should relate only to this study).*	Marine mussels (Mytilus) such as Mytilus californianus anchor themselves to wet surfaces in hostile, intertidal zones such as rocks, bio-fouled, salt-encrusted and corroded surfaces via collagen-rich threads ending in adhesive pads, the plaques. Mussel plaques can achieve strong adhesion on a wet surface in a matter of minutes while immersed in high salt and basic pH	

	conditions imposed by seawater. The plaque core exhibits a cellular structure, consisting of a disordered, foamy network of pores at the length scales ranging from Nanometres to Micrometres, and reinforced by collagen fibre bundles. The cuticle layer exhibits a granular composite structure. The plaque core and the cuticle layer work in a cooperative way to achieve good load bearing capacity and high ductility under tension and shear. We aim to develop principles to design high performance, mussel plaque inspired multifunctional composite material systems.
Objective of study *State succinctly the primary objective or research question or hypothesis that will be addressed in this study.*	This is an interdisciplinary project funded through Leverhulme Trust. The proposal aims to (1) establish the mechanistic understanding on how the stiffness and the surface texture pattern of an underlying substratum influence the adhesive structure and adhesion behaviour of a mussel plaque. (2) Based on the understanding, the principles to develop mussel plaque inspired multifunctional composite material systems will be established.
What will happen to the animals?	The project only focuses on the thread-plaque system generated by mussels. The mussels will be looked after with great care as we want mussels to generate the thread-plaque systems. **<u>Collection, breeding and processing of mussels</u>** • The mussel type is blue mussel, also known as the common mussel. It is edible and is not biologically or chemically harmful to humans. (https://en.wikipedia.org/wiki/Blue_mussel) • The mussel will be shipped by the mussel supplier. • Keep mussels and glass slides tied together with rubber bands in water tank. The flowing seawater temperature in the water tank is typically 12-15˚C. • The mussel-attached plates are placed and maintained in the water tank for 1–4 days until the mussel plaques grow and stick to the glass slides. • The threads that connected the plaques to the mussel are cut, as close to the mussel body as possible. The mussels themselves will not be harmed by this action and can be returned to the tank after cutting for further studies. On average, each mussel produced 1-3 useful plaques per day. • At the end of the experiment, the mussels will be returned to the supplier or released back into the sea. 

What are the potential benefits likely to derive from this study? *Explain how this study will help advance current knowledge or meet a clinical need (this should relate to information provided in the 'Scientific background').* *Please include a description of the primary data outputs.*	We aim to develop mussel plaque inspired composite material systems to tackle engineering challenges • The novel, mussel plaque inspired approaches for joining dissimilar engineering materials will have been established via mimicking the adhesive structures of a mussel plaque formed on different substratum conditions. • The understanding on the unique load bearing behaviour of a plaque core under the effects of the stiffness and the surface texture pattern of the underlying substratum will have been established. The principles to design the high-performance composite materials with high tensile/shear strength and high ductility will have been established inspired by the complex material system of a plaque core.
What will happen to the animals at the end of the study? *If the animals are to be killed please state the ASPA schedule 1 method of humane killing and confirmation that will be used (see Appendix D of the Guidance on the Operation of ASPA) or provide justification for an alternative method.*	At the end of the experiment, the mussels will be returned to the suppliers or released back into the sea.
Housing & care *Please confirm that animals will be housed and cared for according to the ASPA Code of Practice or provide details and justification for alternative housing and care standards (e.g. relevant DEFRA guides). If working with wild animals please see the Home Office Advice Note on using animals taken from the wild.*	We accept advice from mussel suppliers and marine biologists from Plymouth Marine Laboratory (PML) to look after mussels. • Water tank, tank cooler, thermometer, and salimeter will be used to guarantee the seawater in the lab is consistent to the natural condition. Seawater will be replaced every other day • A large water tank with dimension of 1m X 1m X 2.5m will be used to ensure that each mussel has sufficient freedom of movement. • Shellfish diet (ShellfishDiet1800) extracted from the natural seawater will be provided, which ensure sufficient food for mussel health. 

Application of the 3Rs

Replacement *State why you need to use animals and why you cannot use non-animal alternatives.*	The mussel thread/plaque systems can only be generated by Mussels. Mussel thread/plaque systems is of unique structures in nature and has never been found in other man-made system; therefore, there is no non-animal alternatives.

Reduction *Explain how you will ensure the most appropriate numbers of animals are used (e.g. the method of statistical analysis and group sizes required).*	The marine mussel will produce thread every day; therefore, we will reuse the mussel in the experiments to minimise the use of marine mussel.
Refinement *Explain the choice of species and why the animal model(s) you will use are the most refined, having regard to the objectives. Explain the general measures you will take to minimise welfare costs (harms) to the animals.*	• Blue mussels will be used in the experiments since this species has a strong adaptive capacity to the environment. • We use water tank, tank cooler, thermometer, and salimeter to ensure consistence between natural seawater condition and laboratory seawater condition. Therefore, potential harms to the mussel will eliminated. • Shellfish diet extracted from the natural seawater will be provided, which ensure sufficient food for mussel health. • We have regular meetings with expert mussel suppliers and marine biologists from PML to seek advice to look after mussels.

To be signed by the head of the research group

a) I confirm that the procedures to be conducted will not result in any animal experiencing pain, suffering, distress, or lasting harm, and are therefore not regulated under ASPA.

b) Humane killing (if applicable) will be in accordance with Schedule 1 and only conducted by competent individuals named on the University of Nottingham central register.

c) I will act at all times in a manner consistent with the principles of the 3Rs.

d) I will ensure that the conduct of those undertaking this programme of work will be in accordance with the University Code of Research Conduct and Research Ethics.

Name: Mike Johnson for Nick Warrior

Signature:

Date: 26/7/2021

Committee use only

Comments by NACWO:
This looks to be a very interesting project. I am happy that the processes have been thought through and the mussels will be returned following the experiment. Happy for this experiment to go ahead. *M. Trussell 30/07/21*
Comments by NVS:
n/a
Comments by primary reader:
Many thanks for making AWERB aware of this project and taking the time to complete the Cover Form. I am satisfied with the justification for animal use but could an approximate numbers of mussels per month (or over the lifetime of the project) be provided please? Many thanks. I presume PML = Plymouth Marine Laboratory? I've added this the first time the acronym is used. *Ian Devonshire 9/8/21* <u>APPLICANT RESPONSE</u> We will only have mussel related experiments during 50% of the lifetime of the project. The water tank we use can accommodate 10-20 mussels. Therefore, we will maintain the number of mussels in the water tank during the period. Thank you for your response; happy to now approve the Cover Form. *Ian Devonshire 9/8/21*
Comments by lay person (if applicable):
n/a

Committee decision:	Approved
Approval reference no:	251
Date communicated to applicant:	9/8/21

Appendix C

C.1 Details on mussel samples preparation

Details of how the mussel samples were cultured in the laboratory have been described. Fig. C.1a shows the water tank used to farm marine mussels in the lab, which includes a glass water tank, a chiller, a water filter system, two water pumps and one airline with tubing. The PH value of artificial seawater is 8.5, as shown in Fig. C.1b. After the mussels were picked up from the Hunstanton mussel farm, they were placed on acrylic substrates, one substrate per mussel, and then secured with rubber rings to prevent them from moving (Fig. C.1c). After the generated byssus systems have adhered to the substrates, carefully cut them off from the mussels' bodies for the following mechanical tests and SEM imaging.

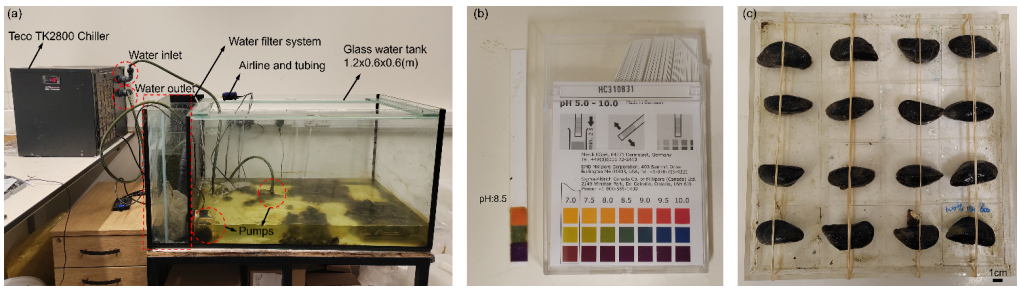


Figure C.1: (a) The water tank for mussels, (b) the seawater PH=8.5, (c) rubber bands were used to fix uniformly sized marine mussels to the substrate.

Appendix D

D.1 The pore distribution analysis of mussel plaque SEM photos

Figures D.1 and D.2 were analysed with additional SEM images to investigate further the pore distribution of large-scale pores within mussel plaques. It can be concluded that the large-scale pore radius still follows a lognormal distribution. The porosity (ν_l), normalised mean radius ($\bar{\mu}_p^*$) and normalised standard deviation of radius ($\bar{s}_p^*$) for those SEM images are shown in Tables D.1 and D.2, respectively.

Table D.1: Porosity (υ_l), normalised mean radius ($\bar{\mu}_p^*$) and normalised standard deviation of radius ($\bar{s}_p^*$) of the simplified large-scale pores within the SEM images of the same mussel.

	Porosity (υ_l)	$\bar{\mu}_p^*$	$\bar{s}_p^*$
Slice 1	33%	0.043	0.012
Slice 2	28%	0.039	0.008
Slice 3	37%	0.041	0.012

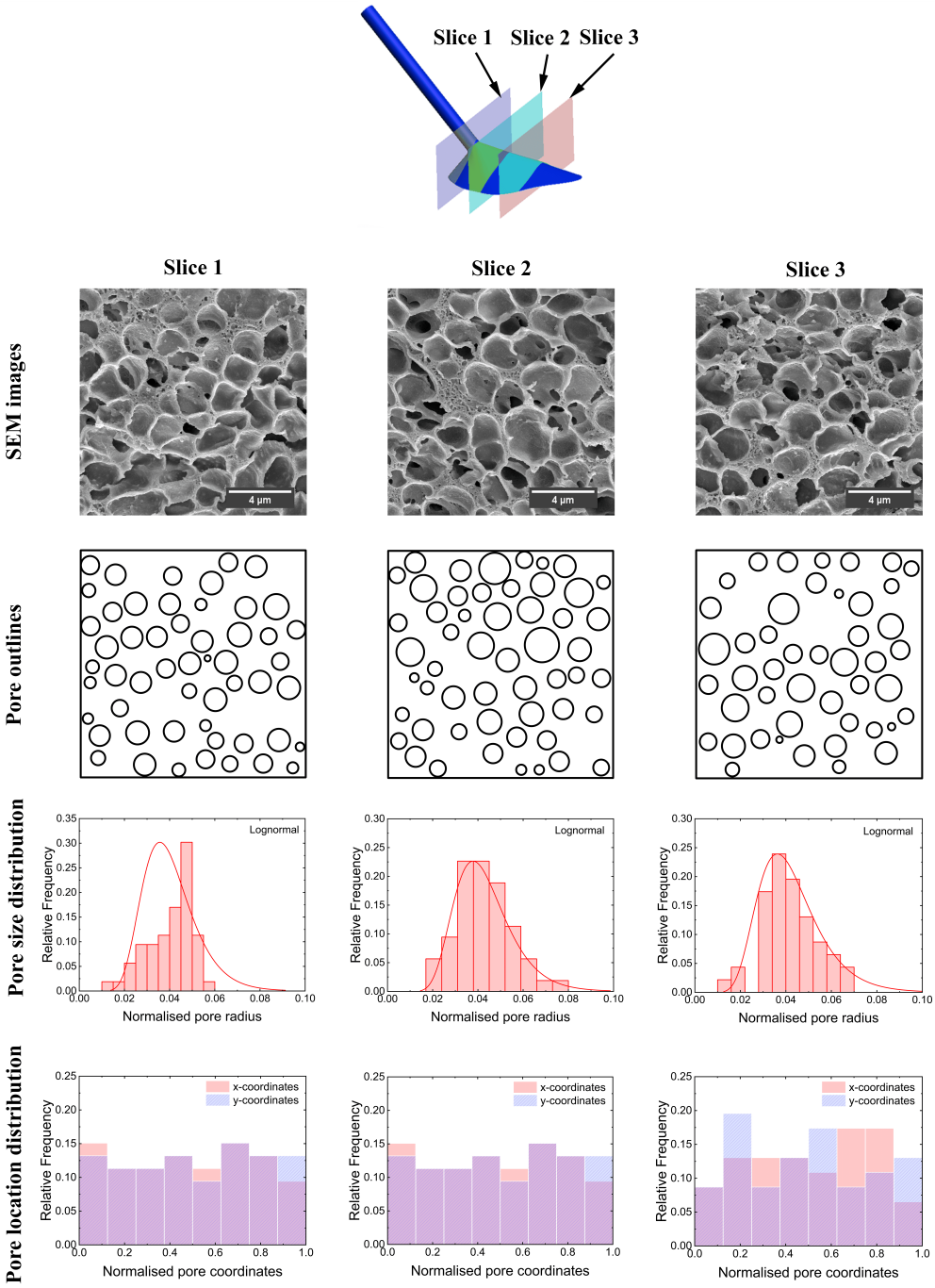


Figure D.1: Large-scale pore size and location distribution analysis for SEM images of the same mussel.

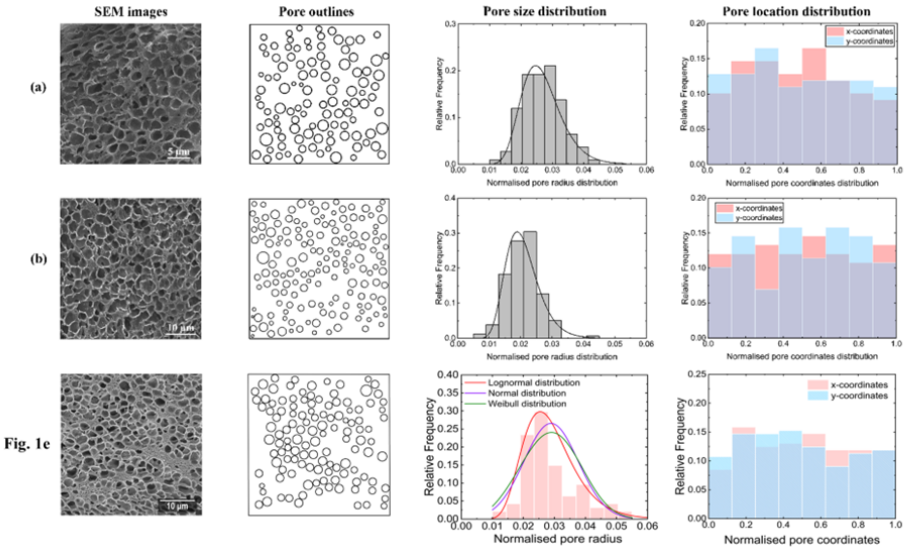


Figure D.2: Large-scale pore size and location distribution analysis for SEM images of different mussel plaques.

Table D.2: Porosity (υ_l), normalised mean radius ($\bar{\mu}_p^*$) and normalised standard deviation of radius ($\bar{s}_p^*$) of the simplified large-scale pores within the SEM images.

	Porosity (υ_l)	$\bar{\mu}_p^*$	$\bar{s}_p^*$
Figure 1e	27%	0.031	0.009
Figure D.2a	26%	0.027	0.006
Figure D.2b	23%	0.021	0.005

D.2 The simplified process of the pore distribution of the mussel plaque cores

The porous structure of the mussel plaque is inherently complex, with irregular pores varying significantly in shape and size, posing challenges for accurate quantification of porosity and other distribution parameters. To address this, we have idealised these irregular pores into circular shapes, enabling a more straightforward approach to measuring key parameters such as porosity, pore radius, and the coordinates of pore centres (Figure D.3). This idealisation ensures uniformity in analysis and facilitates the application of mathematical models and computational methods. During this

process, pores that appeared incomplete or had poorly defined boundaries were excluded to maintain the accuracy and reliability of the measurements. Special attention was given to avoiding the overlap of pores during the idealisation process, as overlapping can lead to incorrect calculations of porosity and pore distribution. Despite the simplification of circular pores, the main geometrical features of the mussel plaque are retained, ensuring the pore arrangement remains consistent with the original complex structure.

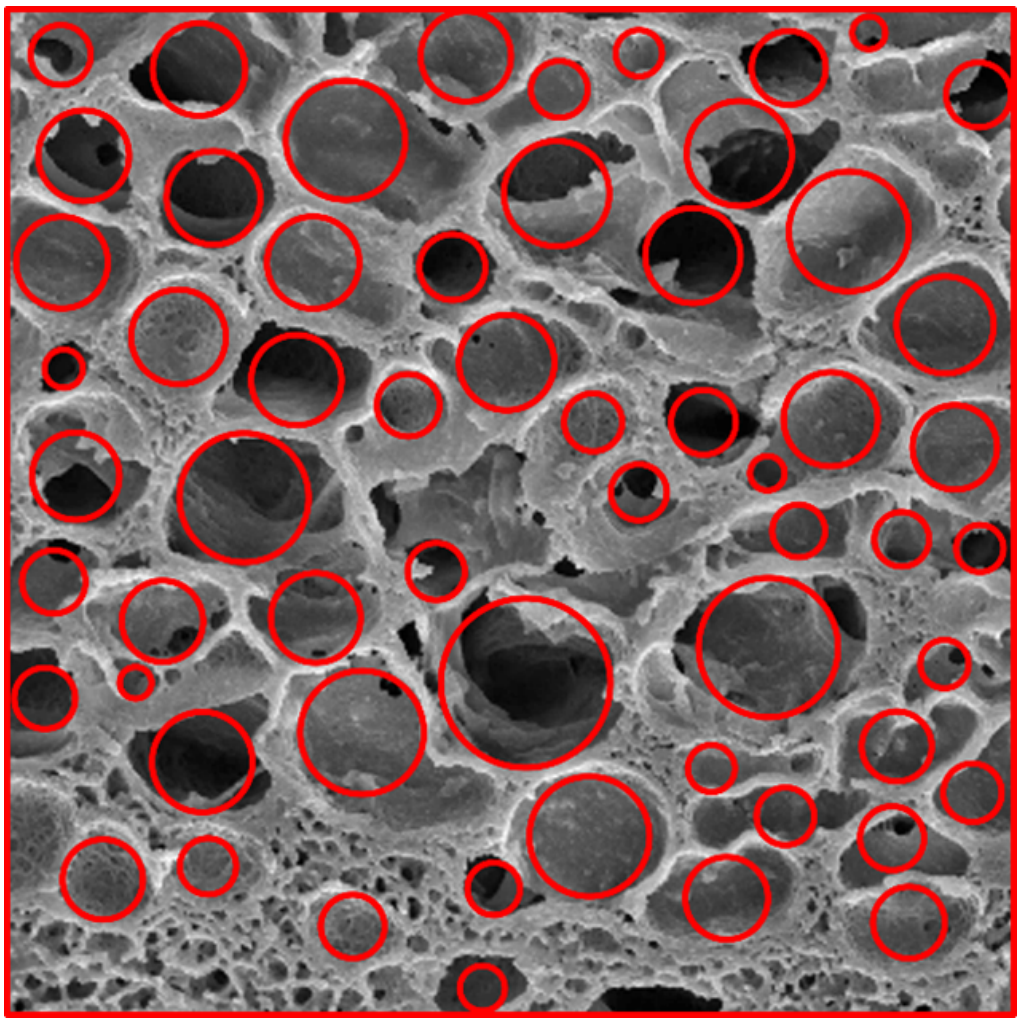


Figure D.3: The schematic drawing of the idealisation of the porous structure of mussel plaque cores.

D.3 The Q–Q (quantile–quantile) plots

The Q–Q (quantile-quantile) plot, which serves as a probability plot, was drawn in Figure D.4 to compare the probability distributions of x and y coordinates of the centres of large-scale pores in those 9 SEM images to a uniform distribution [203]. It can be seen that both x and y coordinates are consistent with a uniform distribution. Therefore, a uniform distribution of large-scale pore locations was applied to generate the porous RVEs.

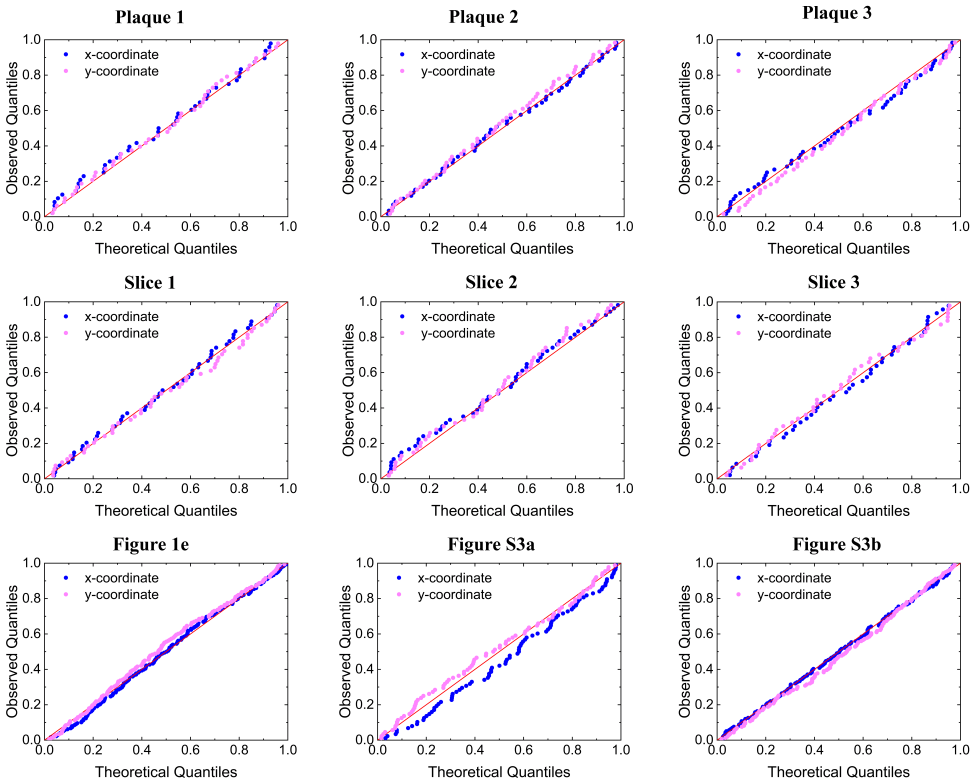


Figure D.4: Q–Q plots (quantile-quantile plot) comparing the x and y coordinates of large pores within the 9 mussel plaque SEM photos to a uniform distribution.

D.4 The size effect of RVE

Because the random distribution of pores affects the stress-strain curve of the RVE, using randomly distributed pore samples to detect dimensional

effects is not applicable. Instead, pores with a radius of 1.12 mm (mean value of pore size distribution) were uniformly arranged in RVEs of three different sizes (15x15 mm, 30x30 mm, 60x60 mm). The porosity of the RVEs of all sizes was 27%, which is the same as the large-scale pore porosity applied in Chapter 5. To ensure that the pore spacing was equal for each of the three different RVE sizes, a spacing of 3.66 mm was applied (Figure D.5).

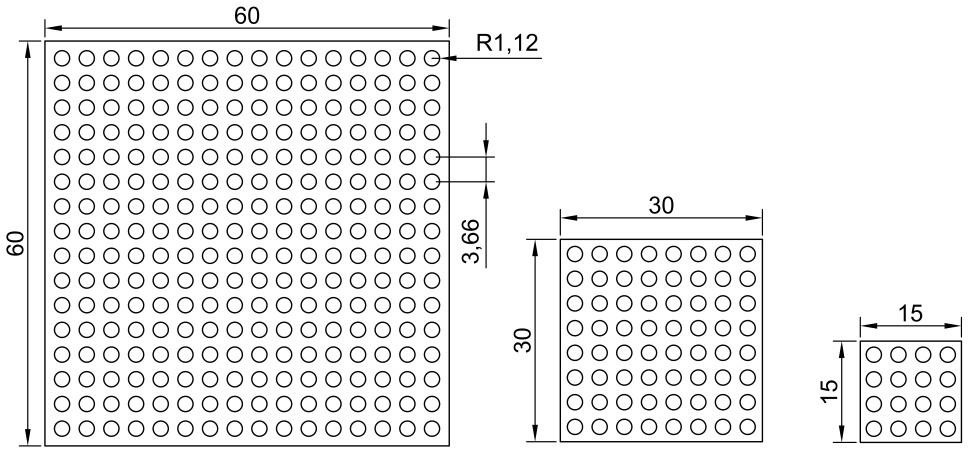


Figure D.5: Schematic diagram of three difference sizes RVEs (60x60 mm, 30x30 mm, 15x15 mm).

It can be seen from Figure D.6 that the stress-strain curves of the three different sizes of RVEs almost overlapped, thus learning that the size effect can be neglected in this study.

D.5 The small-scale pores size effect study for the multi-scale porous RVEs

Sample C in Section 5.5.2 was selected to regenerate the multi-scale porous RVEs with three different approximate small-scale pore sizes (0.4 mm, 0.5 mm and 0.6 mm) to understand the size effect on the macroscopic material

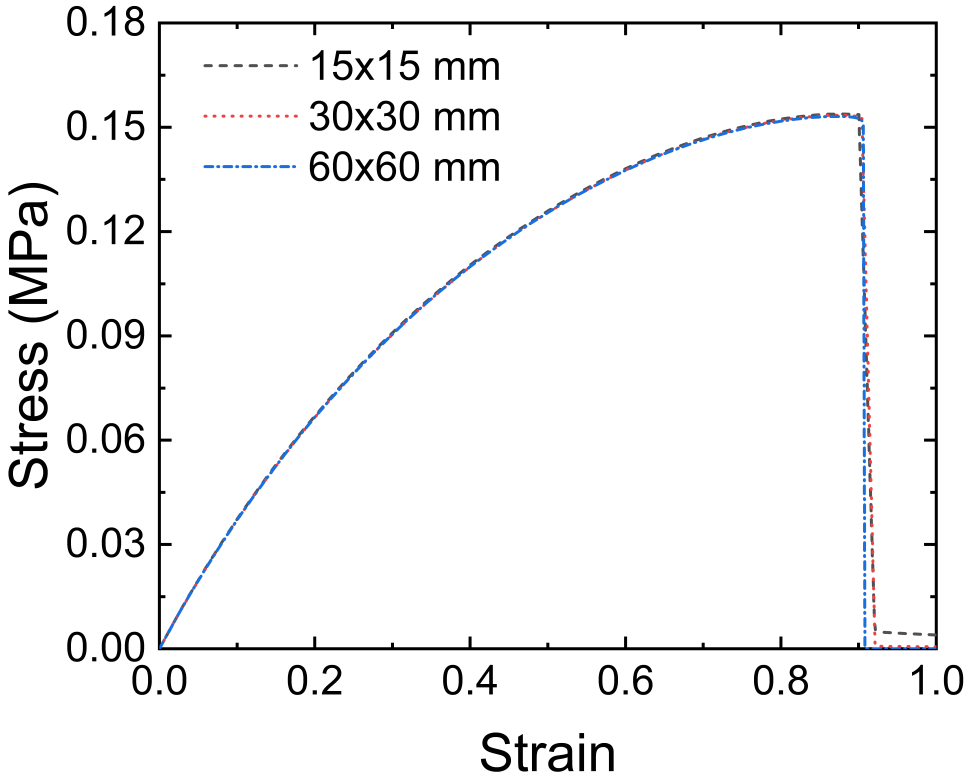


Figure D.6: Strain-stress curves of the three difference sizes RVEs (60x60 mm, 30x30 mm, 15x15 mm).

behaviours of multi-scale RVEs. In ABAQUS, Sample C was meshed using triangular elements with three different approximate mesh sizes: 0.4 mm, 0.5 mm and 0.6 mm. The 2D elements in the FE models were then removed, and the remaining nodes were connected using truss elements (T2D2T) as described in Section 3.2 of the original text. This generated three multi-scale porous RVEs with approximate small-scale pore size approximations of 0.4 mm, 0.5 mm and 0.6 mm, respectively. It is noteworthy that the porosities of these three multiscale porous RVEs remain consistent by adjusting the radius of truss elements. The results show that the size of the small-scale pores within the multi-scale porous RVEs has an insignificant effect on the macroscopic material behaviours of multi-scale porous RVEs thereby 0.5 mm was set as the approximate small-scale pore size in the simulations (Figure D.7).

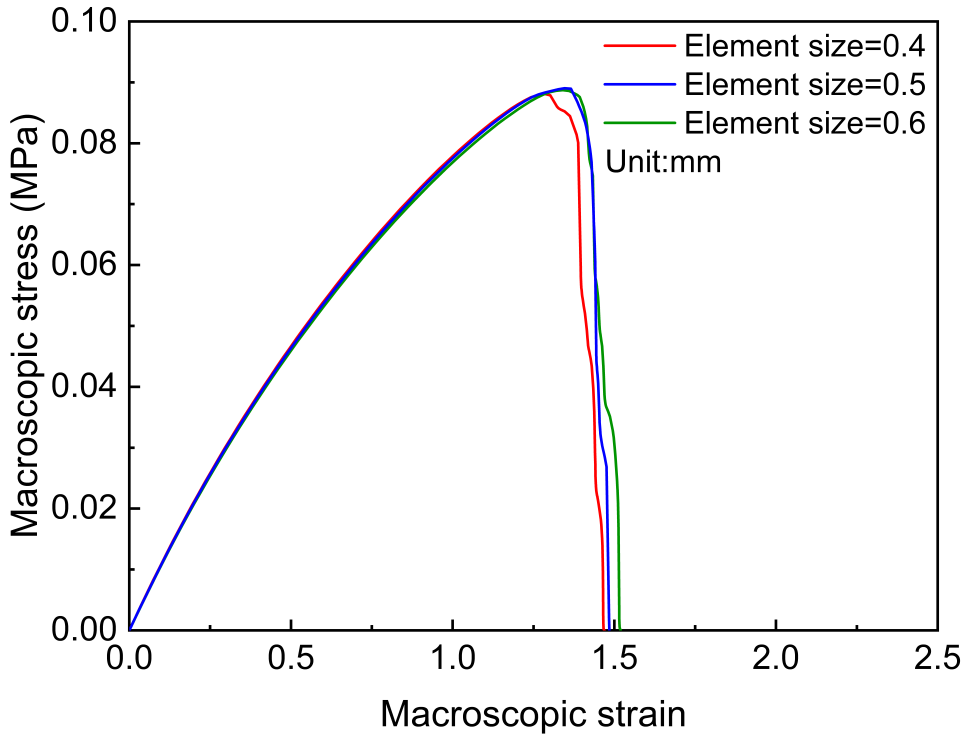


Figure D.7: The macroscopic stress-strain curves of multi-scale porous RVEs with different approximate small-scale pore sizes: 0.4 mm, 0.5 mm (Sample C') and 0.6 mm.

D.6 The derivation of Eq. 5.14

The following equation can be derived from Eqs. 5.12 and 5.13 in Chapter 5:

$$\dot{U} = \int_{\Omega} \left(\frac{\partial g(c)}{\partial c} \psi \dot{c} + g(c) \frac{\partial \psi}{\partial \boldsymbol{F}} : \dot{\boldsymbol{F}} \right) dV \tag{D.1}$$

where $\dot{\mathbf{F}}$ is the rate of change of the deformation gradient, which can be presented as $\dot{\mathbf{F}} = \frac{d}{dt}(\nabla \mathbf{u}) = \nabla \frac{d\mathbf{u}}{dt} = \nabla \dot{\mathbf{u}}$. The velocity field $\dot{\mathbf{u}}$ represents the rate of change of the displacement field $\mathbf{u}$ with respect to time.

Meanwhile, the vector calculus identity for the divergence of a product of a vector field a and $\boldsymbol{a}$ vector field $\boldsymbol{A}$ is shown below:

$$\mathrm{div}(\boldsymbol{a} \cdot \boldsymbol{A}) = \boldsymbol{a} \cdot \mathrm{div}(\boldsymbol{A}) + \boldsymbol{A} : \nabla \boldsymbol{a} \tag{D.2}$$

Therefore, the second term on the right-hand side of Eq. D.1 can be written as:

$$\begin{aligned}\int_\Omega g(c)\frac{\partial\psi}{\partial \boldsymbol{F}} : \dot{\boldsymbol{F}} dV &= \int_\Omega g(c)\frac{\partial\psi}{\partial \boldsymbol{F}} : \nabla\dot{\mathbf{u}} dV \\ &= \int_\Omega \mathrm{div}\left(g(c)\frac{\partial\psi}{\partial \boldsymbol{F}}\cdot\dot{\mathbf{u}}\right) dV - \int_\Omega \mathrm{div}\left(g(c)\frac{\partial\psi}{\partial \boldsymbol{F}}\right)\cdot\dot{\mathbf{u}} dV\end{aligned} \tag{D.3}$$

It is also known that the equation of the divergence theorem is,

$$\int_\Omega \nabla\cdot\mathbf{F} dV = \int_{\partial\Omega} \mathbf{F}\cdot\mathbf{n} dA \tag{D.4}$$

Hence Eq. D.3 can be rewritten as:

$$\int_\Omega g(c)\frac{\partial\psi}{\partial \boldsymbol{F}} : \dot{\boldsymbol{F}} dV = \int_{\partial\Omega} g(c)\frac{\partial\psi}{\partial \boldsymbol{F}}\cdot\dot{\mathbf{u}}\cdot\mathbf{n} dA - \int_\Omega \left(\nabla\cdot\left(g(c)\frac{\partial\psi}{\partial \boldsymbol{F}}\right)\right)\cdot\dot{\mathbf{u}} dV \tag{D.5}$$

Consequently, Eq. D.1 can be expressed as:

$$\dot{U} = \int_\Omega \left(\frac{\partial g(c)}{\partial c}\psi\dot{c}\right) dV + \int_{\partial\Omega} g(c)\frac{\partial\psi}{\partial \boldsymbol{F}}\cdot\dot{\mathbf{u}}\cdot\mathbf{n} dA - \int_\Omega \left(\nabla\cdot\left(g(c)\frac{\partial\psi}{\partial \boldsymbol{F}}\right)\right)\cdot\dot{\mathbf{u}} dV \tag{D.6}$$

D.7 The derivation of Eq. 5.18

Based on Eq. 5.17 in the original text, the rate of the dissipated energy from crack formation $\dot{D}^f$ can be expressed as:

$$\dot{D}^f = \int_\Omega G_c\left(\frac{c\dot{c}}{l} + l(\nabla c\cdot\nabla\dot{c})\right) dV \tag{D.7}$$

The vector calculus identity for the divergence of a product of a scalar field

ϕ and a vector field $\mathbf{A}$ is shown below:

$$\nabla \cdot (\phi \mathbf{A}) = \nabla \phi \cdot \mathbf{A} + \phi (\nabla \cdot \mathbf{A}) \tag{D.8}$$

Therefore, the second term on the right-hand side of Eq. D.7 can be rewritten as:

$$\int_{\Omega} \left(G_c l \nabla c \cdot \nabla \dot{c} \right) dV = \int_{\Omega} \nabla \cdot (G_c l \nabla c \dot{c}) \, dV - \int_{\Omega} G_c l \dot{c} (\nabla \cdot \nabla c) dV \tag{D.9}$$

Meanwhile, the equation of the divergence theorem is shown below,

$$\int_{\Omega} \nabla \cdot \mathbf{F} dV = \int_{\partial \Omega} \mathbf{F} \cdot \mathbf{n} dA \tag{D.10}$$

Thus Eq. D.9 can be rewritten as follow:

$$\int_{\Omega} \left(G_c l \nabla c \cdot \nabla \dot{c} \right) dV = \int_{\partial \Omega} G_c l \nabla c \dot{c} \cdot \mathbf{n} dA - \int_{\Omega} G_c l \dot{c} (\nabla \cdot \nabla c) dV \tag{D.11}$$

Finally, based on Eqs. D.7 and D.11, we can obtain the following equation:

$$\dot{D}^f = \int_{\Omega} G_c \dot{c} \left(\frac{c}{l} - l \nabla^2 c \right) dV + \int_{\partial \Omega} G_c l \nabla c \dot{c} \cdot \mathbf{n} dA \tag{D.12}$$

D.8 The comparison of the solid and small-scale porous RVEs

Following Section 5.5.3, a truss RVE with 5% porosity, reflecting the porosity of small-scale pores observed in the plaque SEM image (Figure 5.1e), was firstly generated to compare with the solid RVE and study the effect

of the small-scale porous structure on material stiffness. It can be seen from Figure D.3 that the solid RVE exhibited significantly higher stiffness compared to the small-scale porous RVE. This indicates that even with a relatively small amount of porosity, the microstructure can substantially impact the mechanical properties, reducing the stiffness and making the material more compliant under tensile loading.

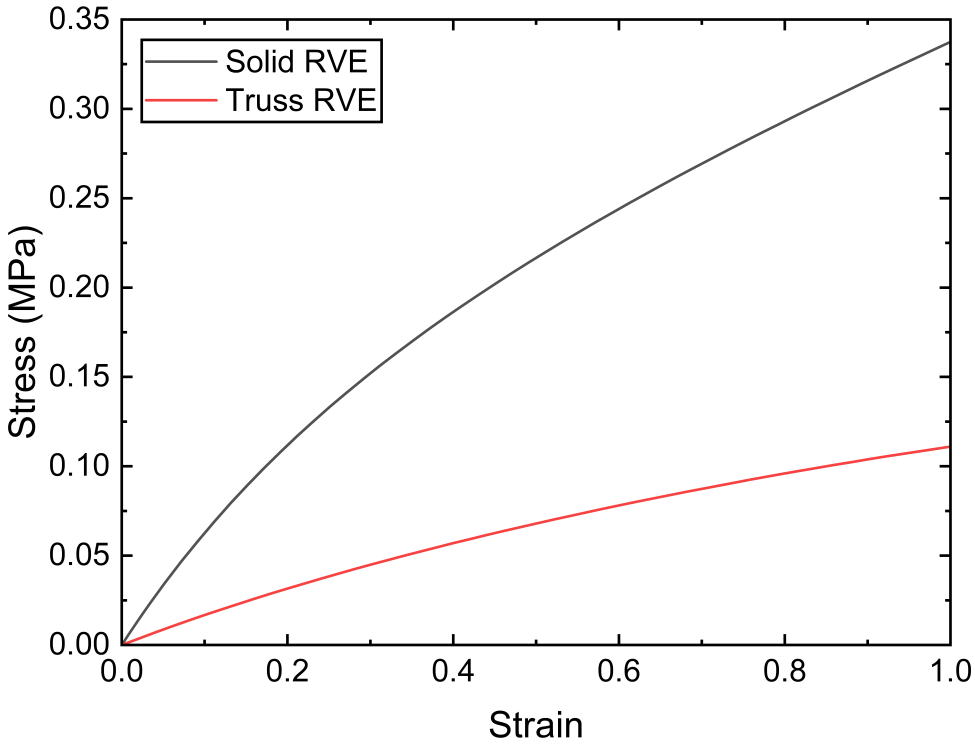


Figure D.8: The stress-strain curves of the solid and small-scale porous RVEs with 5% porosity.

Appendix E

E.1 Typical framed-supported force–indentation curves for carbon fibre mesh reinforced LLDPE foams

The following figures are the typical framed-supported force–indentation curves for five different carbon fibre mesh reinforced LLDPE foams under four different indenters in Chapter 6. The curves show the high consistency of the QSI tests.

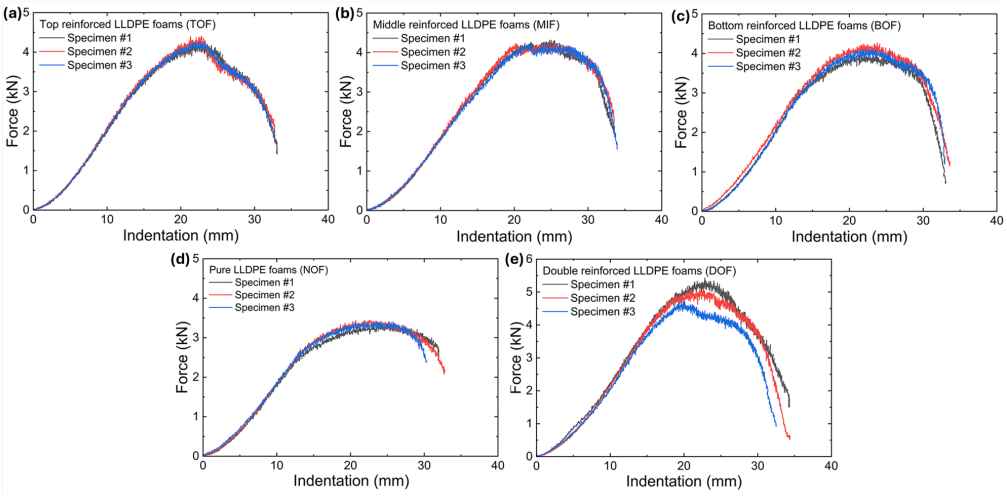


Figure E.1: Typical framed-supported force–indentation curves for different carbon fibre mesh reinforced LLDPE foams under conical indenter: (a) Top reinforced LLDPE foams (TOF), (b) middle reinforced LLDPE foams (MIF), (c) bottom reinforced LLDPE foams (BOF), (d) pure reinforced LLDPE foams (NOF) and (e) double reinforced LLDPE foams (DOF).

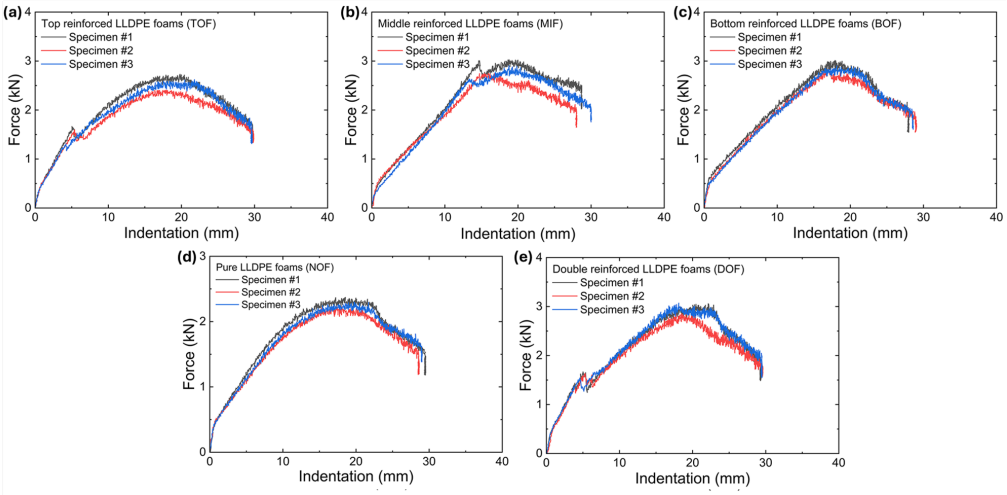


Figure E.2: Typical framed-supported force–indentation curves for different carbon fibre mesh reinforced LLDPE foams under truncated indenter: (a) Top reinforced LLDPE foams (TOF), (b) middle reinforced LLDPE foams (MIF), (c) bottom reinforced LLDPE foams (BOF), (d) pure reinforced LLDPE foams (NOF) and (e) double reinforced LLDPE foams (DOF).

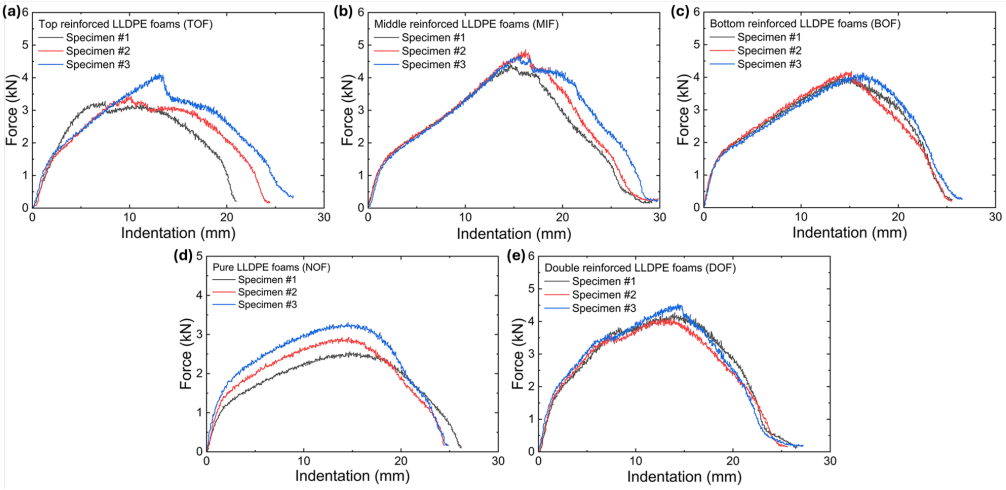


Figure E.3: Typical framed-supported force–indentation curves for different carbon fibre mesh reinforced LLDPE foams under flat-circular indenter: (a) Top reinforced LLDPE foams (TOF), (b) middle reinforced LLDPE foams (MIF), (c) bottom reinforced LLDPE foams (BOF), (d) pure reinforced LLDPE foams (NOF) and (e) double reinforced LLDPE foams (DOF).

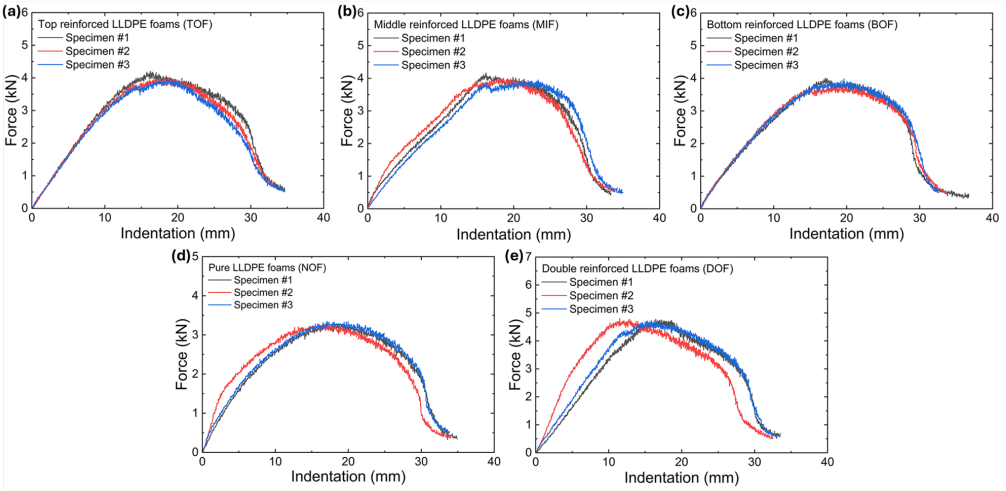


Figure E.4: Typical framed-supported force–indentation curves for different carbon fibre mesh reinforced LLDPE foams under hemi-spherical indenter: (a) Top reinforced LLDPE foams (TOF), (b) middle reinforced LLDPE foams (MIF), (c) bottom reinforced LLDPE foams (BOF), (d) pure reinforced LLDPE foams (NOF) and (e) double reinforced LLDPE foams (DOF).